University of Liège, Faculty of Sciences
CESAM Research Unit, Q-MAT Center
Experimental Physics of Nanostructured Materials

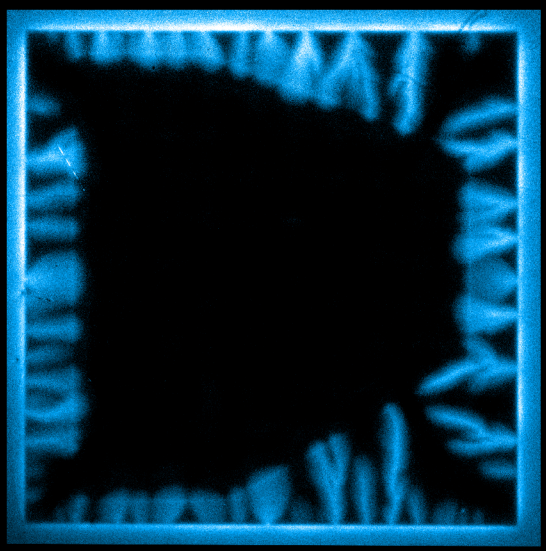

Magneto-optical investigation of superconducting hybrid structures

Jérémy Brisbois

Academic year 2016-2017

University of Liège, Faculty of Sciences
CESAM Research Unit, Q-MAT Center
Experimental Physics of Nanostructured Materials

Magneto-optical investigation of superconducting hybrid structures

Jury:

Prof. Dr. Ir. N. D. Nguyen (Chairman)
Prof. Dr. Ir. P. Vanderbemden
Prof. Dr. Ir. B. Vanderheyden
Prof. Dr. W. A. Ortiz (Universidade Federal de São Carlos, Brazil)
Prof. Dr. T. Tamegai (University of Tokyo, Japan)
Prof. Dr. A. V. Silhanek (Supervisor)

September 2017

Dissertation presented in partial fulfillment of the requirements for the degree of Doctor in Science

by

Jérémy Brisbois

Academic year 2016-2017

Abstract

Superconducting materials have found their way in numerous applications taking advantage of their perfect conductivity, such as lossless power cables and powerful magnets. However, the proper functioning of those devices is threatened by the displacement of vortices, microscopic magnetic flux bundles moving under the action of an electric current and dissipating energy. A common approach to deal with this problem consists in introducing defects in the superconductor to enhance vortex pinning, but this technique has the major drawback of being irreversible, as it permanently modifies the properties of the superconducting material. A way to overcome these limitations consists of adjoining a capping layer to the superconductor, in such a way that it interacts with the vortices through their stray field and enhances the damping of vortex motion. In particular, superconducting hybrids structures, combining a superconducting film with non-superconducting materials, constitute promising systems, as they provide an efficient and flexible way to explore the mechanisms of vortex damping without affecting the superconductor.

This thesis is devoted to the experimental investigation of several types of superconducting hybrids structures, consisting of a superconducting film partially covered either with a conductive layer or a magnetic layer. The samples are investigated by magneto-optical imaging, a microscopy technique relying on the Faraday effect to visualize the magnetic field distribution with a fair compromise between spatial resolution and field sensitivity. Comprehensive protocols have been developed for converting Faraday rotation data acquired by magneto-optical imaging into magnetic field maps and to enhance the quality of the images. For the sake of testing these procedures, we apply them on images of a microscopic planar coil and arrays of rectangular magnetic bars, for which the magnetic field can be determined by other means. Afterwards the technique is used in samples made of a superconductor and a magnetic material such as a microscopic disk or a polygonal layer. In these systems, it enables to reveal the comparatively weaker magnetic response of the superconductor from the background of larger fields and field gradients generated by the magnetic material.

When encountering a conductive layer deposited on top of the superconductor,

abrupt flux avalanches of magnetic flux bursting into a superconducting sample are deflected from their trajectories. Remarkably, in some cases the flux is totally excluded from the area covered by the conductive layer. We experiment this behavior in Nb films partially covered by Cu layers of various shapes and we present a simple classical model explaining the observed features, that considers a magnetic monopole approaching a semi-infinite conductive plane. This model suggests that electromagnetic braking, coming from eddy currents induced in the conductor, is a key mechanism in the avalanche deflection. Moreover, the metallic layer provides an additional velocity-dependent damping mechanism for the flux motion, that helps protecting the superconducting state from thermomagnetic instabilities. If flux moves with a velocity slower than $w = 2/\mu_0\sigma t$, where σ is the capping layer electric conductivity and t is its thickness, the flux penetration remains unaffected, whereas for incoming flux advancing faster than w, the metallic layer becomes an active screening shield. We explore these regimes by changing the thickness and the composition of the metallic layer. In particular, our results show that the general wisdom considering magneto-optical imaging as a non invasive technique might not be valid when the magneto-optical indicator lies at submicrometric distances from the sample surface. When the metallic layer is replaced by a perfect conductor, it is expected that the flux braking effect will occur for all flux velocities. We demonstrate this effect by investigating Nb samples with a thickness step. Some of the observed features, namely the deflection and the branching of the flux trajectories at the border of the thick center, as well as the favored flux penetration at the indentation, are reproduced by time-dependent Ginzburg-Landau simulations.

Finally, we experimentally show that local polarization of a magnetic layer can be applied for imprinting into a soft magnetic layer of permalloy (Py) the trajectory of vortices, traveling in a Nb superconducting film. In full analogy with the magnetic drawing board toy, vortices act as tiny magnetic scribers leaving a wake of polarized magnetic media in the Py board. The mutual interaction between superconducting vortices and ferromagnetic domains is strongly dependent on the thickness of the magnetic layer. In all cases, we observe that the flux is delayed at the border of the magnetic layer. For thick Py layers, the stripe magnetic domain pattern guides both the smooth magnetic flux penetration and the abrupt vortex avalanches in the Nb film. It is however in thin Py layers without stripe domains that superconducting vortices leave the clearest imprints of locally polarized magnetic moment along their paths. Furthermore, we demonstrate that the imprinting of a microstructured magnet at room temperature can be exploited to define at will the pinning landscape in the superconductor.

Résumé

Les matériaux supraconducteurs sont utilisés dans de nombreuses applications profitant de leur conductivité parfaite, notamment des câbles conduisant le courant électrique sans perte d'énergie ou encore des électroaimants performants. Cependant, le fonctionnement de ces dispositifs est menacé par le déplacement des vortex (ou fluxons), ces unités microscopiques de flux magnétique se déplaçant sous l'action d'un courant électrique et dissipant de l'énergie. Une approche fréquemment adoptée pour traiter ce problème consiste à introduire des défauts dans le supraconducteur afin de renforcer l'ancrage des vortex. Cependant, cette technique présente l'inconvénient majeur de modifier irrémédiablement les propriétés du matériau. Une manière de contourner ces limitations consiste à couvrir le supraconducteur d'une couche d'un autre matériau. De cette manière, l'amortissement du mouvement des vortex est réalisé par l'interaction de cette couche avec les vortex via leur champ magnétique. Les structures hybrides supraconductrices, combinant un film supraconducteur avec des matériaux non-supraconducteurs, constituent des systèmes prometteurs car ils permettent d'explorer de façon efficace et flexible les mécanismes d'amortissement des vortex sans affecter le supraconducteur.

Cette thèse est dédiée à l'étude expérimentale de plusieurs types de structures hybrides supraconductrices, formées d'un film supraconducteur partiellement recouvert d'une couche conductrice ou magnétique. Les échantillons sont étudiés au moyen de l'imagerie magnéto-optique, une technique de microscopie se basant sur l'effet Faraday pour visualiser le champ magnétique, avec un bon compromis entre résolution spatiale et sensibilité au champ. Des protocoles ont été développés pour améliorer la qualité des images et pour déterminer l'intensité du champ magnétique à partir des données acquises par imagerie magnéto-optique. Ces procédures sont testées sur des images d'une bobine micrométrique et d'un réseau de barreaux magnétiques. Ensuite, la technique est appliquée à des échantillons obtenus en associant un supraconducteur et un matériau magnétique, tels qu'un disque microscopique ou une couche polygonale. Elle permet alors de révéler la réponse magnétique du supraconducteur, particulièrement lorsque cette dernière est faible comparée à celle du matériau magnétique.

Lorsqu'elles rencontrent une couche conductrice placée au-dessus d'un supraconducteur, les avalanches de flux pénétrant brusquement dans l'échantillon sont déviées de leur trajectoire. Dans certains cas, le flux est même totalement exclu de la région recouverte par la couche conductrice. Nous avons mis en évidence ce comportement dans des films de Nb partiellement recouverts de couches de Cu de diverses épaisseurs. Nous présentons un modèle classique simple qui explique l'origine du phénomène en considérant un monopole magnétique approchant un plan conducteur semi-infini. Ce modèle suggère que le freinage électromagnétique, issu des courants de Foucault induits dans le conducteur, est le mécanisme à la base de la déflexion des avalanches. En outre, la couche métallique est à l'origine d'une contribution supplémentaire à l'amortissement des déplacements des vortex. Cette dernière dépend de la vitesse et aide à protéger l'état supraconducteur du développement d'instabilités thermomagnétiques. Lorsque le flux se déplace à une vitesse v inférieure à $w = 2/\mu_0\sigma t$, où σ est la conductivité électrique de la couche recouvrant le supraconducteur et t est son épaisseur, la pénétration du flux n'est pas affectée. En revanche, si $v > w$, la couche métallique devient un bouclier d'écrantage actif. Nous explorons ces différents régimes en changeant l'épaisseur de la couche métallique et sa composition. Nos résultats montrent notamment que le fait généralement accepté que la magnéto-optique est une technique non-invasive doit en général être reconsidéré lorsque l'indicateur magnéto-optique se trouve à des distances submicrométriques de la surface de l'échantillon. Lorsque la couche métallique est remplacée par un conducteur parfait, l'effet de freinage devrait être présent indépendamment de la vitesse du flux. Nous démontrons cet effet en étudiant des échantillons de Nb avec un échelon d'épaisseur. Certains des phénomènes observés, notamment la déflexion et la subdivision des trajectoires du flux à l'emplacement de l'échelon, sont reproduits par des simulations basées sur les équations de Ginzburg-Landau dépendantes du temps.

Enfin, nous démontrons expérimentalement qu'il est possible d'exploiter la polarisabilité d'un matériau magnétique pour y imprimer la trajectoire des vortex. Nous illustrons ce phénomène en enregistrant dans une couche magnétique de permalloy (Py) la trace des vortex se déplaçant dans un film supraconducteur de Nb. En analogie complète avec l'ardoise magique, les vortex se comportent comme des poinçons microscopiques, laissant dans leur sillage une trace de milieu magnétique polarisé dans l'ardoise de Py. L'interaction entre les vortex supraconducteurs et les domaines ferromagnétiques dépend fortement de l'épaisseur de la couche magnétique. Dans tous les cas, nous observons que le flux est retardé au bord de la couche. Pour des couches épaisses de Py, les bandes de domaines magnétiques guident aussi bien la pénétration douce du flux que les avalanches de vortex dans le film de Nb. Cependant, les vortex supraconducteurs laissent sur leur chemin les traces les plus nettes dans les couches minces de Py, où les domaines magnétiques perpendiculaires au plan sont

absents. Par ailleurs, nous démontrons que l'impression d'un aimant microstructuré dans le Py, réalisée à température ambiante, peut être exploitée pour définir à volonté le potentiel d'ancrage dans le supraconducteur.

Acknowledgements

This work is obviously not the work of a single person and it would not have been possible without the help of numerous people that I would like to acknowledge here.

First, I am grateful to the FRS-FNRS for funding my thesis with a Research Fellow grant.

I would like to acknowledge the members of my thesis comitee, Benoît Vanderheyden, Ngoc Duy Nguyen and Anne-Sophie Duwez, for following my progress during these four years.

My deepest thanks go to the jury members for taking the time to review my thesis and attend the defense.

The time-consuming process of sample fabrication was carried by several people I would like to acknowledge here. The Nb films with various coatings (Cu, Au, Py) were fabricated by Roman Kramer (Université Grenoble Alpes). Obaïd Adami evaporated the Cu layer (triangle and ring) in the facilities of Benoît Hackens (Université Catholique de Louvain-la-Neuve). Joachim Friztsche (Chalmers Institute of Technology) produced the Nb films with a step in thickness. The arrays of Co magnetic bars where made by Jeroen Scheerder (KULeuven). Gorky Shaw, Nora Dempsey and Thibaut Devillers fabricated the NdFeB thermomagnetically patterned films (Université Grenoble Alpes). The micrometric coil was designed and fabricated by Sylvain Blanco Alvarez and Emile Fourneau.

I am particularly grateful to Tom Henning Johansen (University of Oslo) and Philippe Vanderbemden for providing the crucial indicators for the magneto-optical imaging experiments.

Several imaging techniques were used to complement the magneto-optical imaging data. I would like to thank Niels Verellen and Joris Van de Vondel (KULeuven), respectively for the optical characterization of the indicators and for giving me access to the MFM setup, and Mattias Timmermans and Ritika Panghotra for their assistance during the measurements. I am also grateful to Savita Veerapandian, who carried MFM measurements in the group of Pierre Colson. The SHPM measurements were performed by Gorky Shaw in the facilities of Roman Kramer and Klaus Hasselbach

(Université Grenoble Alpes). The SQUID magnetometry data were acquired at the Federal University of São Carlos, mostly by Maycon Motta.

I am grateful to Benoît Vanderheyden for his theoretical support on the complex problematics of vortex damping in the vicinity of a conducting layer and flux diffusion through border defects in superconductors. I would also like to acknowledge Obaïd Adami and Jonathan Avila for the COMSOL simulations featured in this work.

I am also very grateful to the GSM group (Federal University of São Carlos) for the decisive contribution to my training and to the magneto-optical imaging experiments. Especially, I would like to thank Wilson A. Ortiz for warmly welcoming me twice in his group, Fabiano Colauto for teaching me the rudiments of magneto-optical imaging and Maycon Motta for the countless hours he spent helping me to solve experimental issues, as well as for the measurements he performed for me. I am also grateful to Danusa do Carmo, Lincoln Pinheiro and Marlon Valerio Cuadron for their help during the measurements, as well as to all the students for their kindness.

I have spent four amazing years working at the university thanks to my colleagues, Xavier Baumans, Obaïd Adami, Željko Jelić, Jonathan Avila, Gorky Shaw, Joseph Lombardo, Sylvain Blanco Alvarez, Emile Fourneau, Lincoln Pinheiro, Mahmoud Abdel-Hafiez and Jonas Müller. I am really grateful to them for their decisive help on scientific matters, namely during the experiments, for the data analysis, the improvement of the setup, the proofreading of my thesis, and much more. Moreover, they were always keen to set up a fun and motivating working atmosphere.

It will be difficult to acknowledge sufficiently my advisor, Alejandro Silhanek, for giving me the opportunity to start (and end) my PhD thesis in his group and for his careful guidance. He gave me a lot of confidence and trust and the high level of performance he expected from me was a great incentive to improve along the way. I am very grateful for his countless ideas and suggestions during our scientific discussions, as well as for his flexibility and his open-mindedness, particularly in hard times.

An important contribution to this work, although not scientific, was provided by my relatives and friends, especially Clémentine, Sylvain, Marie-Julie, Ludivine, Antoine, Judith and Alain. The great times we spent together regularly made my day. Special thanks go also to my Brazilian friends, namely Lincoln, Dayana, Joana, Jhony, Eraldo, Amabile, Cassio and Everton for making me feel at home during my stay in São Carlos. Of course, I am indebted to my family for the support they provided during my studies and my PhD thesis. In particular, I would like to thank my parents, Anaïs, Lara, my parents-in-law and Sophie, for doing all they could to help me.

Finally, I could never express enough how much the support of Elodie carried weight in the realization of this thesis. She has been comprehensive and supportive beyond belief and I will be forever grateful for her help.

Contents

Introduction

Since their discovery in 1911, superconducting materials have progressively gained a unique place in numerous applications: powerful magnets, levitating trains, high-sensitivity magnetometers, lossless transmission power cables, voltage standard, quantum bits, single photon detectors and bolometers, to name a few. All these examples take advantage of the fundamental properties of superconductors, perfect electric conductivity and perfect diamagnetism. Superconductivity can be depicted as a magnetophobic state of matter, characterized by persistent currents flowing around the material surface to shield the external field from its bulk. However, in technologically relevant superconductors, the magnetic field can penetrate the material in the form of topologically protected entities, called vortices. These quantized units of flux agglomerate magnetic flux lines around their normal core of a few tens of nanometers in diameter. Unfortunately, the displacements of these objects under the action of an electric current lead to dissipation in the normal vortex cores, threatening the perfect conductivity of the superconductor and limiting its potential for applications.

Therefore, during the last decades, a huge effort has been devoted to inhibit the motion of vortices, by introducing in the superconductor pinning centers, where the superconducting condensate is already weakened. There is a large zoology of pinning centers, ranging from natural material defects such as dislocations, grain boundaries, twin planes, impurities and vacancies, to artificial pinning sites introduced by ion/proton irradiation, ion implantation or nanofabrication. Unfortunately, all these pinning landscapes modify irreversibly the superconducting properties, since pinning centers cannot be removed or modified once introduced in the material.

While flux lines interact with inhomogeneities inside the superconductor, the static and dynamic response of vortices can also be modified if their stray field outside the superconductor is altered, for instance by another material placed in its vicinity. This is precisely why multilayered hybrid structures combining superconducting and non-superconducting materials have been an active field of research in recent years. Hybrid structures are flexible systems to explore alternative vortex damping mechanisms, since in these, vortex motion can be affected in a wide variety of situations without

modifying the properties of the superconducting material.

The objective of this work is to explore, from a fundamental point of view, other means to reduce dissipation in superconductors by increasing damping of the vortex motion. This is achieved through the investigation of superconducting hybrid structures, where essentially two types of damping mechanisms are tackled.

Firstly, it has been shown that the stray field of a moving vortex induces eddy currents in a nearby metallic layer, leading to a damping force, non-linear with respect to the vortex velocity. This electromagnetic effect has proved efficient in protecting superconducting magnets from quenching due to catastrophic flux jumps, where flux abruptly bursts into the material and destroys superconductivity. Moreover, if the metallic layer is structured, it can be used to induce an in-plane anisotropy in the damping coefficient.

Secondly, we address the problematic of magnetic damping, taking place in structures combining a superconductor with a magnetic material. Depending on the relative strength of the characteristic fields of the superconductor and the magnetic layer, the upper critical field H_{c2} and the coercive field H_{coe} respectively, several mechanisms may be involved in the damping process, such as generation of magnons and spin polarization. We show evidence of the latter in a superconducting film covered by a soft ferromagnet, where we use the vortex stray field as submicron-sized magnetic tweezers to locally polarize spin carriers. In addition, we explore the possibility to exploit a hard ferromagnetic layer to control the vortex trajectories and tune the pinning potential at will.

Most of the observations on superconducting hybrid structures are done through magneto-optical imaging. This microscopy technique relies on the Faraday effect, rotating the polarization of light proportionally to the magnetic field in an indicator placed on top of the sample. It has the advantage to provide real time images of the magnetic field distribution, while presenting a fair compromise between spatial resolution and field sensitivity. It is intrinsically adapted for the observation of sample areas up to a few millimeters squared, comparable to the size of the structures under study.

This thesis is structured as follows:

In **Chapter 1**, we review the theoretical concepts of superconductivity that are necessary for a good comprehension of the subsequent chapters. We start by covering the basics of superconductivity and vortices in type-II superconductors. We then describe the flux penetration in superconducting materials, with a particular attention to the thin film geometry, central to this work. After detailing the smooth flux penetration regime, we emphasize the regime of abrupt flux avalanches appearing at low

temperatures.

Chapter 2 describes the cryogenics and the magneto-optical imaging technique, on which this work relies for the magnetic field visualization. After an overview of the physical principles behind cooling and the cryostat configuration, the basics of the magneto-optical imaging technique and the setup are presented. We take particular care to characterize our system, the optics as well as the indicator, and explain the data acquisition and analysis procedures. We also expose techniques to improve the magneto-optical images and recover quantitative information on the magnetic field and we illustrate them on various samples.

In **Chapter 3**, we study the flux penetration in a superconducting thin film partially covered by a metallic layer. Depending on the velocity of the vortices and the properties of the conductor, significant electromagnetic damping takes place due to eddy currents in the metal. We highlight the crucial role played by the border of the conductor and we propose a classical model to account for the deflection of flux avalanches, efficiently shielded from the area covered by the metal.

In **Chapter 4**, we generalize the results of the previous chapter to the extreme situation where the capping layer is a superconductor, by considering superconducting films with a step in thickness. Our experimental findings that the vortex damping is velocity-independent are in agreement with the model presented earlier, although additional contributions, such as vortex core energy, need to be considered. These results are backed up by time-dependent Ginzburg-Landau simulations.

In **Chapter 5**, we focus on the magnetic damping in superconducting-ferromagnetic hybrid structures. The mutual interaction between a superconductor and a magnetic layer leads to interesting phenomena, such as strong anisotropy in the flux penetration and in return, polarization of the magnetic media along the trail of vortices. This opens the path for a new method to visualize the flux penetration *ex situ*, since the trajectories of the vortices can be imprinted in the magnetic layer and observed up to room temperature. We take advantage of the versatility of the magnetic material to tune at will the pinning landscape, strongly affecting the flux penetration.

Chapter 1

Magnetic flux in superconductors

Popular summary

The hybrid structures we study in this thesis are based on materials becoming superconducting when they are cooled down to low temperatures. Superconductivity is a state of matter characterized by two fundamental properties. Firstly, superconductors have zero resistance, meaning that they can carry an electric current without dissipating energy. Secondly, superconducting materials are magnetophobic: when they are immersed in a magnetic field, they react to expel the magnetic field. This is caused by the appearance of screening currents flowing around the sample, which generate a magnetic field countering the external magnetic field.

However, in type-II superconductors, the class of superconductors useful for practical applications, magnetic field is allowed inside the material in tiny cylindrical flux bundles called vortices. These entities have a diameter of about a hundred of nanometers and can be pictured as small tubes of material in the normal non-superconducting state, letting the magnetic field pass through a matrix of superconducting material. If a weak electric current is applied, vortices stay anchored to defects in the material, but if the current is strong enough, they start moving in a viscous media and thus to dissipate energy, eventually leading to the disappearance of the perfect conductivity property.

The equilibrium distribution of the magnetic field inside the superconductor can be reached in two different ways, depending on how fast the heat produced by the vortex motion is evacuated from the sample. In most cases, the heat is efficiently removed, so vortices enters from the sample borders and slowly progress towards the center as the external magnetic field is increased. However, in some situations, when the heat is not properly evacuated to the environment, the temperature of the superconductor locally rises along the trail of moving vortices. This reinforces vortex motion and leads to further energy dissipation, causing catastrophic events called magnetic flux avalanches, where a burst of millions of vortices penetrates into the sample in a very short time scale. These events are somewhat similar to snow avalanches, occurring when the accumulation of snow (of magnetic field here) on top of a mountain (at the border of the sample) cannot be sustained anymore, and snow slides to the bottom of the slope (field bursts into the superconductor).

1.1 Introduction

In this chapter, we develop the basic theoretical requirements on superconductivity necessary to understand the subsequent chapters of this thesis. We present the particularities of the superconducting state, i.e., the zero-resistance and the expulsion of the magnetic field. In type-II superconductors, of particular technological interest, the magnetic field enters in small quantized cylinders of flux called vortices, central to this work. We will review their basic properties, with a particular attention to their motion and the resulting dissipation. We then describe how flux enters a superconductor when the applied magnetic field is increased or decreased in a bulk superconductor, and move to the more practical situation of a thin film, a key constituent of superconducting hybrid structures, where the field and current profiles are significantly modified with respect to the bulk geometry. The flux penetration can occur in two different regimes, depending on how efficiently the heat produced by vortex motion is evacuated. When heat is efficiently removed, flux enters smoothly in the sample when the magnetic field is increased. However, at low temperatures, when the heat diffusion is reduced, flux might enter the sample in sudden random bursts, called flux avalanches. The thermomagnetic origin of the avalanches is described and contrasted with small dynamically driven avalanches in the smooth flux penetration regime. The phenomenology of avalanches is detailed, along with their phase diagram in superconducting films.

1.2 Superconductivity basics

We start by reviewing the fundamental properties of the superconducting state. We then focus on the vortices present in type-II superconductors, and in particular in the Nb films that we study in this work.

1.2.1 General properties of the superconducting state

Superconductivity is a quantum state of matter discovered in 1911 [1] and existing at low temperatures in some materials, namely in certain ceramics and metals. It is characterized by two fundamental properties, perfect conductivity and perfect diamagnetism, appearing when the material is cooled down below its critical temperature T_c. Perfect conductivity expresses the ability of the superconductor to carry electric currents without dissipating energy, meaning that their resistance $R = 0$. This property is a macroscopic manifestation of quantum mechanics and arises from the condensation of electron pairs, called Cooper pairs [2], in the ground-state energy. The paired superconducting electrons are grouped in a single macroscopic wave function, stable

with respect to energy excitations smaller than $\Delta \sim k_B T_c$, as described by the BCS theory [3]. Superconductors are also perfect diamagnetic materials. When a superconductor is immersed in a magnetic field H, supercurrents are induced and generate a magnetization M, keeping the bulk flux-free. The magnetic field $\mathbf{B} = \mu_0(\mathbf{H} + \mathbf{M})$ in the bulk is then zero. This is the so-called Meissner state [4], first explained by the London theory [5]. At the surface of the superconductor, the magnetic field decays exponentially over a distance λ called the magnetic penetration depth, usually on the order of hundred nanometers.

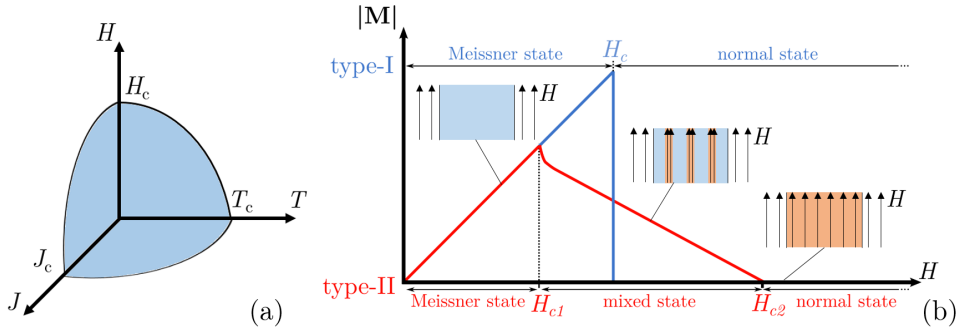

Figure 1.1: **Basic properties of the superconducting state.** (a) Phase diagram of the superconducting state, limited by the critical temperature T_c, the critical current density J_c and the critical magnetic field H_c. (b) Magnetization M of a superconductor as a function of the applied magnetic field H, illustrating the fundamental difference in behavior between type-I and type-II superconductors. While superconductivity disappears suddenly at the critical field H_c in type-I superconductors, it survives between the lower and upper critical fields, H_{c1} and H_{c2}, in type-II superconductors, where field is allowed inside the superconductor. The insets represent, from left to right, the Meissner state, the mixed state and the normal state. Superconducting regions are colored in blue, while normal regions are in orange.

The typical phase diagram of a superconductor is represented in Fig. 1.1 (a). Aside from the temperature T, increasing the energy fluctuations and ultimately destroying superconductivity at $T = T_c$, the superconducting state is also limited by a maximum current density J_c and a maximum magnetic field H_c. Depending on their behavior upon increasing the applied field H, superconductors are classified either as type-I or type-II. In type-I superconductors, the Meissner state survives up to the critical field H_c, at which superconductivity disappears at once, as illustrated in Fig. 1.1 (b) by the sudden drop of the magnetization M. On the contrary, in type-II superconductors, superconductivity is not lost once the Meissner state disappears: field enters the superconductor above H_{c1}, called the lower penetration field, and M is reduced gradually upon increasing H up to the upper critical field H_{c2} where superconductivity is suppressed. This intermediary state is called the mixed state. Most applications

rely on type-II superconductors, namely because they can operate under much higher fields, since H_{c2} is always significantly larger than H_c.

Materials are classified in type-I or type-II superconductors depending on the sign of the surface energy $\sigma_{ns} \sim \xi - \lambda$ associated with the interface between normal and superconducting regions [6]. The coherence length ξ is a characteristic distance for the decay of the superconducting electrons density n_s, occurring between the superconducting and normal regions. If $\sigma_{ns} > 0$, the creation of such interfaces is energetically unfavorable and the material is a type-I superconductor. If $\sigma_{ns} < 0$, the state of lower energy corresponds to the situation where some normal regions where flux has penetrated are allowed within the superconductor. In practice, the boundary between these two regimes is assessed by computing the Ginzburg-Landau parameter $\kappa = \lambda/\xi$: if $\kappa < 1/\sqrt{2}$, the material is a type-I superconductor, while it is a type-II if $\kappa > 1/\sqrt{2}$.

1.2.2 Vortices in type-II superconductors

In type-II superconductors, when the magnetic field is larger than H_{c1}, flux enters the superconductor in small cylinders with a normal core of diameter $\sim 2\xi$, called vortices (or fluxons) [6]. The magnetic flux associated with a vortex is quantized and is a multiple of the fundamental quantum of magnetic flux $\phi_0 = h/2e = 2.07\times10^{-15}$ Tm^{-2}. When H is increased over H_{c1}, the number of vortices inside the superconductor rises, until H_{c2} is reached. At this field, the normal cores of the vortices overlap and superconductivity disappears, as represented in the insets of Fig. 1.1 (b).

1.2.2.1 Description of a vortex

In this section, we consider a vortex whose flux line are along the z-direction inside a bulk superconductor. In the case where $\kappa \gg 1$, in the framework of the Ginzburg-Landau theory, the magnetic field $B_z(r)$ at a radial distance r of the vortex is given by [7]

$$B_z(r) = \frac{\phi_0}{2\pi\lambda^2} \mathrm{K}_0\left(\frac{r}{\lambda}\right), \tag{1.1}$$

where K_0 is the modified Bessel function of the second kind (order 0). The magnetic field distribution following this expression is represented in Fig. 1.2 (a). Since Eq. (1.1) diverges at small r, a cutoff is introduced for $r < \xi$ and the maximum field at the vortex core is approximately constant and given by

$$B_{z,\max}(r) \simeq \frac{\phi_0}{2\pi\lambda^2} \ln\kappa. \tag{1.2}$$

From Eq. (1.1), $B_z(r)$ decays exponentially far from the vortex core ($r \gg \lambda$):

$$B_z(r) \simeq \frac{\phi_0}{2\pi\lambda^2}\sqrt{\frac{\pi\lambda}{2r}}\,\mathrm{e}^{-\frac{r}{\lambda}}. \tag{1.3}$$

The superconducting electrons density, $n_\mathrm{s}(r)$, is represented in Fig. 1.2 (b) and drops to zero at the center of the vortex. The modulus of the superconducting currents flowing around the vortex, $J(r)$, is shown in Fig. 1.2 (c) and is expressed as

$$J(r) = \frac{\phi_0}{2\pi\mu_0\lambda^3}\mathrm{K}_1\left(\frac{r}{\lambda}\right), \tag{1.4}$$

where K_1 is the modified Bessel function of the second kind (order 1). As for the magnetic field, the currents decay exponentially when $r \gg \lambda$.

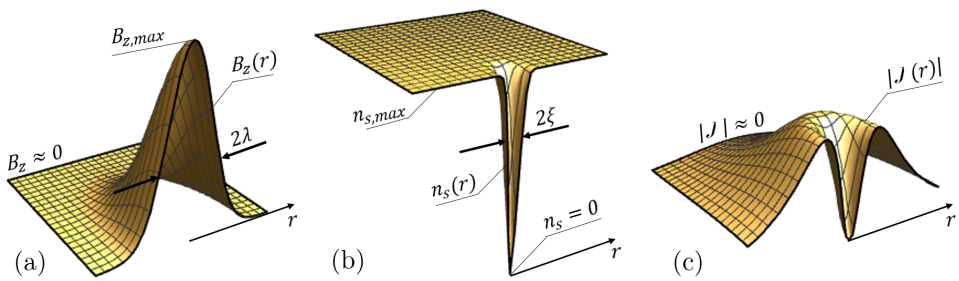

Figure 1.2: **Vortex in a type-II bulk superconductor.** (a) Magnetic field B_z and (b) superconducting electrons density n_s of a vortex as a function of the radial distance r, in a bulk superconductor with magnetic penetration depth λ and coherence length ξ. (c) Superconducting current density $J(r)$ of the current loops flowing around the vortex core.

In a homogeneous superconductor, the free energy per unit length ϵ_l associated with a vortex flux line is the sum of the contributions of the magnetic field, the kinetic energy of the supercurrents and the normal core. It is written as

$$\epsilon_\mathrm{l} = \frac{n^2\phi_0^2}{4\pi\mu_0\lambda^2}\left(\ln\left(\frac{\lambda}{\xi}\right) + \epsilon\right), \tag{1.5}$$

where n is the number of flux quanta carried by the vortex and ϵ is the core contribution. Therefore, since $\epsilon_\mathrm{l} \sim n^2$, it is not energetically favorable to have a vortex carrying $n \geq 2$ flux quanta in a homogeneous superconductor, compared to n single quantum vortices.

1.2.2.2 Forces acting on a vortex

The expression in Eq. (1.5) is valid for an isolated vortex. However, when two vortices are close enough (i.e., at distances on the order of λ), they start to feel each others current distribution and their interaction gives an additional contribution to ϵ_l. This causes a repulsive force $\mathbf{f}_\mathrm{int}$ to appear between vortices with the same polarity, i.e., with their field pointing in the same direction, while vortices with opposed polarities attract each other. Indeed, a vortex crossed by a superconducting current density $\mathbf{J}$ will feel a force per unit length $\mathbf{f}_\mathrm{L}$ perpendicular to the current, given by

$$\mathbf{f}_\mathrm{L} = \mathbf{J} \times \phi_n. \tag{1.6}$$

This force is often misleadingly called the Lorentz force, although it is not related to the force exerted by a magnetic field on a moving electric charge, since it is the supercurrent $\mathbf{J}$ that exerts a force on the vortex [8]. Note that the Lorentz force takes the same expression if the current density $\mathbf{J}$ has another origin than the vortices, for instance if it is applied to the material through a current source. Due to the repulsive interaction, vortices tend to maximize their separation, which means that in a homogeneous (pinning free) superconductor, the most stable configuration is a periodic triangular lattice [9].

However, the symmetry of the crystalline lattice or defects in the material might lead to different equilibrium configurations, since they cause spatial variations of ϵ_l. The local minima in the potential energy landscape constitute preferential sites for vortices and are therefore called pinning sites. A pinned vortex is trapped in the potential well with a pinning force $\mathbf{f}_\mathrm{p} \sim -\mathrm{d}\epsilon_\mathrm{l}/\mathrm{d}\mathbf{r}$. Pinning can arise from various phenomena, modifying one or several parameters in Eq. (1.5): defects (intrinsic or artificial), doping, irradiation, ionic implantation, magnetic pinning, etc. Controlling the pinning potential is notably of technological interest, because it helps to design materials with higher critical currents[1], closely related to the vortex motion.

In general, the total force per unit length $\mathbf{f}_\mathrm{tot}$ acting on a vortex is made of more contributions than those already mentioned:

$$\mathbf{f}_\mathrm{tot} = \mathbf{f}_\mathrm{int} + \mathbf{f}_\mathrm{L} + \mathbf{f}_\mathrm{p} + \mathbf{f}_\mathrm{d} + \mathbf{f}_\mathrm{M} + \mathbf{f}_\mathrm{T}. \tag{1.7}$$

The Lorentz and pinning forces, $\mathbf{f}_\mathrm{l}$ and $\mathbf{f}_\mathrm{p}$, as well as the force coming from the interaction between vortices, $\mathbf{f}_\mathrm{int}$, have already been described previously. The drag force $\mathbf{f}_\mathrm{d} \sim \mathbf{v}$ arises from the displacement of the vortex at a velocity $\mathbf{v}$ and will be addressed in the next section. The hydrodynamic Magnus force $\mathbf{f}_\mathrm{M} \sim \phi_0 \times \mathbf{v}$ appears

[1] In general, the critical current density J_c at which superconductivity is lost is smaller than the depairing current density J_dep necessary to break the Cooper pairs.

perpendicularly to the vortex motion [10] and is analogous to the force acting on a body rotating in a fluid. Finally, the random thermal fluctuations are responsible for the Brownian motion of the vortex around its equilibrium position [11], traduced by a random force $\mathbf{f}_\mathrm{T}$ in Eq. (1.7). The forces $\mathbf{f}_\mathrm{M}$ and $\mathbf{f}_\mathrm{T}$ are usually negligible, respectively provided that the velocity $\mathbf{v}$ is not too large and the temperature is below the activation temperature.

1.2.2.3 Dissipation produced by vortex motion

As anticipated when introducing Eq. (1.7), the displacement of vortices at velocity $\mathbf{v}$ under the action of a current $\mathbf{J}$ leads to energy dissipation. Indeed, the flux variation caused by the moving vortex induces an electric field $\mathbf{E}$ in the direction of $\mathbf{J}$, given by $\mathbf{E} = \mathbf{B} \times \mathbf{v}$, where $\mathbf{B}$ is the magnetic field of the vortex. Therefore, a difference of electrical potential appears and the resistance of the material becomes finite. This effect limits high currents applications of superconductors.

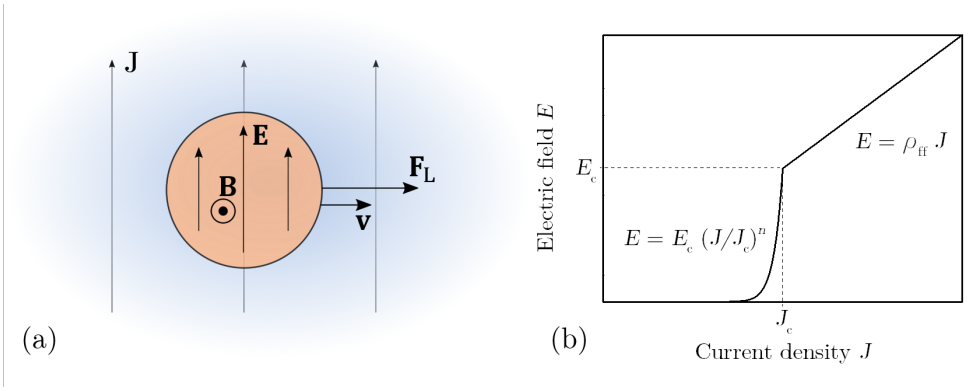

Figure 1.3: **Dissipation in moving vortices.** (a) Schematics of the microscopic origin of the dissipation in a vortex moving at a velocity $\mathbf{v}$ in a current density $\mathbf{J}$, under the action of the Lorentz force $\mathbf{F}_\mathrm{L}$. The variation of the magnetic field $\mathbf{B}$ causes an electric field $\mathbf{E}$ to appear in the same direction as $\mathbf{J}$, thus leading to a resistive behavior. (b) Phenomenological relation between J and the electric field E. J_c and E_c are respectively the critical electric field and the critical current density, and n is the creep exponent.

From a macroscopic point of view, i.e., considering a large ensemble of vortices and neglecting the fact that the field distribution is discretized, the electric field E and the applied current density J are related through a phenomenological highly non-linear expression when $J < J_\mathrm{c}$, a regime called flux creep:

$$E = E_\mathrm{c} \left(\frac{J}{J_\mathrm{c}} \right)^n , \tag{1.8}$$

where n is the creep exponent and E_c is the critical electric field. On the other hand, when $J > J_c$:

$$E = \rho_{ff} J \tag{1.9}$$

This is called the flux flow regime, characterized by a resistivity ρ_{ff}. The relation between E and J looks similar to Ohm's law in non-magnetic materials, but with the significant different that the resistivity ρ_{ff} increases with the magnetic field H:

$$\rho_{ff} = \rho_n H/H_{c2}, \tag{1.10}$$

where ρ_n is the resistivity of the normal state.

The microscopic origin of the dissipation is still debated, but according to the Bardeen-Stephen model, it comes from resistive phenomena taking place in the normal core of the vortex during its displacement [12]. This might be due to the fact that (i) part of the supercurrent is forced to transform to normal current to pass through the normal core of the vortex, or (ii) superconducting regions are destroyed at the vortex front, to be reformed at the back [13, 14]. The energy dissipation gives rise to a viscous drag force opposing the vortex motion:

$$\mathbf{f}_d = -\eta \mathbf{v}, \tag{1.11}$$

where η represents the drag coefficient from the homogeneous superconducting medium. It has to be noted that since vortex mass is negligibly small [15], damping forces dominate the dynamics. In other words, vortex motion occurs in an overdamped regime where inertia plays no role.

1.3 Smooth flux penetration in superconductors

In typical magneto-optical imaging experiments, a superconductor is submitted to magnetic fields H changing in magnitude. It is therefore important to understand how flux penetrates into the sample, since the images essentially show the magnetic field distribution of the sample.

1.3.1 Bulk superconductors

In a homogeneous superconductor where pinning is absent, when the applied field $H > H_{c1}$, vortices enter the sample from the border and tend to spread to minimize their interaction energy. However, in real superconductors, intrinsic pinning is always present, so that flux entering through the borders of the material upon increasing H is trapped by the pinning centers and does not readily exit when H is decreased.

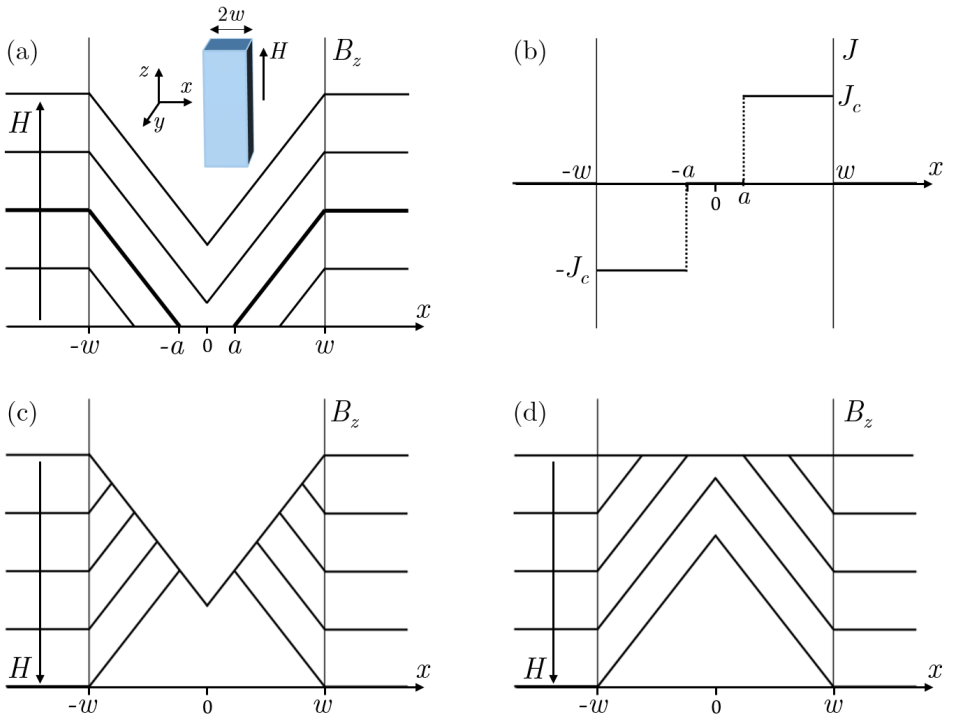

Figure 1.4: **Flux penetration in a bulk superconductor.** (a) Flux penetration in a long superconducting slab of width $2w$ for several values of the applied field H. The position of the flux front is $x = \pm a(H)$. (b) Current distribution corresponding to the profile in bold in panel (a). (c) Magnetic field distribution upon decreasing H. (d) Flux distribution when the field is decreased after field cooling. Zero field cooling corresponds to the situation in panel (a).

A simple model, proposed by Bean [16], describes the flux penetration in a superconductor where pinning is strong, assuming that vortex motion is negligible. This is equivalent to a system where the creep exponent $n = \infty$, i.e., vortices do not move unless $J > J_c$. Moreover, this model assumes that $H_{c1} = 0$ and the surface barrier for flux penetration [17] is not taken into account. When H is increased, vortices enter through the sample border and screening currents J flow around the sample. As the currents push the vortices towards the sample center, they are pinned by the closest available pinning sites. When H is further increased, additional flux penetrating into the sample pushes the vortices, moving from one pinning site to the next available one. The Bean model assumes that wherever there are currents, $J = J_c$. While J_c is in first approximation independent of H, more refined models account for the field dependence [18, 19].

The magnetic field distribution in the sample is determined with Ampère's law:

$$\nabla \times \mathbf{B} = \mu_0 \mathbf{J}. \tag{1.12}$$

To illustrate on a concrete example, let us consider the general situation, depicted in Fig. 1.4 (a), of a superconducting slab of width $2w$ with its principal axis aligned with the applied field $\mathbf{H} = H\mathbf{e}_z$. In this situation, since the screening currents flow parallel to the sample border, along the y-direction, Eq. (1.12) becomes

$$\frac{\mathrm{d}B_z}{\mathrm{d}x} = \mu_0 J. \tag{1.13}$$

The modulus of the magnetic field gradient is constant and given by the critical current. Therefore, since $B_z = \mu_0 H$ at the edge of the sample, the magnetic field takes the following expression, with the reference of the coordinates at the center of the sample:

$$B_z(x) = \begin{cases} \mu_0 H & \text{if } |x| > w \\ \mu_0 \left(|x| - a\right) J_\mathrm{c} & \text{if } w > |x| > a \\ 0 & \text{if } |x| < a. \end{cases} \tag{1.14}$$

The position $a(H)$ of the flux front is given by

$$a(H) = w - \frac{H}{J_\mathrm{c}}. \tag{1.15}$$

The current is written as

$$J(x) = \begin{cases} \frac{x}{|x|} J_\mathrm{c} & \text{if } w > |x| > a \\ 0 & \text{if } |x| < a. \end{cases} \tag{1.16}$$

Screening currents flow only in the slice along the edge where flux has penetrated.

The magnetic field and current distributions are represented in Fig. 1.4 (a) and (b) for several values of H. When H is larger than the field necessary to have full penetration in the sample, the exceeding flux spreads over the whole sample in order to keep the gradient constant. When H is decreased starting from a situation where flux is already trapped in the sample, flux leaves the sample from the borders, but the field gradient is still equal to $\pm\mu_0 J_\mathrm{c}$, as shown in Fig. 1.4 (c). From this, it is easy to understand that in general, applying a magnetic field to a superconductor at $T < T_\mathrm{c}$ (zero field cooling, or ZFC) is different from applying H at $T > T_\mathrm{c}$ before cooling the sample to $T < T_\mathrm{c}$ (field cooling, or FC). Indeed, while the first case corresponds to the situation presented in Fig. 1.4 (a), in the latter case, the flux distribution is constant over the whole sample before the flux is decreased, as illustrated in Fig. 1.4 (d).

1.3.2 Thin films

Depending on the shape and size of the superconductor, some material properties might change considerably, in particular as far as flux penetration is concerned. In this thesis, we work with thin superconducting films, having a thickness t comparable to λ. In this situation, the screening currents are spatially confined by the thickness of the film and lose some efficiency to shield magnetic fields. It is therefore convenient to define a new parameter accounting for the reduction of the magnetic shielding, called the effective penetration length Λ and given by

$$\Lambda = \frac{\lambda^2}{t}. \tag{1.17}$$

This expression is valid as long as $t \ll \lambda$. The flux penetration is therefore modified compared to bulk superconductors. Moreover, when t is small enough, type-I superconductors might behave as type-II superconductors. Indeed, the effective Ginzburg-Landau parameter κ_{eff} is given by

$$\kappa_{\text{eff}} = \frac{\Lambda}{\xi}, \tag{1.18}$$

so a superconductor with $\kappa < 1/\sqrt{2}$ might have $\kappa_{\text{eff}} > 1/\sqrt{2}$ when geometrically constrained.

The confinement of the screening currents in the out-of-plane direction also affects the magnetic field distribution of vortices. Due to the less efficient screening, the field is more spread out and the current loops around the vortex core extend further than for a bulk superconductor vortex [20]. At a distance $r \gg \Lambda$ from the vortex core, the magnetic field decays as $1/r^3$, whereas the current intensity goes as $1/r^2$:

$$B_z(r) \simeq \frac{2\phi_0\Lambda}{\pi r^3}. \tag{1.19}$$

This leads to a long range $1/r^2$ interaction between vortices in thin films, also called Pearl vortices, compared to the e^{-r} interaction between Abrikosov vortices in bulk superconductors. On the other hand, when $\xi < r < \Lambda$, the magnetic field is approximately given by

$$B_z(r) \simeq \frac{\phi_0}{4\pi\Lambda r}. \tag{1.20}$$

While these results where obtained in the situation where $t \ll \lambda$, the qualitative conclusions still hold when $t \sim \lambda$ [21].

Another difference with bulk superconductors is that demagnetization effects take place. Depending on the particular geometry of the thin film, they can lead to a

substantial enhancement of the effective magnetic field H_{eff} close to the sample borders:

$$H_{\text{eff}} = \frac{H}{1-N}, \tag{1.21}$$

where N is the demagnetization factor[2]. This is illustrated in Fig. 1.5 (a) for a thin superconducting film in a perpendicular magnetic field. In a long superconducting slab, as the one considered in Fig. 1.4, $N \sim 0$ and $H_{\text{eff}} \simeq H$: the field at the edge of the superconductor is equal to the applied field. In a thin stripe of thickness t and width $2w$, a geometry close to the square thin films considered in this work, $N = 1 - t/w$ [22]. Since t is much smaller than w in our samples, $N \simeq 1$ and $H_{\text{eff}} \gg H$. For this reason, vortices penetrate in thin films at applied fields much smaller than H_{c1}.

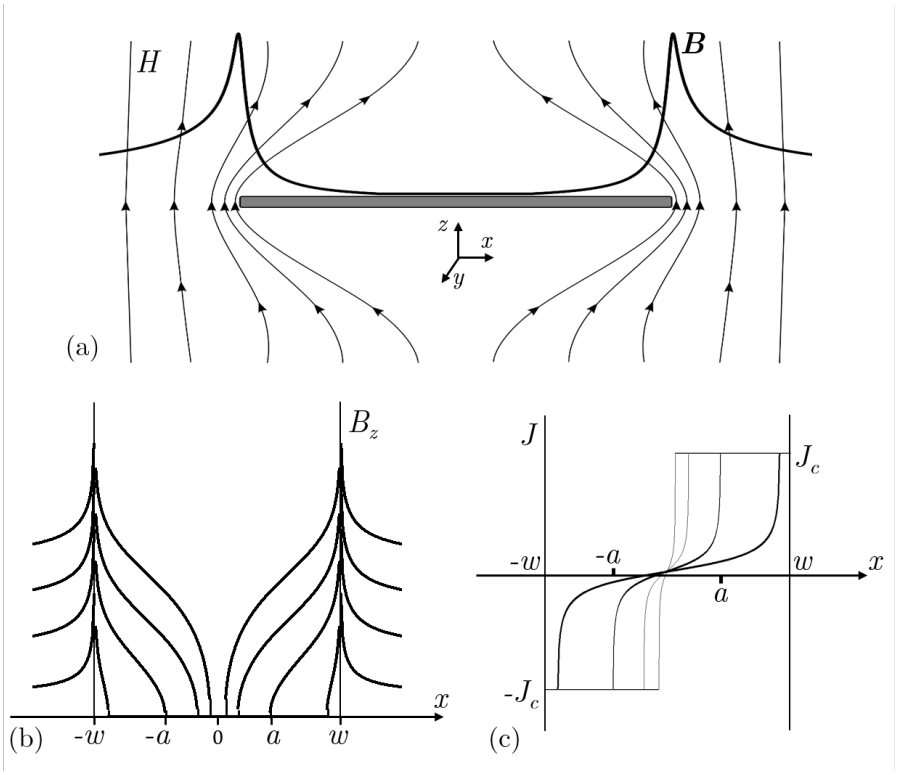

Figure 1.5: **Particularities of the thin film geometry.** (a) Demagnetization effects reinforcing the magnetic field at the border of a thin film of width $2w$. The applied field H is represented by the arrows, while the field profile B is shown with a green line. (b) Flux penetration in a thin film for several values of H. The position of the flux front is $x = \pm a(H)$. (c) Current distributions corresponding to the H values of panel (b).

[2]This is in general a tensor, but in the case of an ellipsoid of revolution, the demagnetization tensor reduces to a single number N. For a thin film, we consider an oblate ellipsoid with one axis much shorter than the two others.

All these effects cause the flux penetration to differ significantly in thin films compared to bulk superconductors, since the magnetic field is enhanced at the sample border and currents flow everywhere in the sample due to the weaker screening. The out-of-plane magnetic field distribution takes the following expression [23]:

$$B_z(x) = \begin{cases} \mu_0 H_g \operatorname{arctanh}\left(\frac{|x|}{w}\sqrt{\frac{w^2-a^2}{x^2-a^2}}\right) & \text{if } |x| > w \\ \mu_0 H_g \operatorname{arctanh}\left(\frac{w}{|x|}\sqrt{\frac{x^2-a^2}{w^2-a^2}}\right) & \text{if } w > |x| > a \\ 0 & \text{if } |x| < a, \end{cases} \tag{1.22}$$

where $H_g = J_c t/\pi$ and a is the distance between the flux front and the sample center, given by

$$a(H) = \frac{w}{\cosh\left(\frac{H}{H_g}\right)}. \tag{1.23}$$

The currents flow all over the sample once a magnetic field is applied:

$$J(x) = \begin{cases} \frac{x}{|x|} J_c & \text{if } w > |x| > a \\ \frac{2}{\pi} \arctan\left(\frac{x}{w}\sqrt{\frac{w^2-a^2}{a^2-x^2}}\right) J_c & \text{if } |x| < a. \end{cases} \tag{1.24}$$

While the model presented in this section accurately accounts for the flux distribution in isothermal conditions, it is no longer valid when flux enters in sudden bursts, such as in thermomagnetic instabilities. These flux avalanches occurring at low temperatures are described in the next section.

1.4 Thermomagnetic instabilities

In this section, we give a qualitative description of the reorganization of flux in the smooth penetration regime (Bean model), occurring through dynamically driven flux avalanches in isothermal conditions. We then move to thermally driven flux avalanches, where thermomagnetic instabilities play a crucial role.

1.4.1 Dynamically driven flux avalanches

The Bean model accounts for the static flux distribution for a given applied field H, but it does not give any information about the dynamics of the system. In other words, when H is slightly increased, vortices move to accommodate the field increase, but the way this reorganization occurs is not addressed, only the final state is described.

Actually, the kind of organization found in the vortex state is not particular to superconductors, but it is found in a wide range of systems, from sand piles to earthquakes or financial markets, and is called self-organized criticality [24,25]. For instance,

when sand grains are added on top of a pile, the system reorganizes to keep the slope of the pile constant. The additional grains might lead to a local slope exceeding the critical slope, hence local avalanches trigger to decrease the slope. Local variations of the slope make it impossible to predict how the system will react upon the addition of a new sand grain. The probability P of an event involving s grains (the size of the avalanche) is given by $P(s) \sim s^{-\alpha}$, where α is the critical exponent. The value of α is representative of the system under study and is said to be universal, in the sense that small changes in the system will not change the outcome and the stationary state, due to the self-organization. Knowing the behavior of the single units is not enough to predict the complex phenomena arising from the interactions between the many constitutive units of the system. The system has a highly non linear response to small perturbations, since the addition of a single unit might trigger an event of any size, from small to big. Note that the system finds an equilibrium which is far from the state of minimum energy, corresponding to a flat sand surface. This happens when the friction between the grains compensates the gravity pulling them to the bottom of the pile.

In superconductors, the elementary units of the system are vortices, playing the role of the sand grains. According to the Bean model, the vortices arrange themselves in order to keep the magnetic field gradient constant. In other words, when the slope of the field distribution, dictated by the value of the critical current, increases locally due to incoming vortices, reorganization occurs through small flux jumps, similar to reorganization in a sand pile. In a superconductor, the Lorentz force pushing the vortices towards the sample center is the analogue of gravity in the sand pile, while pinning corresponds to the friction between sand grains, preventing the vortices to move. The value of α is close to 1 for an ideal sand pile and it ranges from 1 to 3 for flux penetration as described by the Bean model [25]. Note that although the analogy of the sand pile is closest to the flux penetration in a bulk superconductor, where the field gradient is constant, the same discussion is valid in the case of a thin film, where the system will adapt to follow the flux penetration described by Eq. (1.22).

The small flux jumps described in this section are also called dynamically driven flux avalanches, since they rely on the balance between the pinning force and the Lorentz force and do not lead to significant dissipation in the system. In opposition, another type of avalanches, called thermally driven flux avalanches, takes places under some circumstances, when thermal effects start to play a significant role.

1.4.2 Thermally driven flux avalanches

In the dynamically driven flux avalanches we just described, thermal effects have little importance and the magnetic field distribution can be understood by invoking only

electromagnetics. In other words, the heat produced by the motion of vortices is efficiently evacuated, meaning that the thermal diffusivity $D_\mathrm{t} = \kappa/C$ is much larger than the magnetic diffusivity $D_\mathrm{m} = 1/\mu_0\sigma$, where κ, C and σ are respectively the heat conductivity, the volumetric heat capacity and the normal state electric conductivity of the superconductor. The ratio between these two coefficients leads to the definition of the parameter τ [26]:

$$\tau = \frac{D_t}{D_m} = \frac{\mu_0\kappa\sigma}{C}. \tag{1.25}$$

Note that this parameter, while useful for the sake of keeping the discussion simple, does not capture all the complex physics behind flux avalanches, as its neglects key parameters such as the heat transfer to the substrate, the sample geometry and the critical current, to name a few.

Up to now, we considered the situation where $\tau \gg 1$, represented in the left image of Fig. 1.6. However, the flux penetration drastically changes when heat cannot be efficiently removed, i.e., when $\tau \ll 1$. In that case, when the applied magnetic field H is increased by a small amount δH, vortices move towards the sample center and energy dissipation occurs in the normal vortex cores, as described in section 1.2.2.3. The released heat δQ causes the temperature to rise locally by an amount δT, since heat is not efficiently removed, either due to poor thermal conductivity or bad thermal sink with the substrate. This leads to a reduction of the critical current density $J_\mathrm{c}(T)$ and the pinning force $f_\mathrm{p}(T)$, both easing the penetration of flux from the sample borders and the displacement of vortices already inside the material. As more flux enters and screening is weaker, more electric field is induced, according to Faraday's law, and heat dissipation is reinforced. This positive feedback loop leads to catastrophic events called flux avalanches, shown in the image on the right side of Fig. 1.6. Flux bursts at once into the sample at high velocities, increasing locally the temperature, in some cases even over T_c according to numerical simulations [27].

The feedback loop stops and the situation reaches an equilibrium as the flux advances towards the sample centre. On the one hand, as the intensity of the screening currents decreases, the force driving the vortices becomes weaker, naturally putting an end to the progression of the flux avalanche. On the other hand, as more and more flux enters in the sample, the flux gradient at the sample border decreases, leading to a reduction of the induced electric field responsible for heat release. The whole process, from the triggering of the avalanche to the stationary state, typically lasts for about hundred nanoseconds, as flux propagates at high velocities. For instance, in YBCO thin films, the velocity can peak over 100 km/s at the beginning of the avalanche, and it is around 20 km/s on average [28]. Similar values are found by numerical simulations in a MgB_2 film, where the average propagation velocity is on the order of 14 km/s [29].

Flux avalanches are an intrinsically stochastic phenomenon: the exact location

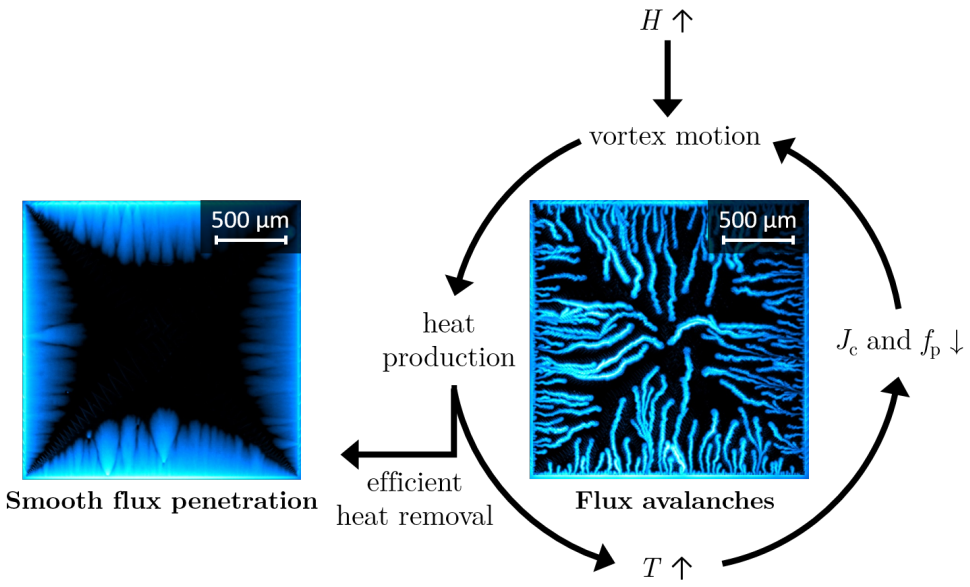

Figure 1.6: **Thermomagnetic instabilities in superconductors.** When the applied magnetic field H is increased, vortices are forced to move and dissipation occurs in their normal cores. If the produced heat is efficiently removed, smooth flux penetration described by the Bean model occurs, as shown in the image on the left representing a 2×2 mm^2 square Nb film. Otherwise, the local increase in the temperature T weakens the pinning force f_p and the critical current J_c, thus reinforcing the vortex motion. This positive feedback loop leads to thermomagnetic instabilities and flux avalanches, represented in the image on the right.

where they appear cannot be predicted, nor reproduced from one experiment to another [30, 31]. They are similar to other relaxation phenomena in nature, such as snow avalanches and thunder for instance. Indeed, in all cases, the system relaxes from a metastable state (the critical state in superconductors) through a catastrophic phenomenon involving a large energy release. In snow avalanches, snow piles up due to friction, until the weight is too important and the pack of snow sweeps down the slope, converting potential energy into kinetic energy. In thunder, the accumulation of electric charges is disrupted by a large discharge, when the gradient of electric potential is too large to be sustained. Flux avalanches also present similarities with branching electric discharges, also known as Lichtenberg figures [32]. Note however that in these examples, thermal effects play no role, in opposition to what happens in flux avalanches.

Formally, thermomagnetic instabilities can be described by coupling the equations of electromagnetism and the thermal diffusion equation, in the so-called thermomagnetic model [33–35]. These equations link the magnetic field $\mathbf{B}$, the electric field $\mathbf{E}$,

the temperature T and the current density $\mathbf{J}$ in a thin film for an out-of-plane applied field H:

$$\nabla \times \mathbf{E} = -\frac{\mathrm{d}\mathbf{B}}{\mathrm{d}t} \tag{1.26}$$

$$\nabla \cdot \mathbf{B} = 0 \tag{1.27}$$

$$\nabla \times \mathbf{B} = \mu_0 \mathbf{j} \delta(z) \tag{1.28}$$

$$c\frac{\mathrm{d}T}{\mathrm{d}t} = \kappa \nabla^2 T - \frac{h_0}{t}(T - T_0) + \frac{\mathbf{j} \cdot \mathbf{E}}{t}. \tag{1.29}$$

The sheet current is $\mathbf{j} = \mathbf{J}t$ and satisfies the equation $\nabla \cdot \mathbf{j} = 0$. Temporal variations of the temperature in the sample comes from the thermal diffusion in the sample, the heat transfer between the sample and the environment, typically through the substrate, and the dissipation in the sample. T_0 is the substrate temperature and h_0 (in W K^{-1} m^{-2}) depends on the thermal link between sample and substrate. The dependence of the electric field on the current is given by Eq. (1.8). Other models exist to account for the formation of thermomagnetic instabilities, such as the shock wave model [36], but the thermomagnetic model has been the most successful in describing correctly the morphology of flux avalanches and its temperature dependence.

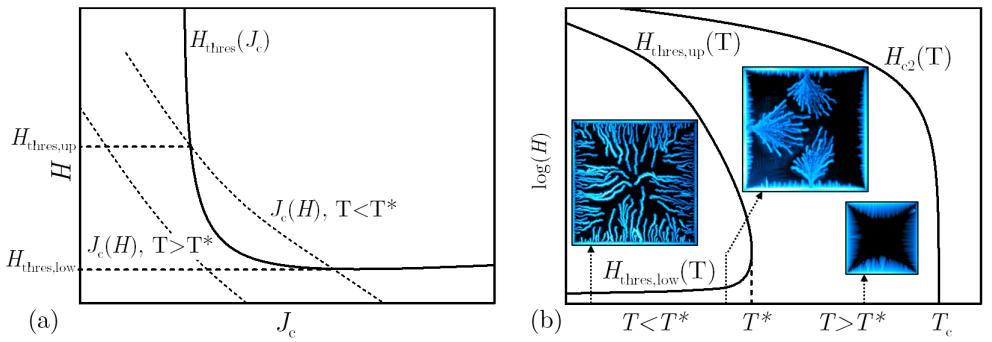

Figure 1.7: **Phase diagram of flux avalanches.** (a) The threshold field for triggering flux avalanches, $H_{\mathrm{thres}}(J_c)$, is plotted according to Eq. (1.30). The dependence of J_c on the applied field H is represented for two temperatures: $T > T^*$, where H is always smaller than H_{thres} (no avalanches), and $T < T^*$, where H is larger than H_{thres} between the lower and upper threshold fields, respectively $H_{\mathrm{thres,low}}$ and $H_{\mathrm{thres,up}}$. In panel (b), the regions of the $H(T)$ diagram where flux avalanches occur is represented, as well as the upper critical field H_{c2}. Avalanches do not take place when T is larger than T^*. The insets illustrate the flux penetration in a 2×2 mm^2 square Nb film for different temperatures, marked by the dashed arrows.

Flux avalanches are quite sensitive to the parameters of the system, such as the geometry of the sample, the material composition, the temperature, the thermal link to the environment and the field ramp rate [37], to name a few. As captured by Eq. (1.29), a bad thermal link between the sample and the substrate, as well as the decrease in C

and κ occurring at low temperatures will favor flux avalanches. Moreover, J_c and its dependence on the temperature also play an important role [26]. It has been shown that the dimensions of the thin film are relevant parameters for the apparition of flux avalanches, as in general, the larger the area of the film and the thinner it is, the lower the field necessary to trigger flux avalanches [31]. For a superconducting films of width $2w$, the threshold field H_{thres} above which avalanches occur is given by [31]

$$H_{\text{thres}} = \frac{J_c t}{\pi} \arccos\left(\frac{w}{w - l^*}\right), \tag{1.30}$$

where l^* is a threshold length, corresponding to the distance between the flux penetration front and the sample border when the first avalanche triggers, and is written as

$$l^* = \frac{\pi}{2\left(\sqrt{\frac{EJ_c}{\kappa T^*}} - \sqrt{\frac{2h_0}{\kappa n t}}\right)}. \tag{1.31}$$

When the magnetic field is low, i.e., when flux has penetrated a distance $l < l^*$ in the sample, the thermomagnetic model only gives stable solutions, meaning that perturbations do not grow in time. On the contrary, when $l > l^*$, the field distribution can become unstable and flux avalanches may occur.

The dependence of H_{thres} on the critical current J_c is represented in Fig. 1.7 (a). Since J_c depends on H and T, there is a well-defined region in the $H(T)$ phase diagram where flux avalanches exist, as represented in Fig. 1.7 (b). Indeed, if $J_c(H)$ curves are plotted in the $H(J_c)$ diagram of panel (a) for different temperatures, it is clear that for $T > T^*$, H_{thres} cannot be reached, regardless of the H value. For $T < T^*$, H_{thres} is reached upon increasing the applied field, defining a lower threshold for the appearance of flux avalanches. Reciprocally, when the field is high enough, H_{thres} becomes larger than H again, defining an upper threshold field above which avalanches do not occur anymore. Avalanches show a variety of morphologies, namely depending on the temperature, the material and the presence of artificial pinning centers. In general, avalanches tend to be small with few branches at low temperature, while close to T^*, bigger avalanches with many branches appear [30]. This is illustrated in the insets of Fig. 1.7 (b).

Chapter 2

Experimental techniques

Popular summary

Two basic ingredients are required in order to perform successful experiments on superconducting materials. Firstly, superconductivity does not (yet) exist at room temperature, meaning that materials need to be cooled down to very low temperatures, around $-269°C$, to actually turn them into the superconducting state. This is achieved thanks to a cryostat, working pretty much as a regular fridge, but capable of keeping the temperature stable down to a few thousandths of degrees. Another important point is that the samples, the pieces of material we place in the cryostat, are usually only a few millimeters large, since the available space is limited. They also need to be under a high vacuum, where the pressure at least a million times smaller than the atmospheric pressure.

Secondly, once the sample is in the superconducting state, techniques permitting to access to the interior of the cryostat have to be employed to make observations. In this work, we are mainly interested to see how materials behave when they are immersed in a magnetic field. To that end, we use a technique called magneto-optical imaging. Observing a material by magneto-optical imaging is like a traditional observation with a microscope, except that instead of showing the defects and roughness of the material surface, evidenced by light scattering, the technique provides us with images of the magnetic field. These images show bright colors where the magnetic field is strong, while dark spots correspond to places where there is little or no field. The magnetic signal is converted to optical signal using a particular compound called indicator, which is placed on top of the material under study. While they look similar to glass, because of their transparency, the best indicators are usually complex crystals designed to affect light where magnetic field is present. One of the advantages of magneto-optical imaging is that it allows to visualize in real time how the magnetic field is changing in the whole material, which might be as big as a few millimeters squared, while seeing details as small as a few micrometers and detecting fields weaker than that of the earth.

Magneto-optical images are composed of pixels whose intensity is proportional to the magnetic field strength, but unfortunately they do not directly give the field value. Therefore, we propose a method to convert the pixel intensity into magnetic field, by calibrating our system in a well-known magnetic field source, such as a coil fed by an electric current. Interestingly, when a superconductor is combined with a permanent magnetic material, our method enables us to discern the magnetic field contribution coming from the magnet from that originated by the superconductor. Finally, since unavoidable defects in the indicator and in the sample often degrade the quality of the images, we present some techniques to correct them and improve the images.

2.1 Introduction

This chapter focuses on the key experimental techniques used throughout this work. Since the study of superconducting samples requires low temperatures, the first part is devoted to the cryogenic systems with a particular attention to the closed cycle cryostat available in our facilities in the group of Experimental Physics of Nanostructured Materials (University of Liège). The second part describes the magneto-optical imaging technique, the main observation method employed to image the magnetic field distribution in superconductors and in magnetic materials. The information concerning the samples fabrication is presented along with the corresponding results in the following chapters.

First, the general functioning of a closed cycle cryostat is explained and the characteristics and limitations of our system are exposed. In view of the relatively weak cooling power provided by our cryostat, the problematic of the sample installation is also addressed, since it plays an important role, especially if the base temperature is to be reached. Finally, as some experiments were performed in the group of Prof. W. A. Ortiz at UFSCar (Brazil), the liquid helium cryostat available there is briefly presented.

Magneto-optical imaging is based on the Faraday effect, occurring more prominently in dielectric materials, causing the rotation of the polarization of linearly polarized light propagating in a magnetic field. This effect is exploited to record near real-time images of the magnetic field distribution in macroscopic samples, with a good compromise between spatial resolution and field sensitivity. The general physical principles of magneto-optical imaging are explained, then the crucial role played by the indicators is described. Indeed, since the Faraday effect is weak in most materials, the observation of magnetic fields through magneto-optical imaging is strongly dependent on the quality of indicator films placed on top of the sample, designed to cause a large rotation of light polarization when a field is applied. The different types of indicators are reviewed, but particular attention is laid on the Bi:YIG based indicators on which this work relies, with a characterization of their optical properties. Subsequently, the magneto-optical imaging setup at our facilities is described and compared to other setups, namely by computing quantities such as the extinction ratio and the sensitivity.

At the end of the chapter, we develop the data processing. We first describe the basic data acquisition and analysis procedures, illustrated on a concrete example where the signal-to-noise ratio is improved step by step through post-processing of the images. After that, we explain how the spatial resolution and magnetic signal can be enhanced during the data acquisition by reducing the gap between the indicator and the sample through mechanical pressing. Finally, we present a technique to convert

raw images, where the pixel intensity is proportional to the magnetic field, to actual magnetic field distributions, and we apply it to various samples. This method differs from the typical quantitative magneto-optical imaging techniques, since it allows to isolate the contribution of a superconductor from constant sources of magnetic field, such as magnetic layers.

In some situations, magneto-optical imaging data has been complemented and compared with other magnetic field sensitive techniques: magnetic force microscopy (MFM), scanning Hall probe microscopy (SHPM) and magnetization measurements (SQUID). MFM is performed exclusively at room temperature and has the advantage of a higher spatial resolution compared to magneto-optical imaging. It is therefore mostly employed to characterize the magnetic domains in magnetic films. SHPM and SQUID measurements have been carried both at room and low temperatures. Therefore, SHPM can be used to image locally the magnetic field distribution in superconductors and hybrid structures, while SQUID measurements probes the global response of samples in a magnetic field of a few teslas. A short description of these complementary techniques is included in the chapters where they first appear.

2.2 Cryogenics

The low temperatures, required namely to access the superconducting state, are achieved within two types of optical cryostats: a helium closed cycle cryostat, available at our facilities at the University of Liège, and a liquid helium cryostat for the measurements carried in the group of Prof. W. A. Ortiz, at the Federal University of São Carlos, Brazil. While the first has the advantage to be independent of costly liquid helium supply and more flexible for the experiments planning, the latter offers a larger cooling power and a lower base temperature. Since most experiments have been carried in the closed cycle cryostat in our laboratory, it is the main focus of this section, whose contents are mainly based on the Cryostation user manual and the online Knowledge Base of Montana Instruments [38]. The principles behind the operation of cryogen free cryostats are reviewed and a description of the main components of the system is given, along with the equipment characteristics. Sample mounting is also addressed, since it plays a crucial role in the success of the experiments.

Our laboratory is equipped with a commercial helium closed cycle Cryostation, commercialized by Montana instruments. Our customized configuration, basically consisting in the base system with an extended connection between the cryocooler and the sample chamber, maximizes the optical access to the sample required for magneto-optical imaging. Moreover, the system has been modified with the so-called "round castle" option extending the sample chamber in height, so the sample can be easily positioned in the bore of a coil surrounding the castle. A global view of the

cryostat, as well as a zoom on the sample chamber in the "round castle" configuration, are represented in Fig. 2.1 (a) and Fig. 2.1 (b), respectively. In this configuration, the cryostat achieves a minimum base temperature of 3.5 K with a stability of 10 mK for extended periods of time, while providing optical and electrical access to the sample, as well as low vibration levels with a maximum peak-to-peak amplitude of 5 nm. Changing the system to the base configuration, shown in Fig. 2.1 (c), enhances the temperature stability to approximately 0.2 mK, but at the expenses of the magnetic field magnitude and homogeneity, as discussed in section 2.3.3.2.

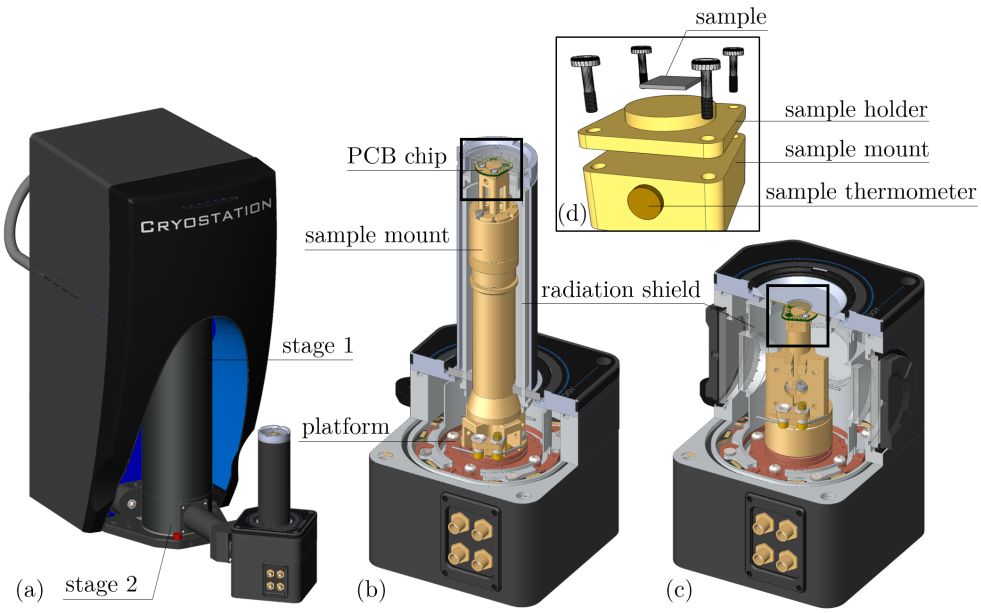

Figure 2.1: **Schematic view of the cryostat unit.** (a) Cryostat unit, encompassing the cryocooler and the sample chamber, in the "round castle" configuration. (b) Sample chamber in the "round castle" configuration. The sample is installed on top of the round sample mount. (c) Sample chamber in the base configuration. (d) Zoom on the area enclosed by the black frames, showing details of the removable parts involved in the sample mounting. Panels (a-c) are reproduced here with the courtesy of Montana Instruments.

The setup, as schematically represented in Fig. 2.2, consists in four main parts: the user interface, the control unit, the compressor and the cryostat itself. The control unit ensures communication between the other components and a computer, where a user interface enables control over the entire equipment. It also hosts the vacuum system, responsible for pumping and venting the sample chamber. The compressor manages the helium gas supply to the cryocooler and evacuates the heat from the returning helium. The cryostat unit, represented in Fig. 2.1 (a), is the only part of

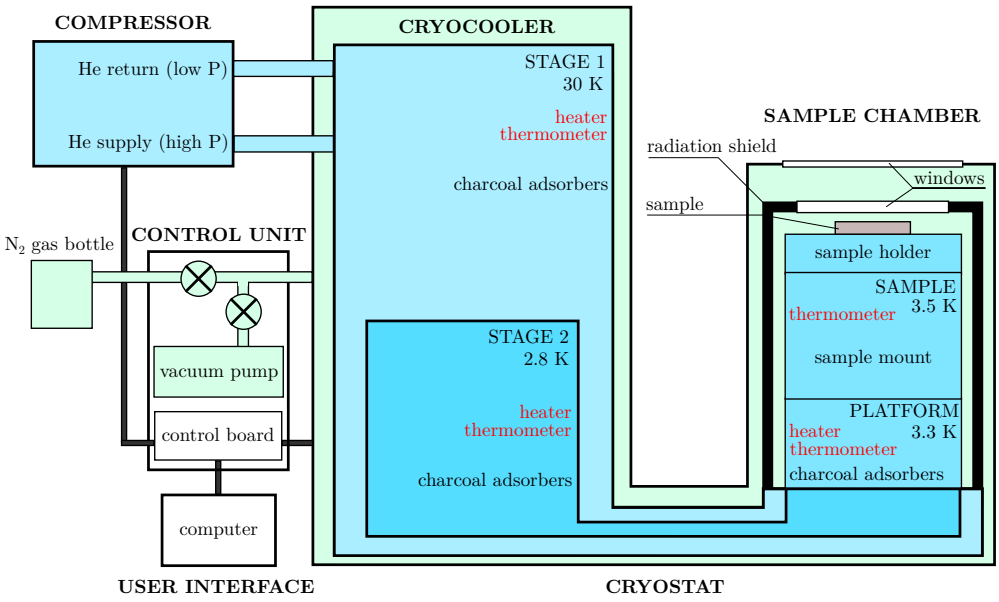

Figure 2.2: **Schematic view of the helium closed cycle cryostat with optical access.** It consists in four main parts: the control unit, the compressor and the cryostat, controlled by the user interface. The vacuum system is colored in green, while the parts involved in the cooling procedure are represented in blue. A range of thermometers and heaters monitor and regulate the temperature at the cryocooler stages and in the sample chamber, while a radiation shield blocks most of the infrared radiation coming from the environment.

the system mounted on top of an optical table, to ensure a minimum of vibrations. It consists of the sample chamber and the two-stage cryocooler, removing heat from the sample chamber based on the Gifford-McMahon cycle.

2.2.1 Cooling principles: the Gifford-McMahon cycle

The heart of the cooling process lies in the cryocooler, a RDK-101D model commercialized by SHI Cryogenics Group. The cryocooler is connected to the compressor via two pressurized pipes: one of them supplies the helium gas at a high pressure (around 20 bar), while the other returns it at a lower pressure (around 6 bar). At the other extremity, the cryocooler is in contact with the sample space, where the low temperatures are actually needed. The description of the Gifford-McMahon cycle presented here has been simplified, but without loosing the essence of the physical principles. The reader interested in the details can find a more advanced discussion in the original work of W. E. Gifford [39].

The Gifford-McMahon cycle consists in four steps, numbered from 1 to 4 in Fig. 2.3. The central idea is to reduce the temperature of helium gas by isentropic expansion,

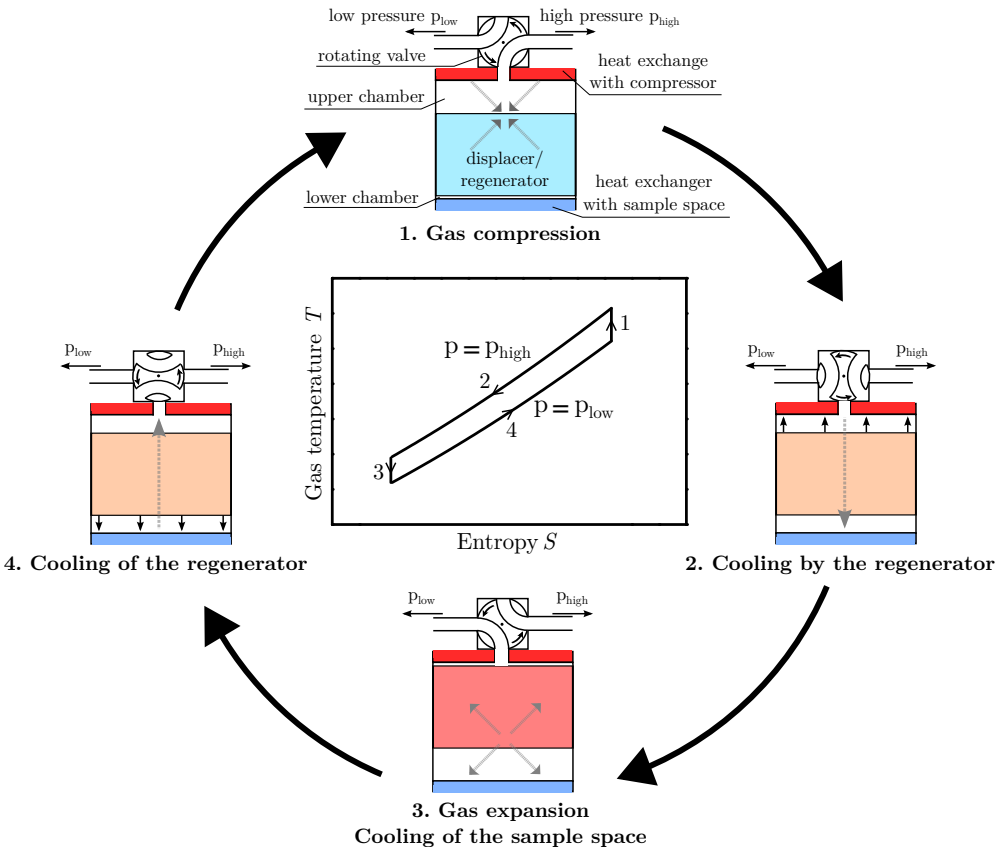

Figure 2.3: **The Gifford-McMahon cycle.** The cycle is represented in the temperature T vs entropy S graph, where the numbers correspond to the key steps illustrated around the graph. It relies on the isentropic expansion and compression of helium gas, forced to pass through a moving displacer (combined with a regenerator). (1) The chamber is connected to the high pressure helium supply, thus helium gas is compressed and releases heat to the compressor. (2) The displacement of the cold regenerator forces the gas to move to the lower chamber and to exchange heat in the process. (3) The low pressure inlet is connected and the gas expands, decreasing its temperature and thus cooling the sample space. (4) The gas is forced to move to the upper chamber and takes up heat from the regenerator.

as illustrated in the graph, and by heat exchange also the temperature of the sample space. The cryocooler that is schematically represented in the four panels of Fig. 2.3 consists in a chamber where a displacer oscillates periodically, in phase with a rotating valve connecting alternatively the low and high helium pressure outlets from the compressor to the chamber. In most designs, the displacer is actually also a regenerator, a porous material that should ideally have a high thermal conductivity to transfer heat to/from the gas, as well as a small resistance to the gas flow. Note that these two

requirements are quite contradictory in terms of material engineering.

In step 1, represented in Fig 2.3, the displacer is in the lowest position and the chamber is connected to the high pressure outlet. The helium gas is thus compressed inside the upper chamber. This process increases the temperature of the gas, and heat is transferred from the gas to the compressor. At this point, the regenerator is already cold as a result of the previous cycle. During step 2, the displacer moves towards the upper chamber, and the gas is forced to pass through the regenerator, thus exchanging heat in the process. In step 3, the displacer is in the upper position and the low pressure outlet is connected to the chamber. As a result, the helium gas present in the lower chamber expands and cools down in the process. The gas therefore takes up some heat from the warmer sample space, whose temperature decreases. During step 4, the displacer moves towards the lower chamber, forcing the gas to cool it as it passes through it, resulting in the gas warming up.

Globally, the cycle results in a decrease of the temperature of the sample chamber (step 3), while the temperature increases at the compressor (step 1). The excess heat is however evacuated through air-cooling. Also, the displacer/regenerator oscillates periodically as the system goes through cycles, thus alternatively storing and releasing heat, at a typical frequency of 70 Hz. One of the advantages of the Gifford-McMahon cycle is that it may be implemented in series. Indeed, instead of connecting the lower chamber to the sample space, it might be attached to the upper chamber of a second cryocooler. The lower chamber of this second stage is then in contact with the sample space. In our system, consisting of two stages assembled in series, stage 1 goes from room temperature to $\sim$ 30 K, while stage 2 brings the temperature from $\sim$ 30 K to $\sim$ 2.8 K. Their respective cooling power is 3 W and 0.1 W.

2.2.2 Cryostat operation

Low temperatures can only be reached provided the sample chamber is in high vacuum, to reduce the heat transfer between the cold parts of the cryostat and the assembly, as well as to avoid condensation inside the chamber. This is achieved by the combined the action of a vacuum pump and cryopumping, requiring the help of active charcoal adsorbers placed at several locations in the cryostat (see Fig. 2.2) and increasing the cold surface available for the adsorption of gas molecules. An optional connection to nitrogen gas is also helpful to reach high vacuum, since nitrogen tends to form bonds with the impurities attached to the sides of the sample chamber, that are thus removed upon flushing the chamber. At the base temperature, the pressure in the vicinity of the sample is around 10^{-10} bar, while it is on the order of 10^{-9} bar outside the radiation shield.

The temperature is monitored with the help of commercial Cernox CX-SD ther-

mometers, from Lakeshore Instruments, at four locations in the cryostat: stage 1, stage 2, sample platform and sample mount, as indicated in Fig. 2.2. This last thermometer is embedded in a metallic cylinder and inserted in a cavity on top of the sample mount, just below the sample holder (see Fig. 2.1 (d)). After cooldown, the final temperatures at stage 1, stage 2, platform and sample thermometers are respectively ~ 30 K, ~ 2.8 K, ~ 3.3 K and ~ 3.5 K. The cooldown procedure typically takes around 3 hours, but if achieving the base temperature is a must, a waiting time of 6 hours should be expected. The temperature of the sample is controlled by adjusting the power dissipated by heaters located at stage 1, stage 2 and sample platform (see Fig. 2.2).

Windows made from UV-grade synthetic fused silica provide optical access to the sample from the top, while minimizing the light intensity losses, namely with an anti-reflective coating that reduces the surface losses for the visible wavelengths. In the "round castle" configuration, in which most of the measurements presented in this thesis were performed, the minimum working distance is 4.2 mm, thus requiring the use of long working distance objectives. This distance can be decreased in the base configuration, even further if the low working distance option is installed (down to 1 mm), but at the cost of a higher base temperature and lower stability. The motion of the sample stage due to the thermal contraction is corrected from room temperature to 4 K, thanks to alternating nested support materials with equally balanced thermal contraction. However, some residual drift on the order of a few tens of micrometers with respect to the microscope might still arise during the measurements and has to be accounted for during data analysis.

2.2.3 Sample mounting

Regarding the cryostat, the most sensitive operation the user has to perform is the installation of the sample in the sample chamber. A schematic view of the sample mounting is represented in Fig. 2.1 (d). It is indeed of paramount importance to have a good thermal link between the sample, the sample holder and the sample mount in order to reach the base temperature of the system. Therefore, these parts are made of oxygen-free high thermal conductivity copper (also called C101 or OFE), which has a thermal conductivity of $630\,\mathrm{Wm^{-1}K^{-1}}$ at 4 K, more than twice the value for standard grade copper (C110)[1]. The thermal link at the sample mount/holder and holder/sample interfaces is ensured by a thin layer of Apiezon N grease[2]. The amount of grease must be carefully adjusted to be as thin as possible, since it has only a thermal conductivity of around $0.1\,\mathrm{Wm^{-1}K^{-1}}$, and it should fill the gaps between the two pieces of material without completely isolating them from one another. For the

[1] By comparison, aluminum or steel have a thermal conductivity lower than $6\,\mathrm{Wm^{-1}K^{-1}}$ at 4 K.
[2] VGE varnish or silver paste might also be used to glue the sample to the holder.

same reason, the sample holder should be firmly tightened to the sample mount using four bolts, as they will increase the pressure at the interface and offer an additional thermal link, as high as $10\,\mathrm{Wm^{-1}K^{-1}}$ per bolt.

Given the limited cooling power of the cryostat, the sample should fit on the 7 mm diameter space available on the sample holder, as in Fig. 2.1 (b-c). This is actually a requirement for electrical measurements, since a PCB chip is then attached on top of the sample holder. The PCB chip has 12 pads wired to electrical connectors outside the cryostat. The pads can be bonded to the sample to perform transport measurements for instance. In section 2.3.5.3, we discuss an example where magneto-optical imaging and transport measurements are performed simultaneously.

2.2.4 Liquid helium cryostat (UFSCar)

Some of the magneto-optical imaging experiments have been carried in the liquid helium cryostat of the Grupo de Supercondutividade e Magnetismo (GSM), at the Federal University of São Carlos (UFSCar). The system is a continuous flow MicrostatHe cryostat, commercialized by Oxford Instruments. The sample is mounted at the extremity of a cold finger, which is then inserted in the sample chamber with optical access. Vacuum is obtained in the chamber using a primary pump in combination with a turbo pump. After a couple of hours of pumping, liquid He stored in a Dewar is inserted through a transfer tube and the temperature quickly drops to the base temperature of the system, around 2.5 K. Note that this is actually lower than the boiling temperature of helium, because of the careful adjustment of the He flow using a needle valve. An Oxford ITC 503S temperature controller adjusts the power in a heater mounted on the cryostat cold finger. More information about this particular setup can be found in Ref. [40]. In addition to its lower base temperature, this system also presents a larger cooling power (around 1 W at 5 K) compared to our closed-cycle cryostat (about 0.1 W at 4 K).

2.3 Magneto-optical imaging

Magneto-optical imaging (MOI) is a microscopy technique relying on linearly polarized light to image the magnetic field of a sample [41, 42]. It is based on the Faraday effect, discovered in 1846 [43], causing a rotation of the plane of polarization of light proportionally to the local magnetic field, in a specially grown indicator placed on top of the sample. MOI is a quite unique technique since it allows for the observation of large areas, up to several $\mathrm{mm^2}$, while being suited for close to real-time imaging. Typical exposure times are smaller than one second, down to 10^{-12} s in optimized fast imaging setups [44]. Compared to other observation techniques, it presents a fair

compromise between spatial resolution, on the order of a few micrometers, and field sensitivity, as low as $10\,\mu$T [45]. It has however been shown that the technique can be optimized to achieve single vortex resolution [46,47]. The best results are obtained with samples having a flat surface, since the gap between the sample and the indicator is minimized in that situation, resulting in a stronger magnetic signal in the indicator.

This section starts with a review of the physical principles underlying the Faraday effect. A description of the indicators designed to optimize the polarization rotation is then presented, followed by a detailed overview and characterization of the MOI setup available at our facilities. We also expose data processing and analysis techniques, with particular focus on how magneto-optical imaging can be turned into a quantitative field-mapping method, as well as how to correct for the artifacts arising in the images. Finally, we apply these techniques on various magnetic samples, such as an array of magnetic bars, a superconducting film topped by magnetic disks and a micrometric planar coil.

2.3.1 Physical principles

Magneto-optical imaging relies on the Faraday effect, consisting in the rotation of the polarization plane of light when it travels in a material where a magnetic field is present. Before delving into the practical implementation of the MOI technique, it is important to understand the underlying physical principles and how polarized light is a useful tool to probe the local magnetic field. The reader will find hereafter a reminder about light polarization, followed by a simplified discussion on the Faraday effect, at the heart of MOI. An excellent review describing the physical principles more formally can be found in Ref. [48].

2.3.1.1 Light polarization

An electromagnetic wave consists in an electric field $\mathbf{E}(\mathbf{r},t)$ and a magnetic field $\mathbf{B}(\mathbf{r},t)$ oscillating in space and time, perpendicular to each other and in phase at all times. These fields define the direction of propagation of the wave, given by the wave vector $\mathbf{k} = \mathbf{E} \times \mathbf{B}$, where $|\mathbf{k}| = k = 2\pi/\lambda$ links the wave number k to the wavelength λ. Therefore, when the direction of propagation of the wave is defined, knowing $\mathbf{E}$ is enough to deduce $\mathbf{B}$. For a given $\mathbf{k}$, there is however a degree of freedom on the direction of $\mathbf{E}$, since it can be oriented anyhow in the plane perpendicular to $\mathbf{k}$. In general, a light beam consists in waves having their electric field $\mathbf{E}$ oscillating in random directions. The light is then said to be unpolarized. In case the oscillation directions of $\mathbf{E}$ are not random, light possesses to some extent a property called polarization. Without loss of generality, let us consider an electromagnetic wave propagating in the positive z-direction ($\mathbf{k} = k\mathbf{e}_z$). At a fixed point $\mathbf{r}_0$ in space, the temporal evolution of

the direction of oscillation of $\mathbf{E}(\mathbf{r}_0, t)$ defines several types of polarization, illustrated for a single wave in Fig. 2.4:

- linear polarization (π): $\mathbf{E}(\mathbf{r}_0, t)$ oscillates along a fixed direction, at a constant angle θ with respect to $\mathbf{e}_x$.
- circular polarization (σ): $\mathbf{E}(\mathbf{r}_0, t)$ rotates and maps out a circle. Depending on the sense of rotation of the tip of the electric field vector as viewed from the observer looking at the oncoming wave, two types of circular polarization can be distinguished: left circular (σ^-, counter-clockwise) or right circular (σ^+, clockwise).
- elliptical polarization: $\mathbf{E}(\mathbf{r}_0, t)$ rotates and maps out an ellipse.

From the point of view of quantum optics, the photon has a spin $S = 1$, and has two eigenstates +1 and -1, corresponding respectively to right circular and left circular polarization. The polarization state of a photon is in general a linear combination of the two eigenstates. In wave optics, the different types of polarization can also be obtained by combining left and right circular polarizations.

In general, the electric field is written as:

$$\mathbf{E}(z, t) = E_0 \mathbf{J} \exp\left(i\left(kz - \omega t\right)\right), \tag{2.1}$$

where ω is the angular frequency, E_0 is the amplitude of the electric field and $\mathbf{J}$, also called the Jones vector, is given by:

$$\mathbf{J} = \cos\theta \exp\left(i\phi_x\right) \mathbf{e}_x + \sin\theta \exp\left(i\phi_y\right) \mathbf{e}_y. \tag{2.2}$$

The observable electric field corresponds to the real part of Eq. (2.1). This way of writing the field is called Jones formalism [49] and is only valid to describe fully polarized light. All other more realistic situations, such as randomly or partially polarized and incoherent light must be treated using Mueller matrices. However, in order to avoid introducing heavy mathematical tools, we will use Jones formalism throughout this discussion, since it leads to the same conclusions provided the light is perfectly polarized. While perfect polarizers do not exist in practice, usual polarizers are close enough for the sake of this discussion, since more than 99.9% of the incident light is indeed polarized.

If $\cos\theta = \sin\theta = \sqrt{2}/2$ and the phase difference $\delta = \phi_x - \phi_y = \pm\pi/2$, the wave is circularly polarized and the Jones vector takes the expression:

$$\mathbf{J}_{\sigma^\pm} = \frac{\sqrt{2}}{2} \exp\left(i\phi_x\right) \left(\mathbf{e}_x \mp i\mathbf{e}_y\right). \tag{2.3}$$

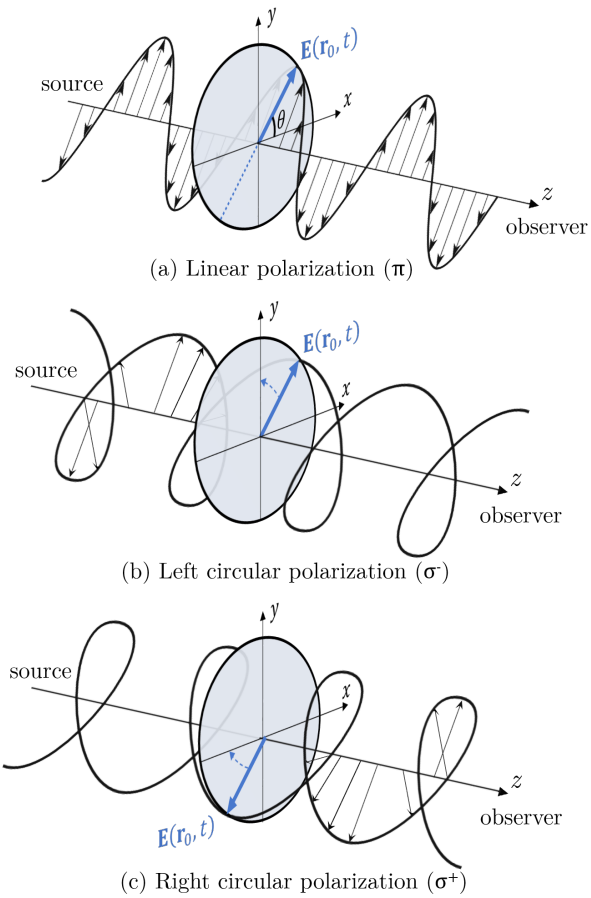

Figure 2.4: **Polarization of an electromagnetic wave.** (a) In a linearly polarized wave, the electric field **E** oscillates in a fixed direction, at an angle θ with respect to the x-axis. (b) When the polarization of the wave is left circular, the tip of the electric field vector maps out a circle at a given point $\mathbf{r}_0$ in space, turning in the counterclockwise sense as seen from an observer looking at the oncoming wave. (c) In case of right circular polarization, the tip of the electric field rotates in the clockwise sense as seen from the observer.

The minus sign in the equation (plus in δ) corresponds to right circular polarization, σ^+, as viewed from the receiver, while the plus sign (minus in δ) correspond to left circular polarization, σ^-.

The Jones vectors for circular polarization can serve as a base for decomposing any kind of polarization. In general, the Jones vector of any wave can be written as a linear combination of $\mathbf{J}_{\sigma^+}$ and $\mathbf{J}_{\sigma^-}$ as follows:

$$\mathbf{J} = \frac{\sqrt{2}}{2}\left(\cos\theta + i\sin\theta\exp\left(i\delta\right)\right)\mathbf{J}_{\sigma^+} + \frac{\sqrt{2}}{2}\left(\cos\theta - i\sin\theta\exp\left(i\delta\right)\right)\mathbf{J}_{\sigma^-}. \tag{2.4}$$

From this equation, is it easy to verify that linear polarization is actually made of the sum of a left and a right polarization. This is verified by writing the Jones vector $\mathbf{J}_\pi$ for $\delta = 0$:

$$\mathbf{J}_\pi = \exp(i\phi_x)(\cos\theta\mathbf{e}_x + \sin\theta\mathbf{e}_y). \tag{2.5}$$

Therefore, a wave linearly polarized at an angle θ with respect to $\mathbf{e}_x$ can always be decomposed in a left circular and a right circular polarization component. This will prove useful to understand the Faraday effect, arising from an asymmetry between the left and right circular components of linearly polarized light.

While this description was based on a single electromagnetic wave, it can be mapped to account for a coherent monochromatic light beam with linear polarization, which would be the ideal light source for the MOI technique. In general however, light might be either unpolarized, for instance in the case of an uncoherent light source, or have partially or totally one of the three types of polarizations presented above. A detailled description of light polarization based on Mueller matrices can be found in Ref. [48].

2.3.1.2 Faraday effect

Light, and electromagnetic waves in general, propagating in a transparent media often undergo a modification of their properties through a variety of phenomena: absorption, refraction, diffusion... For instance, all materials are characterized by a complex refractive index $\tilde{n}(\lambda) = n(\lambda) + i\kappa(\lambda)$, function of the wavelength λ of the incident light. The real part, $n(\lambda)$, is related to the velocity $v(\lambda)$ of light in the material, through $n(\lambda) = c/v(\lambda)$, where c is the velocity of light in vacuum. The imaginary part, $\kappa(\lambda)$, represents the absorption of the medium. In isotropic materials, such as gases or liquids for instance, $\tilde{n}$ is uniquely defined and is independent on the incident direction of light.

However, in anisotropic materials such as crystals, different propagation velocities might be associated to different crystallographic axes, since the atomic spacing and electronic density vary depending on the crystalline structure. This gives rise to different $\tilde{n}(\lambda)$ values depending on the incident light direction, a phenomenon known as birefringence: if a light beam is send at an angle with respect to crystallographic directions with different $\tilde{n}(\lambda)$, it is split when exiting the material. This is a consequence of the fact that the projections of the light beam on each crystallographic axis behave according to different refractive indices.

Birefringence is observed only if the incident light is at an angle with respect to the crystallographic axes. However, a light beam might be affected by some materials, even if it is parallel to one of the crystallographic axes. For instance, some anisotropic crystals or liquids have a property called optical chirality: these media are not sym-

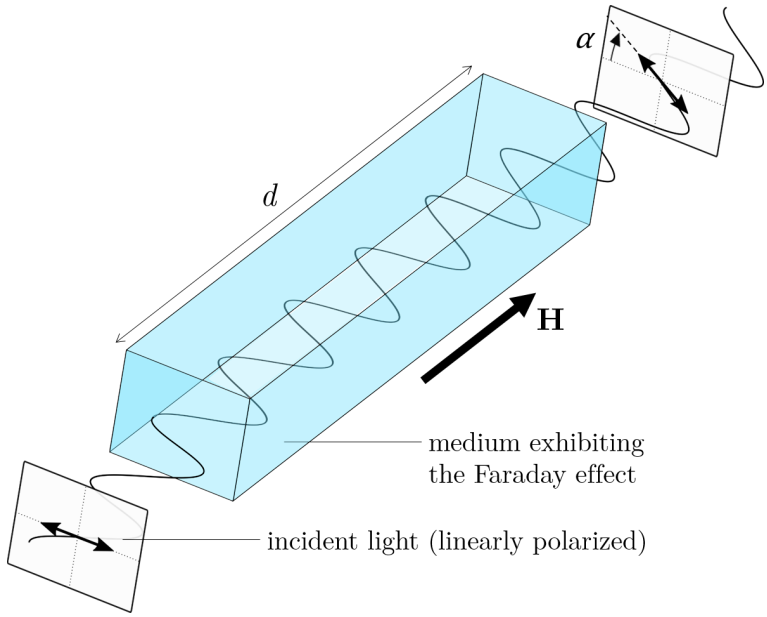

Figure 2.5: **Faraday effect.** Illustration of the Faraday effect, occurring when a linearly polarized electromagnetic wave crosses a transparent dielectric material immersed in a magnetic field H. The right and left circularly polarized components of the wave propagate at different velocities, due to the difference of refractive indices $\Delta n = n_{\sigma^+} - n_{\sigma^-}$, leading to a rotation α of the direction of the linear polarization, proportionally to Δn.

metric with respect to a mirror operation, i.e., their image in a mirror is different from the initial object. Interestingly, this leads to different refractive indices $\tilde{n}_{\sigma^+}$ and $\tilde{n}_{\sigma^-}$ for the left and right circular polarization components of the light beam. When the real part $n_{\sigma^\pm}$ of $\tilde{n}_{\sigma^\pm}$ is affected, meaning that the left and right circular polarization components travel at different velocities, the medium is said to show optical activity, while it presents circular dichroism if κ_{σ^+} and κ_{σ^-} are different. The difference $\Delta n = n_{\sigma^+} - n_{\sigma^-}$ between right and left circular polarization means that a linearly polarized beam propagating in an optically active medium will have its polarization direction rotated, proportionally to Δn. Since this rotation occurs naturally in some materials, it is sometimes also called natural rotation.

Under certain conditions, rotation of the light polarization might also appear in non-chiral materials, namely in the presence of a magnetic field. This effect, called the Faraday effect, is present in all transparent dielectric media when linearly polarized light travels parallel to a magnetic field, but it is generally quite weak. When a magnetic field is applied, the mobility of the bound electrons is affected and symmetry is broken in the material: left and right circularly polarized components of light propagate at slightly different velocities in the medium. In other words, the presence

of the field modifies the dielectric permittivity tensor, closely related to the refractive index, which loses its symmetry with respect to the light polarization. For linearly polarized light, this leads to the rotation of the polarization direction, proportionally to $\Delta n = \tilde{n}_{\sigma^+} - \tilde{n}_{\sigma^-}$, as represented in Fig. 2.5.

For an applied field $H = \mu_0 B$, the rotation angle α of the plane of linear polarization is given by

$$\alpha = V(\lambda) dB, \tag{2.6}$$

where d is the distance traveled by light in the material and $V(\lambda)$ is the Verdet constant, depending on the medium of propagation and the wavelength of the light. Typical values of $V \sim 10^{-5}\,^{\circ}\mu\mathrm{m}^{-1}\mathrm{mT}^{-1}$ are found in liquids and solids [48], but these can be greatly enhanced in magnetic materials, as will be explained in the next section. Since the Faraday effect is at the heart of the MOI technique, it is of paramount importance to design materials where the rotation of the polarization is as large as possible.

As a final remark, there is an important difference between optical activity and the Faraday effect in the situation where light travels back and forth through the material, for instance upon reflection by a mirror. In the case of optical activity, the total rotation of polarization is zero, since the rotation on one way is annihilated by a rotation in opposite direction on the way back, while the rotation is doubled for the Faraday effect. This difference comes from the fact that the situation is symmetric in the first case, while the magnetic field introduces a symmetry breaking in the latter case. A more quantitative approach of the Faraday effect, using Mueller matrices, can be found in Ref. [48].

2.3.2 Indicators for magneto-optical imaging

Since most materials do not provide on their own enough rotation of the light polarization under an applied magnetic field, it is necessary to adjoin them some indicators, materials specially designed to produce an enhanced Faraday effect. In the next section is given a description of the possible configurations in which the indicators can be used and the parts they are composed of. It is followed by a presentation of the main types of indicators and how they affect the resulting images of the magnetic field distribution. After that, the focus is set on the Bi:YIG based indicators on which this work relies, with a characterization of their optical properties and a description of their response in a magnetic field.

2.3.2.1 Types of indicators

In MOI experiments, the sample is normally observed in the reflection regime, meaning that the polarized light source and the image acquisition device are on the same side of the sample. As mentioned previously, specific indicators are required to produce a significant Faraday effect. The indicator is placed in the optical path, on top of the sample surface, and light crosses it twice, before and after reflection. The key part of the magneto-optical indicators is the magneto-optical active layer, responsible for the Faraday effect. Depending on the type of indicator, it is between a few hundreds of nanometers [50] to hundreds of micrometers thick [51]. In most cases, when the active layer is too thin to sustain itself, it is grown on a transparent glass substrate, typically between 0.2 to 0.5 mm thick. Optionally, a thin mirror layer of about $100 - 200$ nm is deposited on top of the active layer, to ensure proper light reflection.

Several indicator configurations are possible. The indicator might be directly deposited on top of the sample, if the sample surface is reflective enough, or otherwise with a thin mirror layer in between. While this configuration gives the best results in terms of spatial resolution, on the order of the wavelength of the light (around 500 nm) [41, 46, 50, 52], it is not the most convenient, due to possible issues related to the indicator deposition, that is irreversible and has to be repeated on every sample. However, these drawbacks can be overcome by placing an indicator on top of the sample, instead of performing a deposition, as shown in Fig. 2.6 (a). A thin mirror layer might also be added for enhanced reflectance. Most of this work is based on this configuration, illustrated in Fig. 2.6 (b), as it has the advantage to eliminate completely all signal coming from the sample topography, and permits the reutilization of the indicator. Unfortunately, this comes at the cost of a degraded spatial resolution, basically due to the gap between the sample surface and the indicator, on the order of a few micrometers, that leads to a decay of the sample's magnetic field inside the indicator.

Historically, the first indicators were paramagnetic glasses, such as cerium metaphosphates or nitrates, developped in the late 1950's [51, 53]. However, the spatial resolution was limited by the thickness of the material, which had to be hundreds of micrometers thick in order to produce sufficient rotation of the polarization. The magnetic field resolution was also quite poor, around 10 mT. Subsequently, thin layers of europium chalcogenides were used to overcome the limitations on the spatial resolution, reaching values on the order of the wavelength λ [50]. Later, the magnetic resolution was improved down to 1 mT, using EuS/EuF_2 [54] and EuSe [52]. One of the advantages of europium-based indicators is that their response to external magnetic fields saturates at high values of H, usually larger than 1 T. This means these materials are particularly well adapted for the study of bulk superconductors and sources

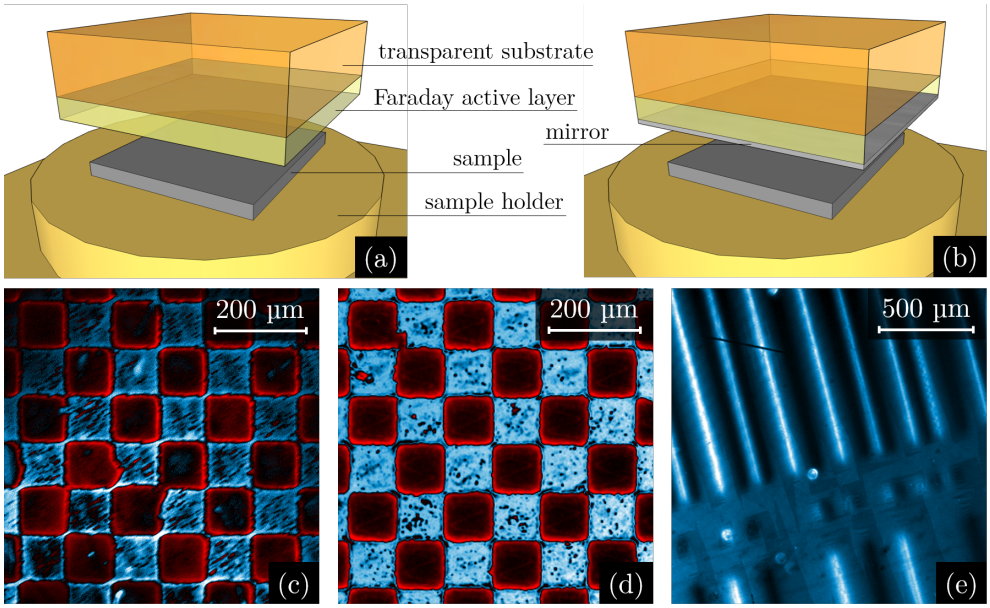

Figure 2.6: **Comparison between different types of indicators used for magneto-optical imaging.** Illustration of the difference in mounting of indicators (a) with mirror and (b) without mirror. (c) Magneto-optical image of a hard ferromagnetic chessboard template (see section 5.3.3.1) with alternating out-of-plane magnetization domains using a EuSe indicator with a thin Al mirror ($T = 4$ K). Dark areas correspond to zero magnetic field, while blue-white (red) represent positive (negative) fields. (d) Same sample observed with a Bi:YIG layer grown on a GGG substrate, with a thin Al mirror. (e) Credit card domains imaged with a Bi:YIG indicator without mirror.

of high fields. However, the drawback of europium-based indicators is that they only operate at low temperatures, below approximately 20 K for EuSe for instance, due to magnetic phase transitions or the decrease of the Verdet constant with increasing temperature [42, 55]. An example of a magneto-optical image using a EuSe indicator at 4 K is shown in Fig. 2.6 (c), where a hard ferromagnetic chessboard template with alternating out-of-plane magnetization is observed[3]. Dark areas correspond to zero magnetic field, while blue-white (red) represent positive (negative) fields.

The drive to study high-T_c superconductors lead to the development of a new type of indicators: impurity doped yttrium iron garnets (YIG, $Y_3Fe_5O_{12}$) [56]. These crystalline magnetic materials are usually grown on a transparent substrate such as gadolinium galium garnet (GGG, $Gd_3Ga_5O_{12}$). Yttrium is substituted with another element, usually with barium or bismuth, to enhance the Faraday effect. The advantage of these indicators is that they can be used at much higher temperatures,

[3]Further information on this sample can be found in section 5.3.3.1.

only limited by the Curie temperature of the material (around 560 K for undoped YIG). The doping has the positive effect of enhancing the Curie temperature and the saturation magnetization, but it also increases the absorption κ, so an optimum for the bismuth concentration x is found for $0.8 < x < 1.1$ [57]. Moreover, the magnetic field resolution is drastically enhanced, up to 10 μT [41]. Originally, garnets called bubble domain films, with spontaneous out-of-plane domains, were used. The spatial resolution is in that case basically limited by the size of the domains and the observation of the magnetic field is indirect, since one is merely monitoring the changes in the domains distribution [56]. These problems were addressed by designing garnets with in-plane anisotropy, where H would tilt out-of-plane the initially in-plane local magnetization [58]. An image of the same sample as in Fig. 2.6 (c), obtained with a Bi:YIG layer grown on a GGG substrate, is shown in Fig. 2.6 (d). This indicator has a thin Al mirror layer, but it is also possible to image samples without mirror, as shown in Fig. 2.6 (e), where the magnetic domains in a credit card are visualized. There materials allow for a direct visualization of the magnetic field distribution, with a spatial resolution of a few micrometers, basically limited by the thickness of the layer and the gap between the sample and the indicator [41]. These indicators are used extensively throughout this work and are characterized in the following section.

2.3.2.2 Optical characterization of Bi:YIG indicators

The MOI experiments in this thesis were performed with Bi:YIG ($Y_{3-x}Bi_xFe_5O_{12}$) garnets provided by the groups of T. H. Johansen (University of Oslo) and P. Vanderbemden (University of Liège). They are grown on an approximately 450 μm thick transparent GGG substrate. A 100 nm thick aluminum mirror has been deposited on the Bi:YIG layer to enhance the reflection of the incident light. The GGG substrate is fairly transparent for visible and infrared light and has a refractive index $n_{GGG} \simeq 2$ in the visible light range [59]. In order to characterize the Bi:YIG layer, we probed the spectral response of an indicator without mirror by performing transmittance and reflectance measurements. The wavelength λ of the incident light is swept from 400 nm to 1200 nm. The detector, measuring light intensity, is positioned at the other side of the indicator (transmittance measurements) or on the same side as the light source (reflectance).

At the interfaces between two different media, the incident beam is split in two parts: a reflected beam and a transmitted beam, as illustrated in Fig. 2.7 (a-b). For the sake of clarity, only the main components relevant for the discussion have been represented. For the transmittance measurements (Fig. 2.7 (a)), the main component of the detected signal comes from the beam transmitted without reflection through all the interfaces. Part of the incident light beam undergoes a double reflection inside

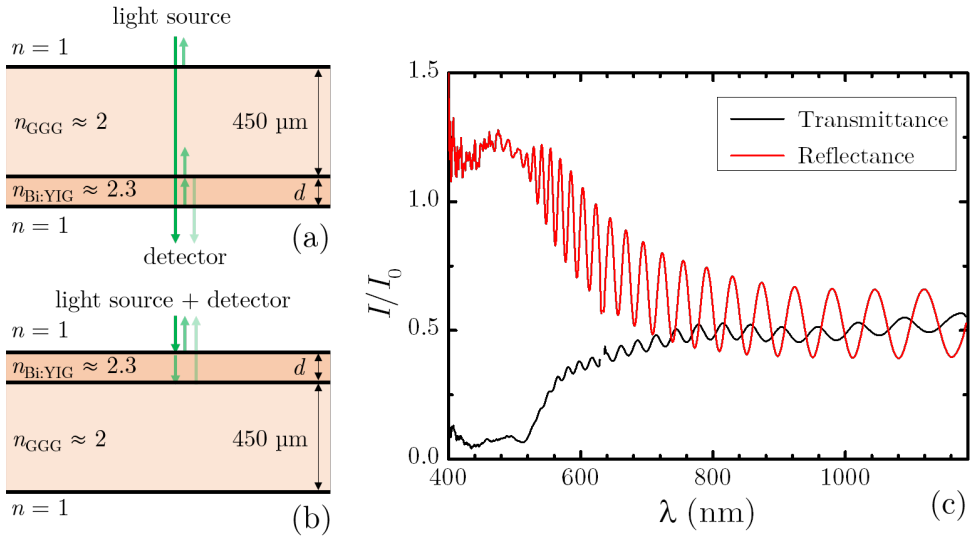

Figure 2.7: **Optical characterization of the Bi:YIG indicator.** Configuration for (a) transmittance and (b) reflectance measurements on the Bi:YIG indicator, grown on a GGG substrate, used throughout this work. For a given wavelength λ of the incident light, two components of the beam interfere constructively or destructively depending on the thickness d of the Bi:YIG layer. (c) Transmittance and reflectance as a function of λ.

the Bi:YIG layer and interferes with the component of the beam transmitted without reflection. Other components of the incident light beam are either reflected towards the light source or have a negligible intensity, since they undergo multiple reflections at the interfaces and are strongly weakened due to absorption in the GGG substrate.

The transmitted light intensity spectrum presented in Fig. 2.7 (c) shows that the indicator is semi-transparent in the near infrared and in the visible region of the spectrum, up to approximately 550 nm. This is consistent with the values found in the literature for similar indicators [60]. For wavelengths where absorption is limited, the spectrum shows an interference pattern characteristic of thin films. Indeed, the phase difference $\Delta\phi$ between the two main interfering beam components is given by

$$\Delta\phi = \frac{2\pi\delta}{\lambda}, \tag{2.7}$$

where λ is the wavelength of light and δ is the difference between the optical distances traveled by the two interfering components. In this situation, δ is expressed as

$$\delta = 2dn_{\text{Bi:YIG}}, \tag{2.8}$$

where $n_{\text{Bi:YIG}}$ is the refractive index of the Bi:YIG layer and d is its thickness. The factor of 2 comes from the fact that the beam component reflected twice at the interfaces crosses the Bi:YIG layer back and forth. In order to have constructive interference, $\Delta\phi$ has to be a multiple of 2π, so any local maximum in the transmittance signal of Fig. 2.7 (c) must satisfy the condition

$$k = \frac{2dn_{\text{Bi:YIG}}}{\lambda}, \tag{2.9}$$

where k is an integer. Two consecutive local maxima in the spectrum, located at λ_1 and λ_2, are therefore related as follows:

$$k_2 - k_1 = 1 = 2dn_{\text{Bi:YIG}} \left(\frac{1}{\lambda_2} - \frac{1}{\lambda_1} \right). \tag{2.10}$$

In the infrared end of the spectrum, the total light intensity in Fig. 2.7 (c) is made of oscillations with an amplitude t_0 superposed to a constant signal T_0, and can be described by

$$T_0 + t_0 \cos \Delta\phi = T_0 + t_0 \cos \left(\frac{4\pi dn_{\text{Bi:YIG}}}{\lambda} \right). \tag{2.11}$$

As can be seen from this expression, the variables d and $n_{\text{Bi:YIG}}$ are associated and can thus not be uniquely determined from this single equation. Since the refractive index of Bi:YIG in the near infrared is know to depend on λ and on the Bi concentration x as [61]

$$n_{\text{Bi:YIG}}(\lambda, x) = 2.174 + \frac{0.0593}{\lambda^2} + \left(0.103 + \frac{0.0371}{\lambda^2} \right) x, \tag{2.12}$$

and assuming $x = 1$, we can fit the infrared part of the spectrum with Eq. (2.11). We find $n_{\text{Bi:YIG}} \simeq 2.3$ for $\lambda = 1\,\mu\text{m}$ and $d = 3.5 \pm 0.5\,\mu\text{m}$.

The same procedure applied to the reflectance spectrum shown in Fig. 2.7 (c) confirms the values calculated previously. In this configuration, the indicator is flipped with the Bi:YIG layer on top, as illustrated in Fig. 2.7 (b). The fact that the signal I/I_0 surpasses 1 in the small wavelengths end of the spectrum probably comes from the imprecision in the incident light intensity calibration (I_0), but it does in any case not play a role in our calculations. The oscillations in the reflectance as a function of λ have a larger amplitude t_0, since light does not cross the GGG substrate in this configuration, thus limiting the absorption. Moreover, there is a phase shift of π with respect to the transmittance spectrum. Indeed, the phase of the light component reflected at the Bi:YIG/GGG interface is left unchanged, as $n_{\text{GGG}} < n_{\text{Bi:YIG}}$, in contrast to the component reflected at the air/Bi:YIG interface, whose phase is shifted by π since $n_{\text{Bi:YIG}} > n_{\text{air}}$.

2.3.2.3 Magnetization in Bi:YIG indicators

The Bi:YIG based indicators that were used in this thesis have a strong in-plane anisotropy, leading to a magnetization M naturally lying in the film plane. Therefore, if a linearly polarized light beam propagates in the layer along the out-of-plane direction, its polarization is left unchanged. However, when a magnetic field H is applied perpendicularly to the layer, the magnetization is tilted by an angle Φ and rotation of the plane of polarization by an angle α occurs, proportionally to the out-of-plane magnetization component M_z:

$$M_z = M_\mathrm{s} \sin \Phi, \tag{2.13}$$

where M_s is the in-plane saturation magnetization. This situation is illustrated in Fig. 2.8 (a), and assumes that there is no hysteresis or residual M_z at $H = 0$. Under these conditions, $\Phi = \arctan(H/H_\mathrm{a})$ and α is given by [42]

$$\alpha = CM_z = CM_\mathrm{s} \sin\left(\arctan\left(\frac{H}{H_\mathrm{a}}\right)\right). \tag{2.14}$$

H_a is called the anisotropy field and corresponds to the applied field at which $M_z = M_\mathrm{s}/2$. A larger value of H_a means that higher fields H can be applied before saturating the indicator response. Typical values for Bi:YIG indicators similar to those used in this thesis are $\mu_0 H_\mathrm{a} \sim 100$ mT [41, 62].

The response of our Bi:YIG indicator at 10 K is represented in Fig. 2.8 (b), for the typical range of fields H we apply during MOI measurements. In practice, the Faraday rotation α caused by H is compensated by changing the angle β between the analyzer and the polarizer, until the detected light intensity is minimized. The slope gives the value of $2Vd = 0.13 \pm 0.02° \mathrm{mT}^{-1}$ for the indicator. Since the Bi:YIG layer has a thickness $d \simeq 3.5\,\mu$m, the Verdet constant of the indicator is $V = 0.018 \pm 0.005° \mu\mathrm{m}^{-1}\mathrm{mT}^{-1}$ at 10 K. This value at low fields is comparable to those obtained by other groups for similar indicators [42].

Even if the magnetization lies in-plane, due to the strong anisotropy, it is often not forming a single domain but is rather broken down in several domains with in-plane magnetization pointing in different directions. These domains form typical triangular shaped structures, clearly visible in the image of Fig. 2.8 (c). The Bloch domain walls between in-plane domains with opposed magnetization are visible thanks to the polar Faraday effect described previously. However, it cannot account for the contrast between domains, since the out-of-plane component of the magnetic field is negligible. The light intensity of domains with different in-plane orientation varies with the polarization direction of the incident light beam. There are two manners to evidence this effect: (i) change the direction of polarization of the incident light beam or (ii)

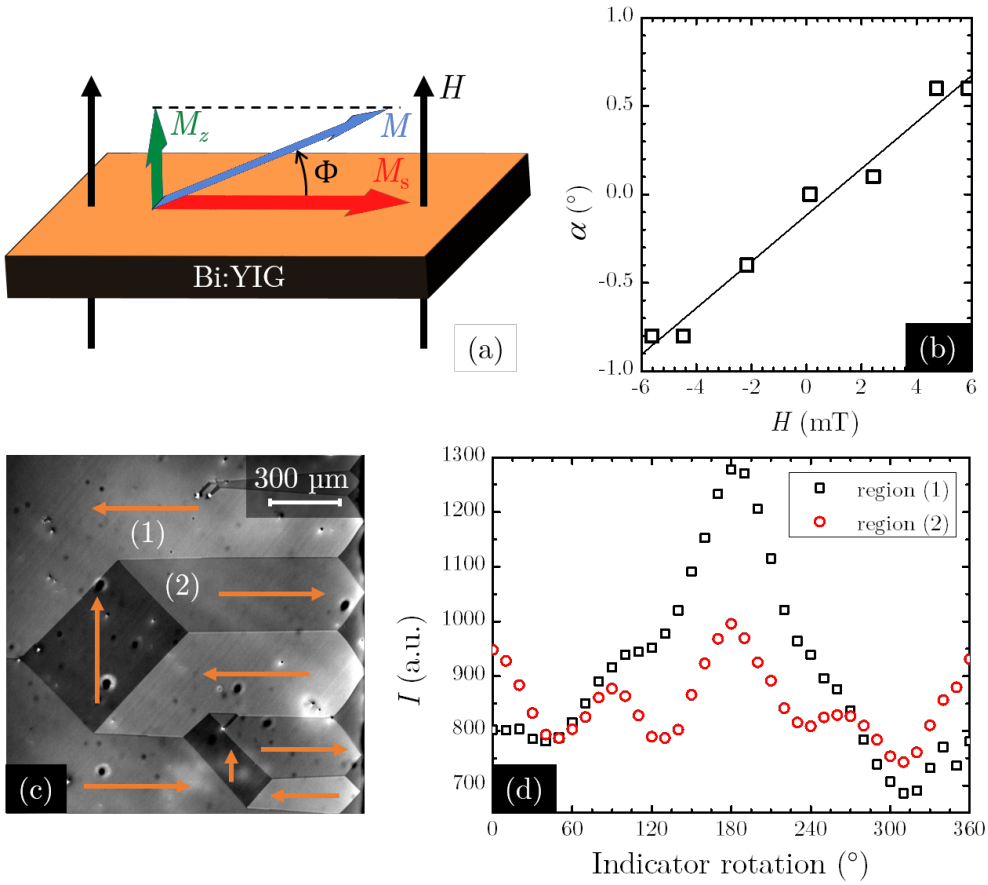

Figure 2.8: **Magnetization of the Bi:YIG indicator.** (a) The magnetization M of the Bi:YIG layer of the indicator naturally lies in-plane and has a saturation value of M_s. It is tilted out-of-plane by an angle Φ when a field H is applied, causing a Faraday rotation α proportional to M_z, the out-of-plane component of M. (b) α in our Bi:YIG based indicator as a function of H at 10 K. The line represents the linear fitting to determine V. (c) Magneto-optical image of the indicator, showing domains with different in-plane magnetization directions (represented by the orange arrows). The intensity as a function of the indicator in-plane rotation angle is represented in panel (d) for two regions of interest, in two neighboring domains of panel (c).

rotate the indicator around a vertical axis. Since the polarizer in our system cannot be rotated, the indicator is placed on a rotating platform and magneto-optical images of the magnetic domains are recorded every 10°. The results are shown in Fig. 2.8 (d). The graph represents the intensity I as a function of the angle of the rotating platform for two regions of interest, located in different domains identified in Fig. 2.8 (c). The curves present oscillations with a 90° period, attributed to the quadratic Voigt effect, while the larger modulation with a period of 360° is related to the longitudinal

Faraday effect [63]. The Voigt effect is caused by linear magnetic birefrigence and takes place even for a light beam at normal incidence. The longitudinal Faraday effect occurs when the incident light is not perfectly perpendicular to the indicator surface. Since the light has a small in-plane component, some unwanted rotation of polarization occurs depending on the direction of M. This comes mainly from the illumination path of the microscope, but can also arise from the difficulty to mount the indicator perfectly horizontally.

In MOI experiments in general, domains are quite difficult to avoid, since they tend to move when the applied field is changed. They especially tend to concentrate in the regions where the field gradient is the strongest. As long as the region of interest stays in the same domain during the whole experiment, images are easy to interpret, but when domains move across the image, one has to be careful not to misinterpret the associated jump in intensity. The unwanted contrast caused by indicator domains will be dealt with in a subsequent part of this chapter.

2.3.3 Magneto-optical imaging setup

Now that the physical principles behind the magneto-optical imaging technique have been established, the practical implementation of the technique is described, along with the different parts of the experimental setup present at our facilities in the group of Experimental Physics of Nanostructured Materials (University of Liège). A similar setup is found in the group of Prof. W. Ortiz at the Federal University of São Carlos, where some of the experiments were performed. Our system is then characterized and compared to equipment used in other laboratories.

An overview of the magneto-optical imaging setup is represented in Fig. 2.9. The magneto-optical indicator responsible for the Faraday rotation is placed on top of the sample under study, with the mirror-covered face downwards. Light produced by a Hg lamp goes through a filter selecting green light, then crosses a linear polarizer, before being directed through the objective by a beam splitter. Linearly polarized light crosses the GGG substrate of the indicator and the Bi:YIG layer, where its polarization direction is rotated proportionally to the local magnetic field. It is then reflected by the mirror and crosses again the indicator and the objective. It then passes through an analyzer, whose polarization direction is oriented close to 90° with respect to the polarizer. The analyzer absorbs the light component with polarization in the original direction, so only the light whose polarization has been rotated in the indicator will pass. Light finally enters a CCD-camera, recording 2048×2048 px^2 images representing a field of view[4] of approximately 3×3 mm^2, where dark areas correspond to low magnetic fields and bright regions represent high fields. Magnetic

[4]This value is for the 5× objective we normally use.

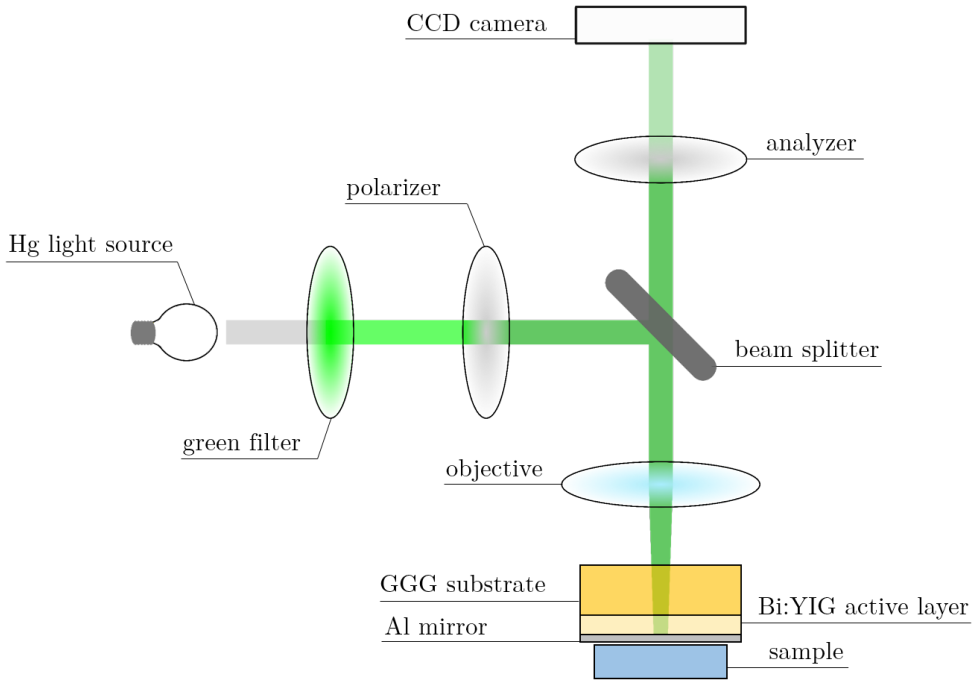

Figure 2.9: **Schematic setup for magneto-optical imaging.** White light produced by the emission of a Hg arc-lamp is wavelength-selected by a green filter and then linearly polarized. The green polarized light is deflected towards the indicator, placed on top of the sample, by a beam splitter. It crosses the GGG substrate and arrives in the Bi:YIG layer where the Faraday effect occurs. If there is a magnetic field, the light has its plane of polarization rotated, while it is unchanged in the absence of field. Light is reflected by the mirror of the indicator and crosses the objective and beam splitter. An analyzer blocks the light whose polarization is unchanged with respect to the polarizer, while it lets through the component that was rotated by the Faraday effect. Images are recorded by a CCD camera, where dark regions correspond to low fields and brights areas represent higher fields.

fields in the range ± 12.5 mT are applied by feeding a cylindrical copper coil with a dc current. The whole microscope and the cryostat, where the sample is installed, are mounted on an actively damped non-magnetic optical table.

2.3.3.1 Microscope unit

In our setup, unpolarized white light is produced in a 100 W arc burner lamp (USH 103 D), through the ionization of high pressure mercury gas by electric discharges. The emission spectrum of the lamp is represented in Fig. 2.10 (a) and is characterized by intense peaks in the UV/violet and in the green/yellow wavelengths range. Of particular interest for MOI is the peak at $\lambda = 550$ nm (green), selected by a green filter (U-25IF550), since the maximum Faraday rotation occurs in this spectral region [64].

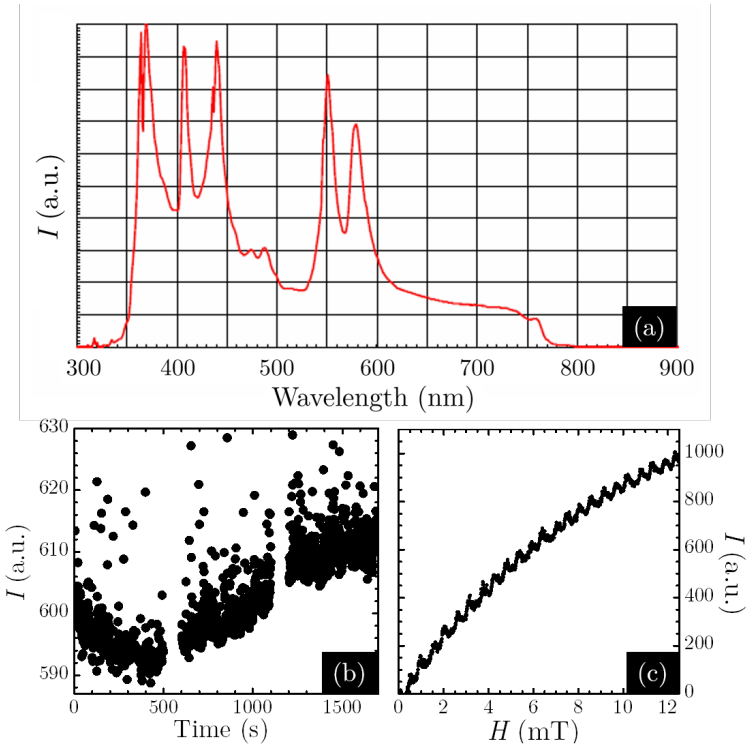

Figure 2.10: **Characteristics of the light source.** (a) Spectrum of the light emitted by the Hg lamp. The peak at 550 nm is selected by a green filter for magneto-optical imaging. Spectrum reproduced with the courtesy of Olympus. (b) Fluctuations of the light intensity as a function of time. Data points corresponds to the intensity averaged over one image. (c) Oscillations of the light intensity over a long period. Each point is the average intensity computed over 100 images. The period of the oscillations is approximately 48 minutes.

The nearly-monochromatic unpolarized green light then passes through a linear polarizer (U-PO3) with a fixed horizontal polarization direction. If the unpolarized incident beam has an intensity I_0, the intensity I of the linearly polarized light coming out of a perfect linear polarizer is given by

$$I = \int_{-\pi/2}^{\pi/2} I_0 \cos^2\theta \mathrm{d}\theta = \frac{I_0}{2}. \tag{2.15}$$

In practice however, as will be discussed later in the system characterization section 2.3.3.3, real polarizers always let some non-linearly polarized component through [48]. The power of the Hg light source integrated over the wavelength range between 200 nm and 1100 nm is 5.9 ± 0.3 mW, as measured by a Si photodiode on a light spot of 8 mm in diameter. After filtering and polarizing, this value drops to 0.54 ± 0.03 mW.

We analyzed the stability of the Hg light source during prolonged experiments by recording the intensity averaged over a whole image at different times. The resulting curve is shown in Fig. 2.10 (b). The data shows clearly that, in addition to the noise with standard deviation $\sigma \simeq 5$, the intensity produced by the light presents a longer period variation. This is even better illustrated in Fig. 2.10 (c), where the intensity, averaged over 100 images, is recorded over 20 hours as the magnetic field H is increased. From fitting the curve, we find a period of approximately 48 minutes for the oscillations. Moreover, while the value of σ gives an idea of the average noise, it is important to notice that a significant number of points are more than 5σ apart from the average intensity, making it important to account for the fluctuations of the incident light intensity when interpreting the MOI data. For this reason, a method correcting for these fluctuations is necessary in order to make quantitative statements on the intensity images. This will be presented in section 2.3.4.3.

The core of the microscope is the modular Olympus BX-RLA2 illuminator, containing all the optics, including the polarizer and the filter described previously. The light source is protected by a dedicated housing attached at the back of the illuminator. The system is mounted on a custom made pillar inserted in a heavy base plate. This configuration allows for two degrees of freedom, rotation around the pillar and height adjustment, preserving at all times the perpendicularity between the sample surface and the optical axis of the microscope. The microscope allows for both brightfield (BF) and darkfield (DF) microscopy. Magneto-optical imaging relies exclusively on BF observation, but DF microscopy is an interesting tool to highlight the topography and the defects of a sample surface, since it forms images by collecting the scattered light and excluding the reflected beam.

After crossing the polarizer, the light beam is directed via a beam splitter through the objective and towards the sample. We have three interchangeable strain-free objectives (5×, 20× and 50× magnetization) with a long working distance, WD, corresponding to the distance between the objective and the plane of focus (the sample or indicator mirror surface). Strain-free objectives are designed to minimize the depolarization of the light beam, arising namely from strain in the lenses, where the lens is connected to its frame for instance. As a reminder, the magnification of an objective is roughly the ratio between the size the object under observation is perceived and its actual size. More formally, it is defined as the ratio between the tube length d and the focal length f_0. The distance d corresponds to the separation between the objective rear focal plane and the eyepiece front focal plane.

Another important parameter characterizing the objectives is the numerical aperture NA, given by

$$\mathrm{NA} = n \sin \gamma, \tag{2.16}$$

where n is the refractive index of the medium where light is propagating ($n = 1$ here), and 2γ is the largest angle of the cone of light that can enter and exit the objective. The 5× objective (LMPLFLN 5×BD) has NA= 0.13, WD= 15 mm and $f_0 = 36$ mm. The 20× objective (LMPLFLN 20×BD) has NA= 0.40, WD= 12 mm and $f_0 = 9$ mm. The 50× objective (LMPLFLN 50×BD) has NA= 0.50, WD= 10.6 mm and $f_0 = 3.6$ mm.

For MOI, we relied mostly on the objective with 5× magnification, since the 20× and 50× objectives do not provide an enhanced spatial resolution in our system. This is due to increased reflection and depolarization effects in the windows of the cryostat upon changing to objectives with larger magnification. Indeed, these have a larger NA, thus the incidence angle of light γ is also larger, leading to an increase of the optical path through the windows and of the reflectivity at the interfaces. These effects degrade the contrast and annihilate the gain in spatial resolution coming from the magnification increase. For regular images of the sample surface however, 20× and 50× objectives still provide better spatial resolution if the sample is observed outside the cryostat, thus without windows in the optical path.

After being reflected back to the objective, light crosses an analyzer (AN-360), whose direction of polarization is tunable with a precision of 0.1°. According to Malus law, the intensity I of the light crossing the analyzer is given by:

$$I = I_0 \cos^2 \beta, \tag{2.17}$$

where I_0 is the intensity of the incident linearly polarized light and β is the angle between the analyzer and the polarizer directions. Let us consider the situation where the analyzer is oriented at $\beta = 90°$ with respect to the polarizer, corresponding to the so-called extinction (or crossed-Nichols) configuration. In the absence of magnetic field in the indicator, all the light is blocked and the output intensity is zero. However, if the plane of linear polarization is rotated, due to the Faraday effect for instance, non-zero intensity proportional to the magnetic field comes out of the analyzer. This allows to form images where the intensity is proportional to the magnetic field, i.e., dark regions correspond to small magnetic fields, while bright areas correspond to larger fields. However, it is not possible to distinguish between positive and negative fields in the extinction configuration: $+H$ and $-H$ fields induce $+\alpha$ or $-\alpha$ rotation of the polarization, which lead to the same intensity I according to Eq. (2.17). For this reason, it is advantageous to chose the angle between analyzer and polarizer such as to have a mismatch β of a few degrees from the extinction configuration. Indeed, $+H$ and $-H$ fields then correspond to different intensities $I_0 \cos^2(\beta \pm \alpha)$, so positive and negative fields can be distinguished. In this situation, $H = 0$ does no longer correspond to $I = 0$, but to some finite intensity I_β. Negative and positive fields will appear darker or brighter than I_β, depending on the sign of β.

Images are recorded with a CCD camera RETIGA-4000R mounted on top of the microscope unit. The captor has 4.2 megapixels and each pixel is 7.4 μm $\times$7.4 μm large. The camera captures light intensity on a 12-bit grayscale, and thus records 2048×2048 px^2 images where the intensity values range from 0 to 4095. With the 5$\times$ objective, the field of view in the images recorded by the camera is 3×3 mm^2, which means that each pixel in the images corresponds to an area of $1.468 \times 1.468\,\mu$m^2. For MOI, the exposure, representing the time the captor is exposed to light, is typically between 100 ms and 1 s. This interval is usually much shorter for regular optical images, depending on the reflectivity of the sample surface.

An optional magnification of 2$\times$ can be obtained by inserting a 2-position magnification changer (U-ECA) in the optical path of the reflected beam. Finally, the light beam can be narrowed at two points along the optical path. The aperture stop (AS) act on the size of the aperture at the light source. It has the advantage of reducing the angle of the incident light cone, but at the expense of the light intensity. The field stop (FS) narrows the light beam after reflection by the sample. While it reduces the field of view, it might be useful to screen some bright saturated spots ruining the contrast.

2.3.3.2 Magnetic field source

Depending on the configuration of the cryostat ("round castle" or base configuration), an adapted copper wire coil is installed to apply a magnetic field to the sample. In the "round castle" configuration where most experiments were carried, the sample is located at the center of a large coil placed on a custom support platform, as shown in Fig. 2.11 (a). The coil is 6 cm high and has inner and outer diameters of respectively 5 cm and 24 cm. It consists in 3000 turns of AWG 24 copper wire (diameter of 0.511 mm) and has a resistance $R = 22.9\,\Omega$ and an inductance $L = 822$ mH at 1 kHz. The magnetic field is produced by feeding the coil with a dc current source (Keithley 2440). Calibration was done with a USB Hall probe and consists in measuring the magnetic field as a function of the current at the center of the coil, at the location of the sample. The range of magnetic fields produced by the coil is $\pm$30 mT, corresponding to currents of approximately $\pm$1 A, although the wire can in principle sustain up to 3 A. This coil guarantees a good field homogeneity, with spatial variations of at most 1% of the maximum field at the sample location (in a 5×5 mm^2 area).

In the base configuration of the cryostat however, a smaller coil has to be installed, since there is little space available and the weight load on top of the cryostat assembly should be limited. This configuration is illustrated in Fig. 2.11 (b). The coil is made of AWG 28 copper wire (diameter of 0.321 mm), it is 2.5 cm high and has inner and outer diameters of respectively 3.5 cm and 5 cm. It has a total resistance $R \simeq 22.1\,\Omega$

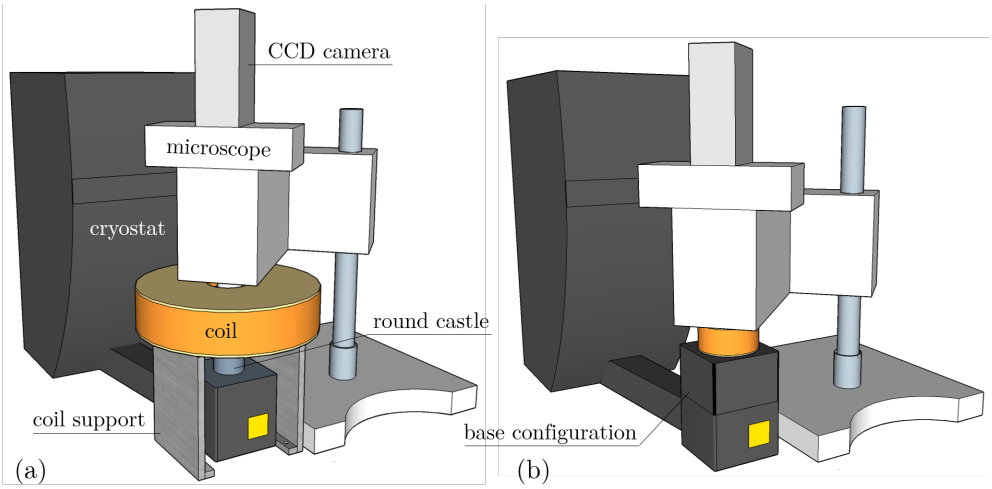

Figure 2.11: **Schematics of the experimental setup for magneto-optical imaging at low temperature.** (a) Magneto-optical setup with the copper coil installed around the sample chamber in the round castle configuration. (b) Magneto-optical setup in the base configuration, where a smaller copper coil is placed on top of the assembly.

and an inductance $L = 27$ mH at 1 kHz. It is placed on top of the cryostat assembly, so the sample is located on the axis of the coil, but at approximately 1 cm from the bottom surface of the coil. Since the sample is further away from the coil and the wire can only sustain 1 A, the field range is limited to ± 10 mT. Moreover, the field at the sample is slightly less homogeneous than for the large coil, with variations of at most a few percents of the maximum field.

2.3.3.3 System characterization

The goal of this section is to characterize the quality of our magneto-optical system from the point of view of optics and compare it with similar setups in other groups [46, 65]. A rigorous way to achieve this is to determine the value of the extinction ratio E_{setup} of our experimental setup, following a procedure described in Ref. [65]. In general, the intensity I measured at the CCD camera is given by the Malus law

$$I(H, \beta_\perp) = P_0 t \left(\sin^2\left(\beta_\perp - \alpha(H)\right) + E_{\text{setup}}\right), \tag{2.18}$$

where H is the applied field and $\beta_\perp$ is the angle between the analyzer and the polarizer, measured from the extinction configuration ($\beta_\perp = \beta - 90° = 0$). P_0 is the power of the light coming out of the polarizer, t is the exposure and $\alpha(H) = 2VdH$ is the Faraday rotation angle, where V is the Verdet constant and d is the thickness of the Bi:YIG

layer in the indicator. As expected from this equation, I increases linearly with the exposure as long as the intensity stays below its saturation value of 4095, a fact that is confirmed experimentally.

In the absence of field H, if $\beta_\perp = 0$, Eq. (2.18) reduces to $I = P_0 t E_{\text{setup}}$. From this expression, the extinction ratio E_{setup} is given by the ratio between the detected intensity I and the light intensity $P_0 t$:

$$E_{\text{setup}} = \frac{I}{P_0 t}. \tag{2.19}$$

In a perfect optical system, $I = 0$ when $\beta_\perp = 0$ and $\alpha = 0$, thus $E_{\text{setup}} = 0$. However, in a real optical system, $I > 0$, mainly because (i) the polarizer lets some non-linearly polarized light through, (ii) depolarization occurs along the optical path, namely in the microscope lenses, the cryostat windows and the indicator, and (iii) light coming from the environment and thermal noise in the CCD camera artificially increase I. Therefore, E_{setup} is non-zero and is the sum of several contributions:

$$E_{\text{setup}} = E_{\text{microscope}} + E_{\text{indicator}} + E_{\text{windows}}, \tag{2.20}$$

where $E_{\text{microscope}}$ accounts for the reflection on the indicator mirror, the microscope optics, the polarizer, the environment and the CCD camera.

In order to characterize our system in the conditions of the MOI experiments, we place the garnet inside the cryostat, GGG substrate facing up, and we measure $I(H)$ for several angles $\beta_\perp$ by sweeping $\mu_0 H$ between -12.5 mT and 12.5 mT in steps of 0.5 mT. The result is plotted in Fig. 2.12 (a). In all the graphs presented in this section, the exposure is $t = 0.5$ s and each data point represents the intensity averaged over 10 images, i.e., over $10 \times 2048 \times 2048 \simeq 42 \times 10^6$ pixels.

By fitting the set of curves with Eq. (2.18), we find[5] that $I_0 = P_0 t = (1.32 \pm 0.15) \times 10^5$, $2Vd = (2.1 \pm 0.2) \times 10^{-3}\,\text{rad.mT}^{-1}$ and $E_{\text{setup}} = (2.5 \pm 0.5) \times 10^{-3}$. From this, notice that the detected intensity is rather small compared to the incident beam intensity, since the ratio I/I_0 is typically on the order of 0.02. The value of $2Vd$ is consistent with results obtained for similar indicators by other groups, finding $2Vd = 2.3 \times 10^{-3}\,\text{rad.mT}^{-1}$ [65]. Since $d \simeq 3.5\,\mu\text{m}$ for our indicator (see section 2.3.2.2), we estimate $V = 0.017 \pm 0.002^\circ\,\mu\text{m}^{-1}\text{mT}^{-1}$, in fair agreement with the values determined in section 2.3.2.3. The extinction ratio E_{setup} is fair compared to other similar experimental setups, where values of 3.8×10^{-3} [65] and 2.25×10^{-4} [46] have been reported.

[5] The intensity I_0 is adimensional, since it corresponds to the grayscale value detected by the CCD camera. However, if needed, calibration can be performed by placing the camera directly in front of the light source. The intensity values can subsequently by mapped to the power provided by a powermeter placed in the same configuration.

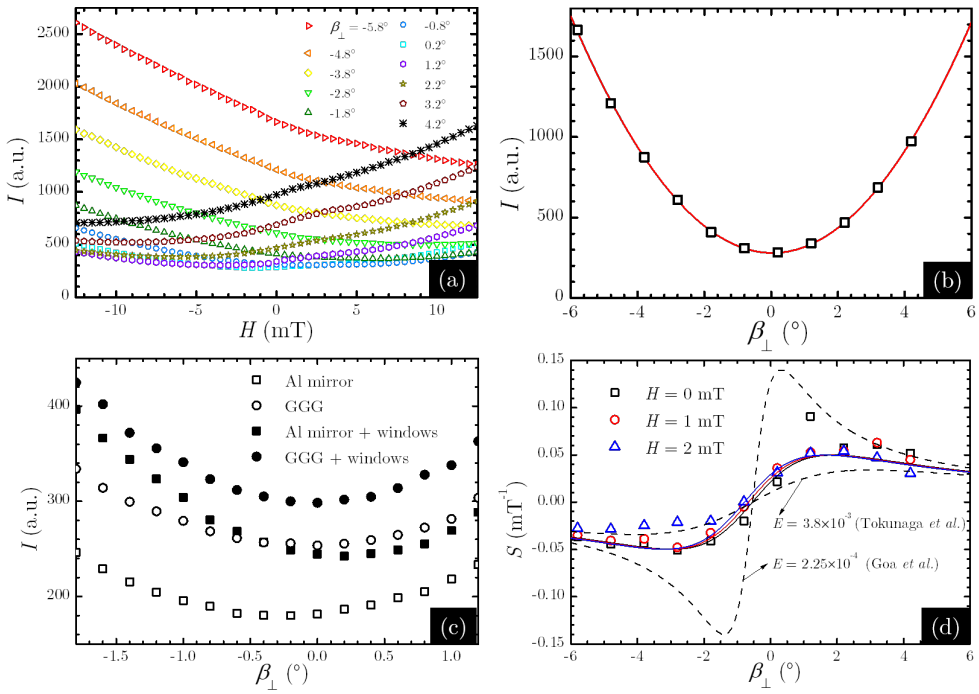

Figure 2.12: **Optical characterization of the magneto-optical setup.** (a) Intensity I as a function of the applied field H for different angles $\beta_\perp$ between analyzer and polarizer (measured from the extinction configuration). (b) I as a function of $\beta_\perp$ for $H = 0$, based on the data of panel (a). (c) Influence of the cryostat windows and the indicator on I. (d) Sensitivity $S(\beta_\perp)$ for various H, compared to setups with different extinction coefficients [46, 65].

When $H = 0$, there is no Faraday rotation of the polarized light and the only parameter influencing I is $\beta_\perp$. Figure 2.12 (b) represents $I(\beta_\perp)$ for $H = 0$ (data points) and the associated fitting (plain line) using Eq. (2.18), confirming the values of the parameters found via Fig. 2.12 (a).

It is possible to estimate the contributions of different parts of the setup to E_{setup} in Eq. (2.20), by comparing $I(\beta_\perp)$ curves when changing the configuration of the system. This is illustrated in Fig. 2.12 (c), where the influence of the cryostat windows and the indicator are evaluated. By assuming that the incident light intensity $I_0 = P_0 t$ is constant throughout the measurements, any variation in the minimum intensity $I = I_0 E$ of the curves must be caused by E. For instance, the influence of the cryostat windows is evaluated by plotting two $I(\beta_\perp)$ curves, one with the windows, the other without. By comparing the ratio of the minimum I in the absence and presence of windows, we find that $E_{\text{setup}} - E_{\text{windows}} \sim 255/300 E_{\text{setup}}$, i.e., $E_{\text{windows}} = (0.15 \pm 0.05) E_{\text{setup}}$. The impact of the indicator, in particular the GGG substrate and the Bi:YIG layer, is estimated by flipping it to have the Al mirror facing up.

If we assume that the mirror has the same properties on both sides, the difference between the two $I(\beta_\perp)$ curves for the indicator substrate up or mirror up comes from the indicator's contribution to E_{setup}. Comparing the minimum I for both curves, we find $E_{\text{setup}} - E_{\text{indicator}} \sim 240/300 E_{\text{setup}}$, so $E_{\text{indicator}} = (0.2 \pm 0.05) E_{\text{setup}}$. Finally, the curve with the indicator mirror up in the absence of windows gives $E_{\text{setup}} - E_{\text{microscope}} \sim 185/300 E_{\text{setup}}$, so $E_{\text{microscope}} = (0.6 \pm 0.1) E_{\text{setup}}$. The main contribution to the depolarization of the light beam is therefore coming from the first term in the sum of Eq. (2.20).

Another parameter of interest is the sensitivity S of the setup, defined as

$$S = \left| \frac{1}{I} \frac{\mathrm{d}I}{\mathrm{d}H} \right| = \left| \frac{-4Vd\,(\beta_\perp - \alpha)}{(\beta_\perp - \alpha)^2 + E} \right|. \tag{2.21}$$

Based on the data presented in Fig. 2.12 (a), $S(\beta_\perp)$ curves are computed for several values of H and are shown in Fig. 2.12 (d). This information is particularly important, since it indicates how the angle $\beta_\perp$ should be chosen to perform the measurements, in order to get the best sensitivity. Fitting of the set of data with Eq. (2.21) gives $S_{\max} = (5 \pm 2) \times 10^{-2}$ mT^{-1} for $\beta_\perp = 2.4 \pm 0.5°$. This value is reasonable when compared to other setups, where $S_{\max} \simeq 3.7 \times 10^{-2}$ mT^{-1} for $\beta_\perp \simeq 3.2°$ [65] and $S_{\max} \simeq 15 \times 10^{-2}$ mT^{-1} for $\beta_\perp \simeq 0.9°$ [46] for instance. Moreover, the fitting also returns $E_{\text{setup}} = (1.8 \pm 0.5) \times 10^{-3}$, close to the value found using Eq. (2.18). The fitting clearly shows that S is relatively independent of H at low fields.

2.3.4 Data acquisition and processing

In this section, the standard procedure for data acquisition is reviewed. It relies on a Labview interface controlling the cryostat, the camera and the current source feeding the coil. Basic image acquisition and analysis is illustrated with a practical example of simple post-imaging data processing leading to clear image enhancement. The usual software tools, namely the ImageJ software, are also presented. While working on the acquired images is important to take the most out of the measurements, it is often better to improve directly the raw images by working on the experimental setup. To that extent, the importance of reducing the distance between the indicator and the sample to obtain better contrast and resolution is demonstrated by introducing a modification in the experimental setup, a clip pressing the indicator against the sample. The natural subsequent step in the analysis process is to convert intensity images to magnetic field. While this is not in general an easy task, a technique is presented to achieve this conversion, provided a preliminary calibration is performed. Interestingly, it also allows to isolate the magnetic field contribution of a superconductor from a constant source of magnetic field, such as a ferromagnetic material for instance. Finally,

a method is proposed to correct images where the indicator magnetic domains spoil the contrast, permitting to unveil information that was hidden by the artifacts.

2.3.4.1 Basic image acquisition and analysis

Basic analysis and data processing on the recorded set of images is usually performed using the open-source ImageJ software [66]. The core version of the software has namely the advantage to be customizable with plugins maintained by the large user community. Along with basic features such as contrast and luminosity adjustment, filtering and mathematical operations on images, the software has some more advanced tools applicable to sequences of images, such as automatic correction for misalignment or contrast differences.

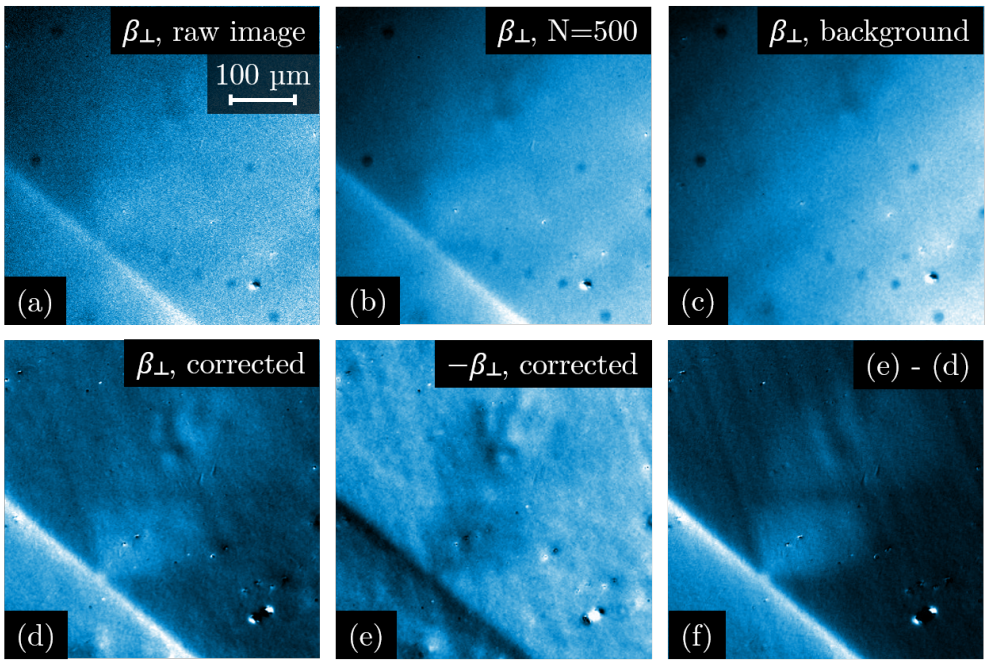

Figure 2.13: **Improvement of the signal-to-noise ratio in magneto-optical images.** Illustration of the different steps that can be undertaken to enhance the images, applied to the edge of a superconducting Nb film. (a) Raw image at a given analyzer angle $\beta_\perp = 1.8°$. (b) Average of $N = 500$ images at $\beta_\perp = 1.8°$. (d) Difference between the image (b) and the average of 500 images at $H = 0$, represented in panel (c). (e) Image resulting from the same procedure applied to obtain panel (d), but for $\beta_\perp = -1.8°$. (f) Difference between image (d) and image (e).

An example of a raw magneto-optical image is presented in Fig. 2.13 (a) and shows the flux penetration at the edge of a superconducting Nb film with a step in thickness[6]

[6]Further information about this particular sample can be found in section 4.2.1.

for $\mu_0 H = 0.3$ mT and $\beta_\perp = 1.8°$. While the edge can clearly be identified through the accumulation of flux, the noise in the image is significant. Since the signal-to-noise ratio increases as $\sqrt{N}$, a simple way to reduce the noise is to record the average of N images. Figure 2.13 (b) shows the average of $N = 500$ images at $\beta_\perp = 1.8°$ and $\mu_0 H = 0.3$ mT. The noise is reduced by a factor $\sqrt{N} \sim 20$.

However, some features in the image do not come from the magnetic signal, but are rather independent from H. This is for example the case of defects in the indicator mirror or spots due to inhomogeneous light illumination. With the assumption that these artifacts are insensitive to the magnetic field H, this constant background can be removed from the intensity, or at least weakened, by subtracting the average of $N = 500$ images at $\beta_\perp = 1.8°$ and $H = 0$ (before the field $\mu_0 H = 0.3$ mT is applied), shown in Fig. 2.13 (c). The result of this operation is shown in Fig. 2.13 (d).

Finally, it is interesting to repeat the procedure leading to Fig. 2.13 (d), but for $\beta_\perp = -1.8°$. In images taken at opposite angles $\beta_\perp$ and $-\beta_\perp$, regions where magnetic field is zero show the same intensity I_0, in contrast to regions where there is magnetic field[7]. Indeed, the Faraday rotation leads to an increase of the intensity $I(\beta_\perp)$ with respect to I_0, while it causes a decrease of $I(-\beta_\perp)$. This is shown in Fig. 2.13 (e), where the colors appear reverted in the image at $-\beta_\perp$ with respect to Fig. 2.13 (d) at $\beta_\perp$. Therefore, by taking the difference between images at $\beta_\perp$ and $-\beta_\perp$, the constant background is attenuated while the magnetic signal is approximately doubled. The result of this operation is shown in Fig. 2.13 (f), where the contrast is strikingly improved with respect to the previous panels.

While giving interesting results, this last step is practically difficult to implement on a regular basis in our setup, since it requires changing manually the analyzer angle for every value of H, which is time consuming and introduces errors on the value of $\beta_\perp$. It is however useful when the signal to be detected is particularly weak and has been successfully implemented in systems where the polarizer is coupled with a polarization rotator, allowing for fast changes of the initial direction of the linear polarization [67, 68]. For this reason, typical data acquisition and analysis is limited to the procedure leading to Fig. 2.13 (d), with N usually between 10 and 100. There are however other means to improve the contrast and signal-to-noise ratio in the images, such as differential magneto-optical imaging [69], where the difference between two images at (T,H) and $(T,H + \delta H)$ highlights the changes in the magnetic flux distribution as the applied field is modified. The same technique can also be applied to evidence the influence of slight variations in the temperature. Another possible way to enhance the images is to work directly on the sample/indicator assembly instead.

[7] Since contrast is optimized individually for each image, this might not be obvious in the images presented here.

2.3.4.2 Resolution improvement by customized sample/indicator assembly

In our system, where the Bi:YIG based indicator is placed on top of the sample, the spatial resolution is basically limited to the sum of (i) the Bi:YIG layer thickness and (ii) the gap between the indicator and the sample surface [41]. While the thickness of the Bi:YIG layer of our indicators, $d \simeq 3.5\,\mu$m, is fixed, it is possible to act on the gap between sample and indicator to enhance the contrast in the images.

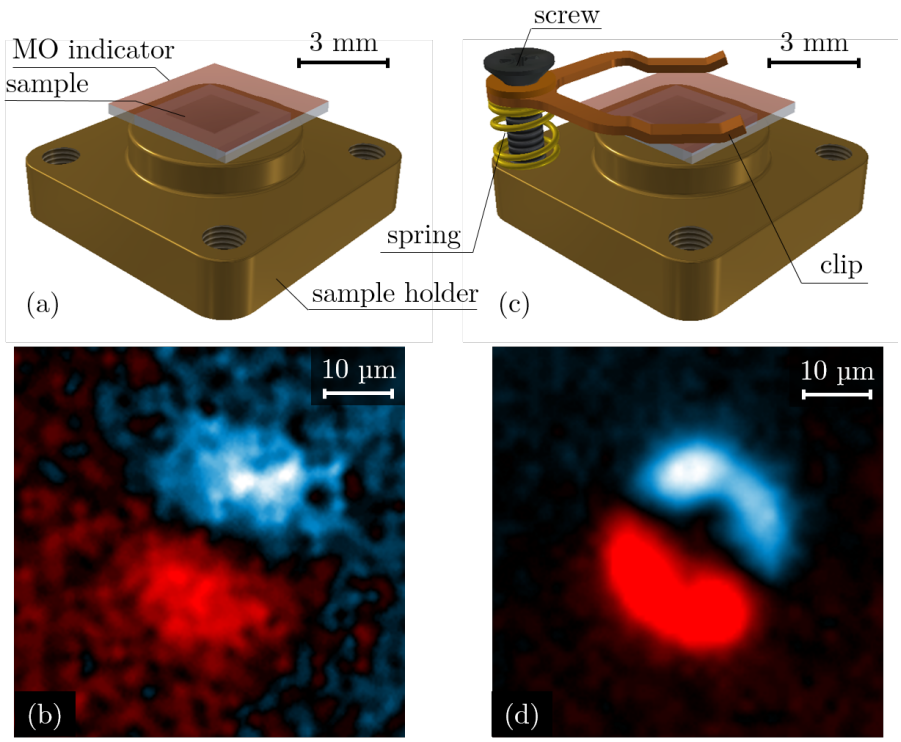

Figure 2.14: **Resolution improvement by pressing the indicator on the sample surface.** (a) Classical configuration for the MOI measurements, with the sample mounted on the sample holder, and the indicator placed on top of it. (b) Magneto-optical image of a 20 μm diameter Co disk (30 nm thick) in the configuration of panel (a), after polarization with an in-plane field of 3 mT. Dark regions correspond to zero magnetic field, while blue-white (red) areas correspond to positive (negative) magnetic field. (c) Alternative configuration where the indicator is pressed closer to the sample surface with a purposely designed metallic clip. (d) Magneto-optical image of the same disk as in panel (b), showing the enhanced signal using the alternative configuration presented in (c).

Figure 2.14 (a) shows the classical assembly, in which most of the results presented in this work were acquired. The indicator is placed on top of the sample, with a

gap z_{MOI} between them. Figure 2.14 (b) shows a magneto-optical room temperature image of a 30 nm thick Co disk with 20 μm diameter [8], after polarizing it with an in-plane field on the order of 3 mT using a commercial neodymium magnet. The stray field of the Co disk, indicating the direction of the in-plane magnetization, is visible in the image as a red (negative B_z) and blue-white (positive B_z) spot. Since the signal is quite weak, leading to poor contrast, it is important to minimize the gap between indicator and sample. The distance z_{MOI} can be considerably reduced if instead of just placing the indicator on the sample, a clip is used to press it firmly onto the sample surface, as illustrated in the sketch of 2.14 (c). This leads to significant improvement in the contrast, as shown in the image in Fig. 2.14 (d), indicating a reduced effective distance z_{MOI} between indicator and sample surface.

While this method is very effective to improve the signal-to-noise ratio, using the clip increases the risk of damaging the indicator, in particular the fragile mirror layer and especially if the sample surface is not clean and flat. Given that the sample mounting has been performed in an environment with a large amount of particles of at least 2.5 μm diameter in the atmosphere, the reduction of the gap that can be achieved by pressing with a clip is restricted by the unavoidable presence of such particles between the indicator and the sample. Another negative side-effect of using the clip is that the mechanical stress induced by the clip favors the proliferation of in-plane magnetic domains in the indicator film. For these reasons, we limit the use of the clip to the situations where it is absolutely required, for instance when the magnetic signal is quite weak or localized. As a final remark, note that other techniques exist to reduce z_{MOI}. For instance, Terao *et al.* [70] rely on the thermal contraction of Apiezon grease placed between the sample and the indicator, or tune the distance *in situ* by replacing the clip of our setup with bimorph-type piezo-actuators.

2.3.4.3 Quantitative magneto-optical imaging

Magneto-optical imaging is a qualitative technique, meaning that it does not provide direct access to the out-of-plane magnetic field B_z in the indicator, but rather to light intensity values I related to it. Therefore, caution must be exerted when interpreting the raw images, since I at a given pixel depends strongly on several parameters other than the local B_z, such as incident light intensity, exposure, depolarization effects due to the optics, or indicator tilt, to name a few. Furthermore, depending on the choice of the analyzer angle β with respect to the polarizer, pixels with the same light intensity may sometimes correspond to different values of the magnetic field. When it is desirable to recover information on the local magnetic field, protocols have been developed to convert the light intensity pixel values into absolute magnetic field

[8] More information about this sample can be found in section 2.3.5.2.

values [42, 62, 71–73]. The procedure we present here is inspired by those, but with two significant added values: (i) we use an exact pixel-by-pixel method, instead of generalizing to the whole image a calibration performed on a reference zone, and (ii) we separate the contribution of the superconductor from other sources of constant magnetic field, such as ferromagnetic structures. The complete procedure is illustrated in Fig. 2.15 using as an example a rectangular superconducting Nb film with the same two ferromagnetic disks as in the previous section as sources of inhomogeneous magnetic field.

According to the Malus law, the intensity $I(B_z, x, y)$ recorded by the camera for a pixel (x, y) in the image can be expressed as follows [42]:

$$I(B_z, x, y) = I_0(x, y) \sin^2 \left(\alpha(B_z, x, y) + \beta_\perp(x, y) \right), \tag{2.22}$$

where $I_0(x, y)$ is the incident light intensity, diminished by depolarizing effects and absorption, $\alpha(B_z, x, y)$ is the angle of rotation of the light polarization, coming from the Faraday effect for a local out-of-plane magnetic field $B_z(x, y)$, and $\beta_\perp(x, y)$ is the angle measured from the extinction configuration (90° between polarizer and analyzer). In general, the angle $\beta_\perp$ is not uniquely defined for a given image, meaning that the minimum of intensity does not occur for the same $\beta_\perp(x, y)$ at every pixel (x, y). The value of $\alpha(B_z, x, y)$ is related to $B_z(x, y)$ through the out-of-plane magnetization $M_z(x, y)$ of the Bi:YIG layer, as already stated in Eq. (2.14). Substitution of $\alpha(B_z, x, y)$ in Eq. (2.22) yields the following expression:

$$I(B_z, x, y) = I_0(x, y) \sin^2 \left(C(x, y) M_\mathrm{s} \sin \left(\arctan \left(\frac{B_z(x, y)}{B_\mathrm{a}} \right) \right) + \beta_\perp(x, y) \right), \tag{2.23}$$

where $B_\mathrm{a} = \mu_0 H_\mathrm{a}$. This equation linking $B_z(x, y)$ with the intensity $I(x, y)$ picked up by the sensor is at the core of quantitative magneto-optical imaging: provided the parameters are determined through a preliminary calibration done on a set of data were $B_z(x, y)$ is known, Eq. (2.23) can be used to convert $I(x, y)$ images to $B_z(x, y)$ field maps in any subsequent measurements.

When the range of local magnetic fields $B_z(x, y) \ll B_\mathrm{a}$, which is the case in most of our experiments, $I(B_z, x, y)$ takes a much simpler parabolic dependence on $B_z(x, y)$:

$$I(B_z, x, y) \simeq a(x, y) + b(x, y) B_z + c(x, y) B_z^2, \tag{2.24}$$

where

$$a(x,y) = I_0 \sin(CM_\mathrm{s} \sin\beta_\perp), \tag{2.25}$$

$$b(x,y) = \frac{I_0 C M_\mathrm{s}}{B_\mathrm{a}} \cos\beta_\perp \sin(2CM_\mathrm{s} \sin\beta_\perp), \tag{2.26}$$

$$c(x,y) = \frac{I_0 C M_\mathrm{s}}{B_\mathrm{a}^2} \{CM_\mathrm{s} \cos^2\beta_\perp \cos(2CM_\mathrm{s} \sin\beta_\perp) - \frac{\sin\beta_\perp}{2} \sin(2CM_\mathrm{s} \sin\beta_\perp)\}. \tag{2.27}$$

Equation (2.24) can also be written in the following form, so the physical meaning of the parameters is easier to identify:

$$I(B_z,x,y) \simeq I_\mathrm{min}(x,y) + A(x,y)(B_z(x,y) - B_\mathrm{min}(x,y))^2, \tag{2.28}$$

where

$$A(x,y) = c(x,y), \tag{2.29}$$

$$B_\mathrm{min}(x,y) = -\frac{b(x,y)}{2c(x,y)}, \tag{2.30}$$

$$I_\mathrm{min}(x,y) = a(x,y) - \frac{b^2(x,y)}{4c(x,y)}, \tag{2.31}$$

are experimental parameters to be determined for each (x,y) pixel of the image. $B_\mathrm{min}(x,y)$ is the value of the local magnetic field for which the minimum intensity $I_\mathrm{min}(x,y)$ is achieved, while $A(x,y)$ is related to the sensitivity of the Faraday-active layer of the indicator.

Calibration The aim of the calibration procedure is to extract values of $A(x,y)$, $H_\mathrm{min}(x,y)$ and $I_\mathrm{min}(x,y)$ for the system configuration of interest, i.e., for fixed sample and indicator mounting, camera parameters and analyser angle. This is done by recording a series of images, varying the external applied magnetic field $H = B/\mu_0$, as illustrated in Fig. 2.15 (a). In the case of a superconducting sample, the calibration needs to be done at a temperature $T > T_\mathrm{c}$, in the absence of superconducting signal. At this temperature, we typically record the average of 3 images for every value of $\mu_0 H$, varying between 12.5 mT and −12.5 mT by steps of 0.1 mT. Since we perform pixel-by-pixel calibration, it is important that all the recorded images overlap perfectly, i.e., unwanted drift occurring during the measurements has to be taken into account. To that end, we use the StackReg plugin [74] of the ImageJ software to correct for the small translation of the sample, on the order of 0.15 μm/min (about 0.1 px/min), due to temperature gradients in the cryostat. The correction provided by the software has

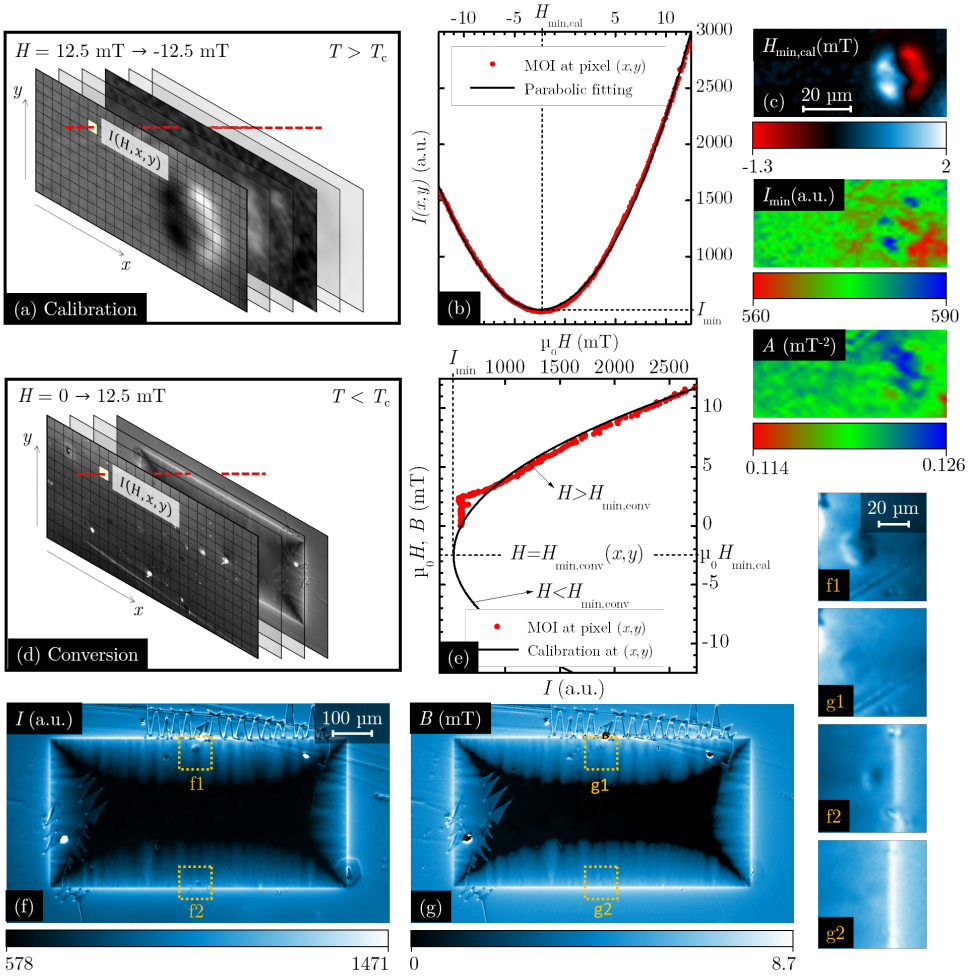

Figure 2.15: **Quantitative magneto-optical imaging.** (a) Data cube formed by the reference intensity images $I(x, y)$ recorded above T_c when sweeping the applied magnetic field H. (b) The intensity profiles $I(H)$ for each (x, y) pixel are fitted by a parabola, given by Eq. (2.28), and have a minimum I_{min} for an applied field $H_{min,cal}$. These two parameters, as well as the concavity A, are mapped in panel (c) for a small part of the sample, showing a 20 μm diameter Co magnetic disk with in-plane magnetization. (d) Sequence of images to be converted to local magnetic field B, taken below T_c when sweeping H. (e) The $I(H)$ curve for each (x, y) pixel is compared to the calibration curve to determine $B(I)$. To discriminate between the two possible values of B for a given I, the field $H_{min,conv}$ at which the minimum of intensity I_{min} occurs is compared with the applied field H: if $H > H_{min,conv}$ ($H < H_{min,conv}$), the upper (lower) branch of the reference parabola is selected. Here $H > 0$, while $H_{min,conv}(x, y) < 0$. A comparison of the original I image with the final B image is shown in panels (f-g) for a superconducting film with magnetic disks, along with enlargements (f1,f2,g1,g2) of the two disks.

an error of ± 2 px (about $3\,\mu$m).

The calibration images sequence can be regarded as a data cube made of N images with dimensions of $N_x \times N_y$ px^2, where each pixel contains the intensity value $I(H, x, y)$. First, the fluctuations of the light intensity produced by the Hg-lamp (see section 2.3.3.1) are dealt with by fitting with Eq. (2.28) the intensity $I_{\text{mean}}(H)$, corresponding to the average intensity in a 30×30 px^2 region free of defects and located far from the sample (where the magnetic field is homogeneous and close to the applied field). The fitting of $I_{\text{mean}}(H)$ returns the parabolic function $I_{\text{ref}}(H)$. Subsequently, each image $I(H, x, y)$ is corrected by multiplying it by $I_{\text{ref}}(H)/I_{\text{mean}}(H)$.

After correcting for image drift and fluctuations of intensity, we plot the intensity $I(H, x, y)$ as a function of the applied magnetic field H for each pixel (x, y) of the data cube, and fit it with Eq. (2.28), as shown in Fig. 2.15 (b). The calibration process yields the functions $H_{\text{min,cal}}(x, y)$, $I_{\text{min}}(x, y)$ and $A(x, y)$, represented in Fig. 2.15 (c). This procedure allows us to accurately relate $I(H, x, y)$ with the local magnetic field $B(x, y) = \mu_0 H(x, y)$, using a different reference curve $I(H, x, y)$ for every pixel. This means that the calibration takes into account any spatial inhomogeneity in the illumination, as well as defects and artifacts in the sample and indicator, and constant magnetic field sources other than H. Of course, we cannot recover magnetic field information for unresponsive pixels (for instance those resulting from damage in the indicator due to scratches) or when the light intensity saturates (due to local high magnetic fields), so the parameter values at these points do not have a physical interpretation.

The magnetic field $H_{\text{min,cal}}(x, y)$ represents the field at which the minimum of intensity $I_{\text{min}}(x, y)$ occurs. In the absence of fields other than the external applied field H, $H_{\text{min,cal}}$ basically corresponds to the field rotating the light polarization of an angle $-\beta_\perp$, compensating the deviation of the analyzer and polarizer from the extinction configuration. However, in the presence of a magnetic field source other than H, the additional contribution to the rotation of light polarization α also has to be compensated, thus impacting the value of $H_{\text{min,cal}}$. Therefore, $H_{\text{min,cal}}$ already provides us with a cartography of the magnetic field source, as can be seen in the example of the magnetic disk presented in Fig. 2.15 (c). Provided we subtract the background coming from $\beta_\perp(x, y)$, we have access to the average field generated by the source over the thickness of the Faraday-active layer. Moreover, the $I_{\text{min}}(x, y)$ distribution shows the inhomogeneities in the background intensity, but it also reflects the shape of the field source. Indeed, a uniform external magnetic field H can never compensate exactly the local magnetic field B generated by an inhomogeneous magnetic field source, since B will be non uniform through the thickness of the indicator active layer, due to the field decay with the distance. The partial compensation thus leads to an increase in I_{min}. Finally, the parameter $A(x, y)$ is related to the sensitivity of the indicator, and may

also vary due to composition inhomogeneities. A careful look at Fig. 2.15 (c) allows us to identify some traces of the magnetic dot on the $A(x, y)$ parameter, which fall within the error bar of the procedure.

Conversion We will now use this calibration to convert the intensity to magnetic field in a set of images, in the interesting case of a superconducting sample with magnetic disks on top. At the end of the conversion procedure, the inhomogeneous field they produce is absent from the field map, leaving only the signal of the superconductor. For that purpose, we usually take a set of 10 images/field at $T < T_c$ applying a zero field cooling procedure and increasing $\mu_0 H$ from 0 to 12.5 mT by steps of 0.1 mT, as illustrated in Fig. 2.15 (d). As before, we correct the thermal drift and the fluctuations of the incident light in the images, taking care of choosing exactly the same reference 30×30 px^2 region as for the calibration. Ideally, the $I_{\text{mean}}(H)$ parabola in the reference square should be, after correction, the same as for the calibration set.

We take the $I(H, x, y)$ curve for every pixel of the data cube and find the value of the applied field $H_{\text{min,conv}}$ at which the minimum intensity I_{min} appears (red curve in Fig. 2.15 (e)). This is an important step in order to convert the intensity into local magnetic field, since for each value of $I(H, x, y)$, there are two possible corresponding values of $B(x, y)$, one on each branch of the calibration parabola (black curve in Fig. 2.15 (e)). The way to choose the proper B for a given $I(H, x, y)$ is to compare H with $H_{\text{min,conv}}(x, y)$: if $H < H_{\text{min,conv}}(x, y)$, the correct $B(I)$ parabola branch to consider is the lower branch; if $H > H_{\text{min,conv}}(x, y)$, the upper branch must be considered. For this reason, and to avoid the imprecision close to the parabola minimum, it is best to choose in advance the analyzer angle appropriately, if possible so that the minimum of intensity does not occur in the range of applied fields H. This is what was done for the measurements presented here, since from Fig. 2.15 (e), we see that $H_{\text{min,conv}}(x, y) < 0$, while $H > 0$.

The result of the conversion procedure is shown in Fig. 2.15 (f-g), for a rectangular superconductor with magnetic disks such as the one shown in Fig. 2.15 (c), highlighted by the yellow dotted rectangular frames. Figure 2.15 (f) shows the original light intensity image compared with the final quantitative magnetic field image in Fig. 2.15 (g). Note that in general, the background of the sample is more homogeneous, and some inhomogeneities in the indicator response are nearly corrected, such as the circular spot in the lower right corner of the sample for instance. Moreover, using this procedure, we can significantly attenuate the signal coming from ferromagnetic materials (with the assumption the signal does not change in the range of fields we apply) and separate it from the superconductor's contribution. In this particular case, the magnetic disks are notoriously visible in panel (f), but are hardly visible in panel (g). This is confirmed by the direct comparison of the enlargements of the disks in panel (f) (images f1 and

f2) with the same regions in panel (g) (images g1 and g2). Unfortunately, magnetic domains and artifact arising from the Bi:YIG layer change as the magnetic field is ramped, and can thus not be properly accounted for using this procedure. However, as we explain in the next section, it is still possible to remove them from the images to some extent.

Note that our quantitative procedure does not take into account possible in-plane components of magnetic field that might affect the Faraday rotation in the indicator film [62, 72]. In-plane components are primarily induced by non-homogeneous magnetic field sources such as superconductors or ferromagnets. For the systems we study in the present thesis, we expect these components to lie below a few mT and therefore to be substantially smaller than the saturation magnetization of the indicator films ($B_{\mathrm{a}} \sim 100$ mT). This justifies neglecting this effect and the associated corrections. Furthermore, consideration and estimation of in-plane components involves elaborate protocols of inversion of magnetic field maps to get current density distribution maps, which are then used to correct the magnetic field information in an iterative manner. The first iteration gives the out-of-plane component (B_z) only, and even after correction due to in-plane components, most of the features in B_z are not altered significantly. As a consequence, the features we are interested in would not change noticeably by including these corrections.

2.3.4.4 Correcting for the indicator artifacts

We usually take particular care to avoid the proliferation of magnetic domain walls between domains with in-plane magnetization in the Faraday-active layer of the indicator, since the local magnetic field is modified in their presence and the technique can therefore no longer be considered as non-invasive [75]. These magnetic domains appear as triangular-shaped regions where the intensity undergoes a jump compared to the neighboring regions, thys degrading the clarity of the images and sometimes hiding actual sample features. In this section, we present an original method to reduce the impact of the indicator magnetization domains on the images, by correcting the concerned areas. As a proof of concept, we apply our procedure in a situation where domains proliferation is favorable, which is the case when large gradients of magnetic field are present. This is clearly visible in the image shown in Fig. 2.16 (a), representing the magnetic field distribution in a rectangular superconducting Nb sample[9] at $T = 3.6$ K for a perpendicular applied field of $\mu_0 H = 2.1$ mT [76].

The correction algorithm, developed by S. Blanco Alvarez, takes as input the 12-bit gray scale image obtained from the experiment. First, the boundaries of the magnetic domains are drawn by applying a discrete differential operator (Sobel filter), based on

[9] More details about this sample can be found in Appendix A.

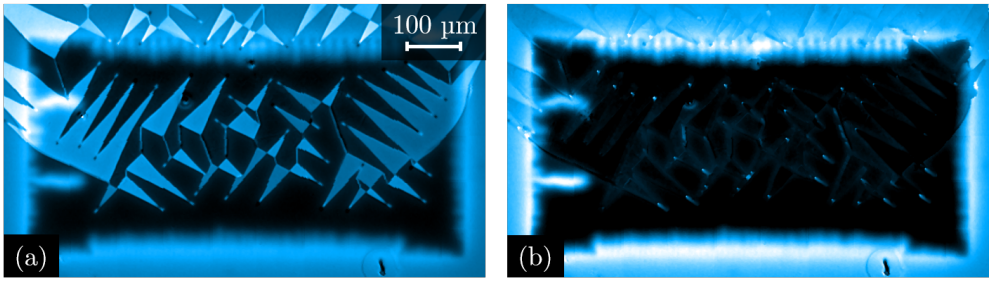

Figure 2.16: **Illustration of the correction of the indicator magnetic domains in a MO image.** (a) Original image of a $800 \times 400\,\mu m^2$ Nb superconducting film at $T = 3.6$ K and $\mu_0 H = 2.1$ mT [76], where the triangular artifacts pollute the contrast. (b) Image after treatment with the correction algorithm, showing an enhanced contrast.

the value of the intensity gradient at each pixel, as an edge detector. This operation creates a black and white boundary map of the image. In this map, we select manually the regions corresponding to artifacts due to the indicator magnetization domains. We assume that the effect of a domain on the underlying image is to shift the intensity by a constant value, possibly different for every artifact. In order to determine these constants, the user is required to provide two reference points for each artifact, one inside and one outside the domain. The difference between the intensity at these two points gives the correction to apply.

Finally, using the boundaries map drawn with the edge detector, we apply the appropriate correction to each domain using a flood fill algorithm. Since the corrections are based on a map of the boundaries and applied only to non boundaries pixels, this method leaves at least a single uncorrected pixel line between corrected domains. To smooth the image, an optional step is to replace each pixel of the boundaries by the mean value of the nearest pixels not belonging to any boundary. This is however not always helpful as this step requires a precise determination of the boundaries, which cannot always be achieved, for instance in particularly noisy pictures or for magnetically textured samples, where it could result in a degraded picture quality.

The result of the above described correction procedure is illustrated in Fig. 2.16 (b). As a final remark, since this method manipulates the values of the intensity, caution must be exerted when trying to extract quantitative information from the corrected image.

2.3.5 Application of quantitative magneto-optical imaging

In the remainder of the chapter, we apply the conversion protocol detailed above to study various magnetic field sources. We start by analyzing a simple non-superconducting

system made of magnetic Co bars and use it to further characterize and calibrate the MOI system. In a second step, we investigate a heterostructure where Co magnetic disks are positioned on top of a Nb superconducting film. Next, we consider the case of a micro-coil as a tunable inhomogeneous magnetic field source, allowing us to precisely establish the field resolution of the magneto-optical indicator.

2.3.5.1 Arrays of magnetic bars

One of the crucial parameters determining both the spatial and magnetic field resolutions of MOI is the gap between the sample and the indicator placed on top of it. This distance is difficult to control, since it depends strongly on the roughness and the cleanliness of the sample and mirror surfaces, and it is therefore also challenging to reproduce, making it problematic to compare images from different experiments. Moreover, quantifying the spatial and field resolution of the technique is not straightforward, since it requires a precise knowledge of the field at the garnet position and the geometry of the field source. For these reasons, it is of interest to design localized magnetic field sources with a well-known field distribution. This can be achieved by using parallelepiped magnetic bars, for which the magnetic field distribution can be calculated analytically [77].

Panels (a) and (b) of Fig. 2.17 show the structure of the sample, consisting of several 800×800 μm^2 arrays of nearly parallelepipedic 30 nm thick Co bars of length L and width W. L is the nominative length of the bars and doesn't take into account the round edges, effectively reducing the size of the domain with in-plane magnetization. Additional layers of Ti and Au cover the sample to prevent oxidation. All the arrays are fabricated on the same substrate, guaranteeing that they are all observed under similar experimental conditions. We consider three different arrays: $L = 20\,\mu$m and $W = 5\,\mu$m, $L = 10\,\mu$m and $W = 3\,\mu$m, and $L = 5\,\mu$m and $W = 1\,\mu$m.

We applied quantitative magneto-optical imaging to map the out-of-plane magnetic field $B(z_{\mathrm{MOI}})$ generated by the magnetic bars in the magneto-optical indicator, located at a distance z_{MOI} from the sample surface. As explained in the calibration procedure in section 2.3.4.3, we sweep the perpendicular applied field $\mu_0 H$ from 12.5 mT to -12.5 mT by steps of 0.1 mT and record the average of 3 images for every value of H. Before starting to observe the sample, we magnetize the Co bars along their length with a permanent magnet. Note that the maximum applied field $\mu_0 H = 12.5$ mT does not change irreversibly the magnetization M in the magnetic bars, a fact supported by the comparison of images before and after the calibration procedure. Any reversible changes in M are accounted for by the calibration. Figure 2.17(c) shows the local magnetic field B map of the magnetic bars array with $L = 20\,\mu$m and $W = 5\,\mu$m. In this image, each individual bar is identified by a pair of red and blue-white dots,

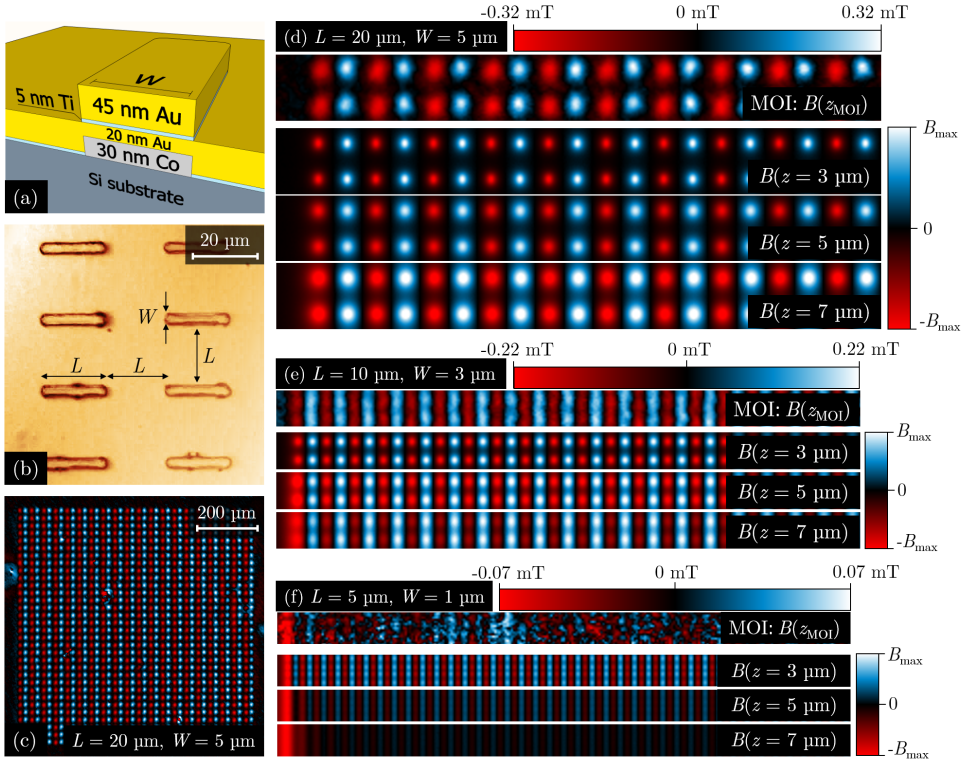

Figure 2.17: **Quantitative magneto-optical imaging on magnetic bars.** (a) Schematic structure of a 30 nm thick Co magnetic bar of length L and width W. (b) Optical image showing the periodicity of the Co bars arrays, characterized by a spacing L between neighboring bars. (c) Magnetic field image, obtained via MOI, of a full $800 \times 800\,\mu\text{m}^2$ array of magnetic bars with $L = 20\,\mu$m and $W = 5\,\mu$m. (d) Zoom on a half row of bars taken from the left side of panel (c). This experimental field distribution $B(z_{\text{MOI}})$ is compared with the exact analytic solution for $B(z)$, based on Eq. (2.32), taking into account the indicator active layer thickness $d \simeq 3\,\mu$m. (e) Same for a sample with $L = 10\,\mu$m and $W = 3\,\mu$m, at the limit where the stray field of a single bar can be resolved. (f) Same for a sample with $L = 5\,\mu$m and $W = 1\,\mu$m, where single bars cannot be seen any more. The response is dominated by the stray field at the border of the array. From the comparison of the theoretical and experimental magnetic field distributions, we estimate z_{MOI} between $5\,\mu$m and $7\,\mu$m.

representing the stray field of opposed polarity associated with the bar extremities. The ratio $m = L/W = 4$ is on the order of magnitude of the expected m for the appearance of single domains in Co bars similar to ours [78], a fact that is evidenced by the pairs of dots in the magneto-optical image. Similar single domain structures are also expected for the other two arrays of Co bars.

Knowing the dimensions of the array of bars and approximating their geometry by a parallelepiped, we can calculate the local magnetic field map at a distance z of

the sample surface. Indeed, as was shown in Ref. [77], the magnetic field generated by a parallelepipedic single domain with magnetization M and dimensions $L \times W \times t$ can be calculated analytically. The out-of-plane component of the magnetic field, that MOI is sensitive to, can be expressed as follows at the coordinates (x, y, z):

$$B(x,y,z) = \frac{\mu_0 M}{4\pi} \sum_{k,l,m=1}^{2} (-1)^{k+l+m} \ln\Bigg((x-x_0) + (-1)^k \frac{W}{2} + \sqrt{\left((x-x_0) + (-1)^k \frac{W}{2}\right)^2 + \left((y-y_0) + (-1)^l \frac{L}{2}\right)^2 + \left(z + (-1)^m \frac{t}{2}\right)^2} \Bigg). \tag{2.32}$$

The bar has its center at the point of coordinates $(x_0, y_0, 0)$ and has its main axis oriented along the y-axis. We calculate the field generated by the whole array by adding up the contributions of all the magnetic bars, obtained by changing x_0 and y_0 in the previous equation. Since the active layer of the indicator has a finite thickness[10] $d \simeq 3\,\mu$m, it is imperative to account for the fact that the magnetic field is not constant through the indicator. The magneto-optical images therefore represent the average of the magnetic field over the distance d. In the calculations, the magnetic field distribution $B(x, y, z_0)$ obtained for a gap z_0 between the indicator and the sample surface is obtained by averaging 31 distributions $B(x, y, z)$, calculated by sweeping z from z_0 to $z_0 + d$ in steps of $0.1\,\mu$m.

Figure 2.17(d) shows a comparison of the experimental out-of-plane magnetic field $B(z_{\mathrm{MOI}})$ with the calculations based on Eq. (2.32), for three distances z between sample and indicator: 3 μm, 5 μm and 7 μm. The left side of the images corresponds to the left edge of the Co bars array shown in Fig. 2.17 (c). We chose linear color scales to represent B, meaning that we can directly compare visually the theoretical magnetic field distributions with the experimental one. This allows us to estimate the distance z_{MOI}, between 5 μm and 7 μm. Moreover, the experimental image gives a maximum field $B_{\max} = 0.32 \pm 0.03$ mT. This can be compared with the maximum field $B_{\max}$ obtained with the analytical expression, where $M = 1.4 \times 10^6$ A/m is taken as the saturation magnetization of Co [79]. This gives $B_{\max} = 0.99$ mT, 0.49 mT and 0.29 mT for distances z of $3\,\mu$m, $5\,\mu$m and $7\,\mu$m, respectively. These values allow for an estimation of $z_{\mathrm{MOI}} \sim 6.3\,\mu$m falling in the range of the distances anticipated by visual inspection.

From the magneto-optical data, we observe that the distance between the two poles of a magnetic bar, i.e., the distance between the center of the red and blue-white dots, is not 20 μm as in the theoretical field maps, but is actually $\sim 18\,\mu$m. This is due to the fact that the magnetic bars are not perfectly parallelepipedic but have round corners, as shown in the optical image in Fig. 2.17 (b). Therefore, the influence of the

[10] This value is within the error bar of $d = 3.5 \pm 0.5\,\mu$m determined in section 2.3.2.2.

bars borders, where the magnetization tends to align with the edges to minimize the energy of the system, reduces the effective size of the domain of magnetization M.

Panels (e) and (f) of Fig. 2.17 follow the same principle for arrays of magnetic bars with $L = 10\,\mu$m and $W = 3\,\mu$m, and $L = 5\,\mu$m and $W = 1\,\mu$m respectively. In the field map of Fig. 2.17 (e), based on MOI, the single poles of the magnetic bars can barely be resolved, meaning the spatial resolution of our system is on the order of 5 μm for this particular z_{MOI}. The analogue poles of neighboring bars look nearly connected and form long stripes extending in the direction perpendicular to the bars main axis. Comparison with the theoretical field maps gives $z_{\mathrm{MOI}} \sim 6\,\mu$m and confirms the value we found based on Fig. 2.17 (d). Note that here, in comparison to the larger bars, B_{max} decayed to 0.22 ± 0.03 mT in the magneto-optical image, while it is 0.65 mT, 0.30 mT and 0.19 mT in the calculations for $z = 3\,\mu$m, $5\,\mu$m and $7\,\mu$m, respectively.

In figure 2.17(f), the perpendicular stripes observed in panel (e) nearly disappeared from the field map obtained by magneto-optical imaging, leaving as main feature in the image a bright line at the border of the bars array, where $B_{\mathrm{max}} = 0.07 \pm 0.03$ mT. This means the magnetic resolution of our system is better than 0.1 mT for the z_{MOI} distances estimated here. The theoretical field maps give $B_{\mathrm{max}} = 0.26$ mT, 0.14 mT and 0.09 mT for $z = 3\,\mu$m, $5\,\mu$m and $7\,\mu$m, respectively, which is in fair agreement with the z_{MOI} value estimated previously.

In the next section, we will increase the complexity of the signal detected by magneto-optical imaging, by adding a superconducting film to the localized source of magnetic field produced by magnetic disks.

2.3.5.2 Magnetic Co disks on top a superconducting Nb film

The very same system that has been used to illustrate the protocol of I-B conversion in Fig. 2.15 and the reduction of the sample-indicator gap in Fig. 2.14 is now analyzed in more detail. The sample under study consists of a rectangular $800 \times 400\,\mu$m^2 Nb film (100 nm thick) with two Co disks (30 nm thick) on top of its surface, as shown in Fig. 2.18 (a). The critical temperature of the Nb film is $T_{\mathrm{c}} = 9.0$ K, as determined by ac magnetic susceptibility measurements, while dc magnetic measurements confirmed a strong in-plane magnetic anisotropy of the Co disks.

The conversion procedure allowed us to determine the values of the magnetic field on top of and around the disks. At zero applied field, the extreme values around the poles are, $B_z = 2.4 \pm 0.3$ mT for the big disk (20 μm), and $B_z = 1.5 \pm 0.3$ mT for the $10\,\mu$m disk. For the range of values of the applied field H, the field produced by the disk typically exceeds the field of the flux penetrating in the superconducting sample, and therefore masks the contribution of the latter to the total field. For this reason, the image conversion method presented in section 2.3.4.3 proves very useful, since it

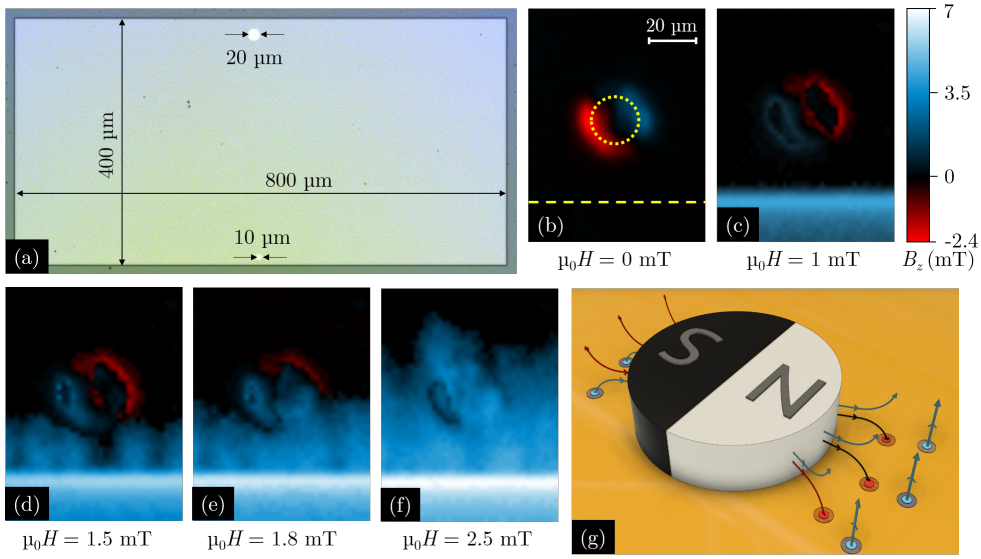

Figure 2.18: **Influence of the Co disks on the flux penetration in a superconducting Nb film.** (a) Optical image of the $800 \times 400\,\mu\text{m}^2$ Nb film (100 nm thick), where the two 30 nm thick Co disks with a diameter of $20\,\mu$m and $10\,\mu$m are located at $20\,\mu$m and $10\,\mu$m, respectively, from the sample edge. (b) Magnetic field distribution of the $20\,\mu$m diameter Co magnetic disk at $T = 10$ K. The disk is outlined by the yellow dotted circle, while the border of the superconductor is marked by the dashed line. The sample is subsequently cooled down to $T = 3.7$ K and a sequence of magneto-optical images is recorded for (c) $\mu_0 H = 1$ mT, (d) $\mu_0 H = 1.5$ mT, (e) $\mu_0 H = 1.8$ mT and (f) $\mu_0 H = 2.5$ mT. These images show the magnetic field distribution after the field of the disk, represented in (b), has been removed following the procedure described in section 2.3.4.3. Panel (g) shows a sketch of the interaction between a magnetized Co disk and the superconductor film below. The indicator positioned on top of it is not shown for the sake of clarity. Field lines representing negative (positive) B_z components are in red (blue). Near the magnetized disk, the positive field as seen by the indicator is opposed to the field in the superconductor below. The vertical blue lines at the right side of (g) represent the field lines from the applied field H.

allows to isolate the contribution of the superconductor from the stronger signal of the Co disks.

In Fig. 2.18, we show the influence of the magnetic disks on the flux penetration in the superconducting Nb film. Beforehand, the disks were magnetized at an angle with respect to the closest sample border, represented with the yellow dashed line in Fig. 2.18(b). Panel (b) represents the magnetic field at $T = 10$ K for the $20\,\mu$m diameter disk, outlined with the dotted yellow circle. The field is clearly visible as red and blue spots corresponding respectively to negative and positive B_z. The sample is subsequently cooled down to $T = 3.7$ K and the applied field H is increased. Images obtained following the procedure described in section 2.3.4.3, and where the magnetic

field landscape in panel (a) is thus removed, show the magnetic field distribution for (c) $\mu_0 H = 1$ mT, (d) $\mu_0 H = 1.5$ mT, (e) $\mu_0 H = 1.8$ mT, and (f) $\mu_0 H = 2.5$ mT. In Fig. 2.18 (c), no magnetic field has penetrated into the superconducting layer yet and the magnetic disk signal should have been removed. However, some magnetic signal is visible around the magnetic disk which might be attributed to the influence of the superconducting screening currents, repelling the magnetic field distribution of the disk and thus modifying slightly the field map shown in panel (b) [80, 81].

When H is increased, magnetic flux starts to penetrate into the sample in small flux jumps (Fig. 2.18 (d)) and interestingly, it can be clearly seen that it propagates preferentially through the side of the disk having the same polarity (positive B_z) as the applied field (Fig. 2.18 (e-f)). In order to understand this behaviour, one must keep in mind that the polarity of the field generated by the disks in the vicinity of the poles is reversed in the indicator with respect to the superconductor [82], as shown in the sketch of Fig. 2.18 (g). The natural attraction (repulsion) between the vortices from the border and the antivortices (vortices) created by one of the poles is responsible for the asymmetry in the flux penetration. This is visible in Fig. 2.18 (e-f) by the enhanced magnitude of the field at the preferred side of the disk, while the other side shows a perceptible shielding of flux. Similar results are obtained for the 10 μm diameter magnetic disk, except that the influence on the flux penetration is weaker. Changing the orientation of the disk magnetization gives essentially the same results, the entering vortices being attracted (repelled) by the side of the disk with the same (opposed) polarity.

2.3.5.3 Micrometric electromagnet

Unfortunately, in the system described in the previous section we have little control other than the direction of the magnetic moment of the disks. An attempt to overcome this limitation is explored in this section where the magnetic disk has been replaced by a single turn micro-coil excited externally with a continuous current. This approach allows us to have a tunable yet localized source of inhomogeneous magnetic field, essential for determining the magnetic field resolution of the MOI technique.

Figure 2.19 (a) shows a scanning electron microscope image of the sample layout. The coil is made of Al, is 50 nm thick and has inner and outer diameters of 20 μm and 24 μm, respectively. All the measurements have been done at room temperature. Figure 2.19 (b) shows a magneto-optical image of the out-of-plane magnetic field distribution of the coil for a current $I = 50$ mA, obtained after applying the conversion procedure. To enhance the signal to noise ratio, the image is the difference between the magnetic field obtained for positive and negative currents.

Figure 2.19 (c) shows the out-of-plane magnetic field B_z at the center of the coil

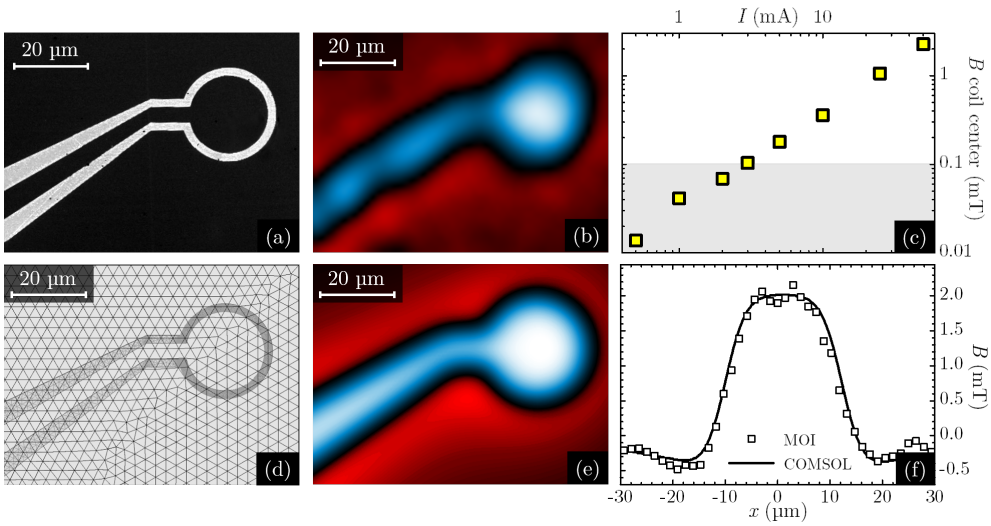

Figure 2.19: **Quantitative magneto-optical imaging on a planar coil.** (a) Scanning electron microscope image of the 50 nm thick coil made of Al. The coil has inner and outer radius of 10 μm and 12 μm, respectively. (b) Magnetic field of the coil fed by a current $I = 50$ mA, obtained by MOI with the indicator pressed on the sample surface. (c) Magnetic field B_z at the center of the coil as a function of I. The error on the magnetic field value of a single pixel is around 0.1 mT, but for extended sources such as the coil, the correlation between pixels gives a lower detection threshold of 0.01 mT. (d) Mesh for the COMSOL numerical simulations. (e) Magnetic field of the coil fed by a current $I = 50$ mA, obtained by numerical simulations, at a distance $z = 6\,\mu$m of the sample surface. (f) Magnetic field profile through the center of the coil for $I = 50$ mA taken in the magneto-optical image of panel (b) and in the numerical simulation of panel (e).

as a function of the applied current amplitude I. For a coil of radius R made of a unidimensional wire, $B_z(z)$ on the coil axis at a distance z of the coil center is given by

$$B_z(z) = \frac{\mu_0 I R^2}{2\left(R^2 + z^2\right)^{3/2}}. \tag{2.33}$$

Although the experimental coil has a finite thickness and its wire has a 2 μm width, this dependence is still valid and can be used to fit the curve of Fig. 2.19 (c). The slope gives a value of $z = 5.7 \pm 1\,\mu$m. Note that the vertical distance obtained here corresponds approximately to the distance between the middle of the indicator active layer and the coil, which gives a gap $z_{\mathrm{MOI}} \simeq 4.2\ \mu$m between the coil and the bottom of the indicator. The error on the magnetic field for a single pixel is on the order of 0.1 mT, but the correlation between all the pixels forming the coil gives a significantly lower detection threshold of around 0.01 mT, at which the coil cannot be seen anymore. This value is in agreement with the resolution limit reported previously with similar magneto-

optical indicators [41] and could possibly be pushed further down by averaging a large number of images.

A more realistic description of the magnetic field texture generated by the micro-coil can be obtained by numerical simulations, with the same geometry as the real coil, done with the COMSOL Multiphysics software. The mesh of finite elements used in the simulations is shown in Fig. 2.19 (d) and the magnetic field distribution obtained with the simulations for a current $I = 50$ mA at a distance $z = 6\,\mu$m from the coil surface is represented in Fig. 2.19 (e). The good agreement between the experimental and the numerical results is further confirmed by plotting the magnetic field profile across the coil center for both the theory and the magneto-optical images, as shown in Fig. 2.19 (f). The vertical distance $z = 6\,\mu$m obtained here corresponds to a gap $z_{\mathrm{MOI}} \simeq 4.5$ μm between the coil and the bottom of the indicator.

Chapter 3

Deflection of flux avalanches by a metallic layer

This chapter is largely based on the following work:

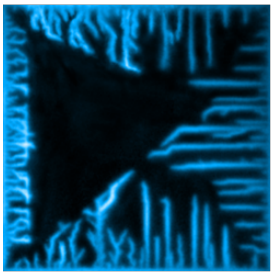

"Classical analogy for the deflection of flux avalanches by a metallic layer"

J. Brisbois, B. Vanderheyden, F. Colauto, M. Motta, W. A. Ortiz, J. Fritzsche, N. D. Nguyen, B. Hackens, O.-A. Adami and A. V. Silhanek.

New Journal of Physics **16**, 103003 (2014).

Popular summary

Superconductors are often used in applications where large electric currents are required, profiting from their ability to carry currents without energy losses. However, when superconducting materials are immersed in a magnetic field, small cylinders of magnetic flux, called vortices, enter into the material. Under the influence of an electric current, they can move and therefore lead to energy dissipation. Even worse, in some situations, millions of vortices enter suddenly into the material at velocities as high as 100 km/s, and cause a partial destruction of the superconducting state, while releasing a great deal of heat in a short period of time. These events, also called flux avalanches for their resemblance with snow avalanches hurtling down a slope, are of course detrimental for technological applications.

Fortunately, a superconductor can be, at least to some extent, preserved from flux avalanches by covering it with a metallic sheet. This is namely used to protect superconducting wires in technological applications. The physics behind this phenomenon is present in other systems, such as a magnet sliding on top of a metallic plate. In that case, the magnet is slowed down compared to when it moves over an insulating material. This happens because the displacement of the magnet induces small current loops, called eddy currents, in the metallic layer, that dissipate energy and thus damp the magnet motion. The same effect can be observed in superconductors, where vortices play the role of microscopic moving magnets. This phenomenon explains why the motion of vortices is slowed down in a superconductor coated with a metal, as well as the delayed appearance of flux avalanches.

Interestingly, there is an additional effect when a magnet moves close to the border of the metallic plate: the metal pushes it away from the border, outside of the plate. While this effect is very small for a traditional magnet and cannot be easily observed on the macroscopic scale, it becomes large in the case of flux avalanches propagating close to a metallic material, due to their very high velocities. We performed experiments relying on the magneto-optical imaging technique, presented in the previous chapter, and we observed that the regions of a superconductor covered by a metal can be shielded from flux avalanches, deviating from their initial trajectories when approaching the border of the metal. We explained these results by developing a simple model based on the above mentioned eddy currents, that qualitatively accounts for the experimental observations.

3.1 Introduction

Faraday's concept of lines of flux emanating from magnets provides a pedagogical way to visualize magnetic or other vectorial fields. Even though these field lines represent a mere mathematical construction, in type-II superconductors where a continuous field breaks up in small tubes of quantized units of flux, called vortices, they are close to acquire physical significance. In principle, as soon as a magnetic field is applied, these vortices nucleate at the sample's borders and rush to the center of the superconductor. However, inevitable and ubiquitous sample imperfections impede the motion of vortices and give rise to a gradient distribution of magnetic field, as described in section 1.3. This so-called critical state is metastable and therefore prone to relax to the equilibrium state corresponding to a more homogeneous field distribution. The relaxation process can be achieved via thermal activation of flux bundles [83, 84] over the pinning potential landscape (flux-creep) if a fast thermal diffusion allows an efficient removal of the heat produced by flux hopping, thus keeping the superconductor under isothermal conditions. A different scenario arises when thermal diffusion to the surroundings is slow. Under these circumstances, local heating leads to a reduction of the critical current, which in turn favors further vortex displacement and heat production [26]. This positive feedback loop eventually triggers a jet of flux lines bridging the border and the center of the sample in a very short time, as explained in section 1.4. Clearly, these thermomagnetic instabilities and the over-heated trail they leave behind can have very detrimental or even catastrophic consequences in technological superconducting applications, as seen for instance in the spectacular quenching of superconducting magnets [85].

It was already noted in early days that copper coating of superconducting solenoids provided a simple remedy to increase the thermal diffusion and consequently, to decrease thermomagnetic instabilities [85, 86]. Later on, similar suppression of dendritic flux avalanches has been observed in superconducting thin films with a metallic capping layer and naturally attributed to their improved thermal-sink effect [87–89]. It was only recently that an alternative mechanism, other than thermal, has been invoked to explain the suppression of flux jumps. First, Albrecht *et al.* [90] noticed that avalanches propagating into an Au-covered region change their propagation direction depending on the incident angle. This observation led the authors to conclude that large electric fields induced in the Au are responsible for these avalanche deflections and that avalanches propagate at slower velocity under the Au layer. In 2010, Colauto *et al.* [91] provided unambiguous confirmation of Albrecht's interpretation when reporting on the suppression of avalanches even if the metallic layer is located far apart from the superconductor. These findings pointed out the relevance of the electromagnetic braking of flux motion caused by induced eddy currents in the metallic layer and

questioned the hypothesis of phonon escaping through the conductive layer.

Interestingly, the problem of increased damping of superconducting vortices when moving under a conductive layer had already been experimentally and theoretically addressed by Rojo and co-workers. Indeed, Danckwerts *et al.* [92] observed an additional damping of vortex motion in a superconductor/semiconductor hybrid system caused by the eddy currents in the 2D electron gas. By changing the number of carriers with a voltage gate on the 2D electron gas, the vortex damping could be controlled. A theoretical analysis of this phenomenon was performed by Baker and Rojo [93] for a single vortex and for a chain of vortices. A more macroscopic study of the influence of inductive braking on the morphology of avalanches has been carried out in Ref. [35,94].

In this chapter, we present experimental evidence, via magneto-optical imaging (MOI), that a conductive layer (Cu) can repel flux avalanches triggered in an underlying superconducting film (Nb). By placing the conductive layer away from the borders of the superconducting film, we ensure no influence of the Cu on the early development of the thermomagnetic instabilities and guarantee that the flux avalanche is running at high speed when entering into the surface covered by the Cu [28,95]. We then address the question of whether a single vortex driven by a constant force would undergo a deflection of its trajectory when encountering a metallic layer, assuming isothermal conditions. Using a classical analogy where the vortex is substituted by a magnetic monopole [96], we demonstrate that (i) Baker and Rojo's calculations of vortex damping need to be corrected at high vortex velocities, and (ii) trajectory deflection and even total repulsion of the monopole should take place. More precisely, we show that the conductive layer gives rise to a non-monotonous damping force similar to that caused by vortex contraction or vortex expansion at high vortex velocities [97–99]. Since the indicator films typically employed in MOI setups include an aluminum mirror of about 100 nm thick which, in turn, is positioned in close proximity to the surface of the superconductor, as detailed in section 2.3.2, one should always bear in mind that, under certain circumstances, the general assumption that MOI is a non-invasive technique might not be entirely valid.

3.2 Magneto-optical imaging of superconductor partially covered by a metallic layer

In this section, samples made of a Nb superconducting layer partially covered by a Cu metallic layer are observed by MOI. After detailing the sample layout and superconducting properties, experimental results are presented for both the uncovered and covered samples, with a particular attention to the flux avalanches regime.

3.2.1 Layout and properties of Nb/Cu hybrid structures

The samples consist of a 200 nm thick Nb film of lithographically-defined square shape with 2 mm side length. In order to increase the $H(T)$ region where thermomagnetic instabilities occur [100], we have patterned the Nb film with a periodic square array of antidots[1] of 4 μm pitch and antidot size of 1.5 μm. The superconducting critical temperature is $T_c = 8.3$ K, estimated coherence length $\xi(0) \sim 12$ nm, and penetration depth $\lambda(0) \sim 92$ nm [101]. The superconducting sample layout is represented in Fig. 3.1 (a). In a subsequent process step, a 500 nm thick copper layer of triangular shape defined by electron-beam lithography was evaporated on top of the Nb sample. A 5 nm thick SiO_2 layer, prepared using chemical vapor deposition, separates the Nb and Cu films to avoid proximity effects. The Cu triangle was purposely placed far from the sample's borders in order to avert any risk of thermal shunt at the nucleation point of the avalanches. Figure 3.1 (e) shows a schematic representation of the final sample layout. After MOI experiments are done in this geometry, the Cu triangle is removed and replaced by a 500 nm thick Cu ring, depicted in Fig. 3.1 (i).

3.2.2 Flux penetration in Nb/Cu hybrid structures

The most important results are summarized in Fig. 3.1 and consist of a clear exclusion of flux avalanches by the Cu layer, as evidenced by comparing the flux entrance for the sample without Cu (Fig. 3.1 (b)) and with Cu (Fig. 3.1 (f)) in zero-field cooling conditions at $T = 2.5$ K and $\mu_0 H = 1$ mT. At a higher field $\mu_0 H = 2$ mT, the flux dendrites penetrate into the triangular area following the main directions of the underlying pinning lattice, similarly to the behaviour recently shown in [101]. This is illustrated in the image represented in Fig. 3.1 (g), to compare with the image in panel (c), taken in the same conditions for the uncovered Nb film. Similar effect is observed if the samples are first field-cooled in $\mu_0 H = 1$ mT down to $T = 2.5$ K and imaged at remanence after turning off the field, as illustrated in Fig. 3.1 (h), comparable to the image of the uncovered Nb film in Fig. 3.1 (d). In this latter case, the samples are initially full of vortices and the avalanches correspond to anti-vortices penetrating from the border of the sample [102].

The effect of the metallic layer geometry on the flux avalanches is further explored by replacing the Cu triangle with a ring, as shown in Fig. 3.1 (i). During the fabrication process, the sample broke in two parts, so the magneto-optical images in Fig. 3.1 (j) and (k) show only half of the initial sample. In zero-field cooling (Fig. 3.1 (j), $T = 2.5$ K, $\mu_0 H = 0.8$ mT) as well as in field cooling conditions (Fig. 3.1 (k), $T = 2.5$ K, $\mu_0 H = 3.5$ mT after 4.6 mT have been applied), the deflection of flux avalanches is

[1] An antidot is equivalent to a blind hole. Half of the sample has triangular antidots, the other half circular ones.

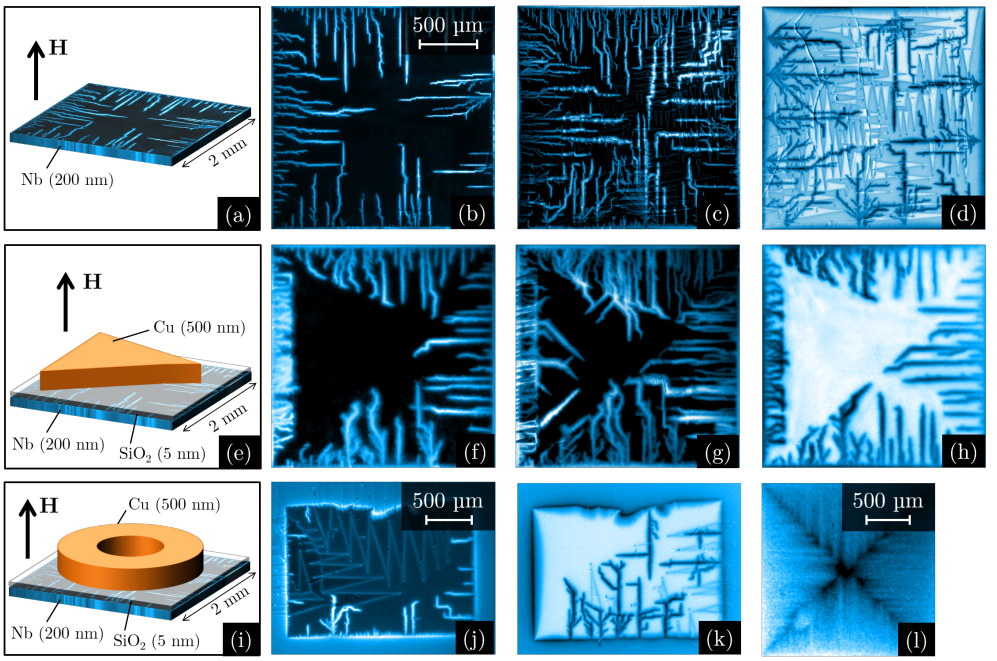

Figure 3.1: **Magneto-optical imaging on a Nb superconducting film partially covered by a Cu metallic layer.** The first row shows the experimental results for the bare Nb film, represented in (a). Panels (b) and (c) show the flux penetration in zero-field cooling conditions for $\mu_0 H = 1$ mT and 2 mT respectively, while panel (d) is in field cooling for $\mu_0 H = 3.5$ mT after 4.6 mT have been applied. The second row corresponds to the Nb film covered with a triangular Cu layer, after zero field cooling in (f) $\mu_0 H = 1$ mT, and (g) $\mu_0 H = 2$ mT. Panel (h) was obtained for $\mu_0 H = 0$ mT after field cooling in $\mu_0 H = 1$ mT. Panels (i), (j) and (k) show respectively the layout of the Nb film covered with a Cu ring and the corresponding magneto-optical images for zero field ($\mu_0 H = 0.8$ mT) and field cooling ($\mu_0 H = 3.5$ mT after 4.6 mT have been applied). Panel (l) shows the smooth flux penetration at $T = 7$ K in the triangular Cu sample.

clearly visible, especially when the flux hits the metallic layer at an angle with respect to normal incidence.

In all cases, the images unambiguously show that the avalanches avoid entering the area covered by the Cu layer and are deflected along its perimeter. Irrespective of the applied field intensity, in the avalanche regime the mean field value under the Cu-layer remains smaller than in the corresponding area in an uncovered Nb film. The images corresponding to the bilayer Nb/Cu system show a somewhat lower resolution than the bare Nb film due to the fact that the Cu spacer places the indicator further away from the Nb surface.

In the smooth (critical state) flux penetration regime, there is no difference between the samples with or without the Cu triangle. Indeed, the Nb film with the

Cu triangle at $T = 7$ K and $\mu_0 H = 1.5$ mT, represented in Fig. 3.1 (l), shows no influence of the metallic layer. This observation clearly indicates that the velocity of flux propagation plays an important role on the deflection of avalanches, and the here reported phenomenon could be thought of as a 2D skin depth effect.

3.3 Classical model for the deflection of flux avalanches by a conducting layer

A macroscopic description of the flux avalanches depicted in Fig. 3.1 requires the coupling of heat transport equations and Maxwell equations with the constitutive relation corresponding to the superconducting state and the inductive link to the conductive layer. This approach seems justified since avalanches involve a large number of vortices. Therefore, knowledge of the behaviour at the single vortex level may not be required. Moreover, numerical modelling suggests that the local temperature in the avalanche trail can rise above the superconducting critical temperature, so an avalanche can be better pictured as a propagating normal/superconductor interface rather than a moving vortex bundle [101]. All in all, an avalanche can undoubtedly be essentially described as a propagating magnetic flux front. This brings up the question of how this traveling magnetic flux front interacts with a conductive layer. In particular, we wonder whether a single individual vortex would undergo any detour of its initial trajectory when penetrating the region covered by the conductive layer. In this section we answer this question by analyzing the classical problem of a magnetic monopole, emulating an individual vortex traveling in an overdamped medium, and its interaction with a conductive plate, as illustrated in Fig. 3.2.

3.3.1 Vortex damping in an infinite conducting layer

Let us start reviewing the general problem of the forces acting on a magnetic charge (monopole) when it moves in the vicinity of a conducting plane of infinite spatial extension. We will later discuss the more complicated situation involving the border of the conductor.

As early as in 1872, J.C. Maxwell already discussed the induction of electric currents in an infinite plane sheet of uniform electric conductivity σ by a moving magnet [103]. In few words, due to Faraday's induction law, when a monopole of positive magnetic charge travels at a distance z_0 from the top of a conductive plane, it induces counterclockwise swirls of eddy currents ahead of the moving magnet (when seen from above) and a clockwise loop of eddy currents lagging behind the magnet. The magnetic field generated by these eddy currents is equivalent to that produced by a negative image of the monopole on its trailing edge and a positive image on the

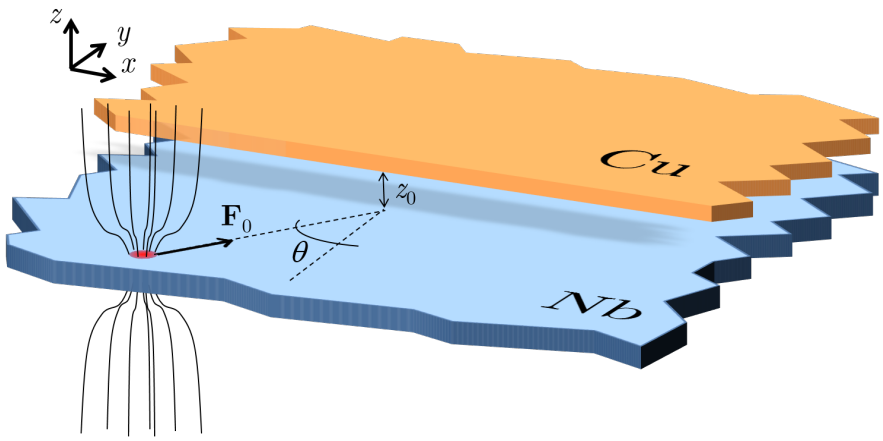

Figure 3.2: **Schematics of the classical model for the deflection of a vortex by a conducting layer.** A single magnetic monopole (vortex) propagating in an overdamped medium (Nb) is pushed towards a conducting layer (Cu) with a constant driving force F_0, forming an angle θ with the normal to the border of the conducting layer. The metallic sheet is separated by a distance z_0 from the plane containing the magnetic charge.

leading edge, both images situated at a distance $-z_0$ from the conducting plane. Due to the finite conductivity of the metallic sheet, these induced images (or eddy currents) gradually disappear, which is equivalent to say that the images propagate downward at a speed $w \propto \sigma^{-1}$. Naturally, if the conductivity is infinite, as in a superconductor, these currents will not fade out. The above considerations for a monopole can be used as building blocks for an arbitrary multipolar distribution. In particular, in the case of a dipole with magnetic moment in the $+z$ direction, the eddy current patterns are very similar to those induced by a moving monopole. When considering the forces acting on the magnet we should add the interaction of the infinite trail of images that the magnet is leaving behind its path (see lower inset in Fig. 3.3). A more modern and pedagogical description of this problem can be found in Ref. [104–110].

At low magnet velocities $v \ll w$, only the new induced positive and negative images matter, since the others have receded long before. Since the leading image is positive and the trailing image is negative, both hold back the monopole, leading to a damping force known as electromagnetic braking. In this limit, the drag force F_D is proportional to v as for a viscous medium. Interestingly, a different scenario appears at high velocities such that $v \gg w$. Now, during the time the magnet moves forward the images have not receded significantly and therefore they cancel out in the limit of infinite velocity or conductivity, leaving only the positive image. Since magnet and image are facing the same magnetic poles, they repel each other giving rise to a levitation force on the magnet whereas the drag force tends to diminish (see upper

inset in Fig. 3.3). As was already pointed out in Ref. [104, 108], similar effects should be observed irrespective of whether we deal with a magnetic monopole or a dipole perpendicular to the conducting plane.

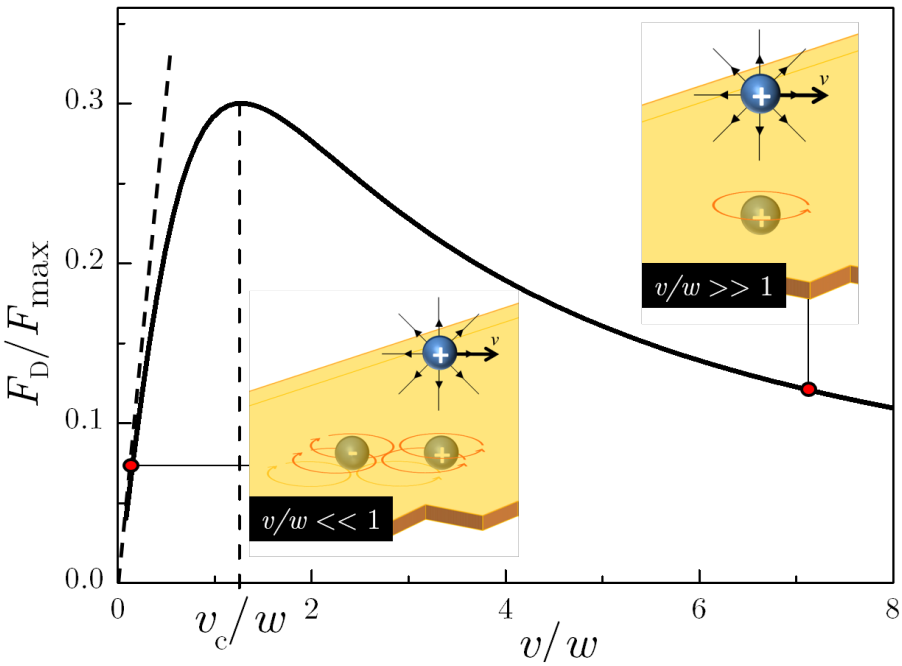

Figure 3.3: **Drag force acting on a monopole moving in the vicinity of an infinite conducting layer.** Comparison of the models developed by Baker-Rojo [93] (dashed line) and that of Reitz [104] (solid line) for the drag force acting on a moving monopole in presence of a conducting layer. The insets illustrate the current images induced in the two extreme situations by a moving monopole with positive magnetic charge. A similar picture is obtained for a moving dipole [104, 108].

The general expression for the drag force is [104]

$$F_D = \frac{\pi C}{z_0^2}\frac{w}{v}\left(1 - \frac{w}{\sqrt{v^2+w^2}}\right), \tag{3.1}$$

where C is a constant equal to $C_m = \mu_0 q^2/16\pi^2$ for a monopole, q is the magnetic charge of the monopole and z_0 is the distance between the monopole and the conductor. In the case of a dipole, C is given by $C_d = 3\mu_0 m_\mu^2/32\pi^2 z_0^2$, where m_μ is the magnetic moment of the dipole.

The lift force is given by $F_L = (v/w)F_D$ and increases monotonously with v. This force is of no particular importance in our treatment of the deflections of vortex trajectories. Figure 3.3 shows the dependence of F_D on the velocity v and an illustration of the magnetic images in the limiting cases.

It is instructive to compare the analysis presented above to the calculation by Baker and Rojo [93] of the viscosity in the case of a superconducting vortex moving close to a two-dimensional electron gas (2DEG) with conductivity σ_{2DEG}. These authors considered the electric field $\mathbf{E}$ induced in the 2DEG by the varying magnetic field of the moving vortex. They deduced an expression for the power density $\sigma_{\mathrm{2DEG}}\mathbf{E}^2$ dissipated by the eddy currents as a function of the vector potential $\mathbf{A}(\mathbf{r})$ associated with the vortex field. This leads to a drag force $\mathbf{F}_{\mathrm{D}} = -\eta_{\mathrm{2DEG}}\mathbf{v}$, with the viscosity η_{2DEG} associated with the 2DEG given by

$$\eta_{\mathrm{2DEG}} = A(t, z_0, \kappa)\sigma_{\mathrm{2DEG}}\frac{\phi_0^2}{4\pi\lambda^2}, \tag{3.2}$$

where ϕ_0 is the fundamental quantum of flux and A is a constant depending on the thickness of the superconductor t, the distance z_0 between the superconductor and the 2DEG and the Ginzburg-Landau parameter $\kappa = \lambda/\xi$. The additional viscosity η_{2DEG} should be added to the Bardeen-Stephen [12] viscosity η_{SC} produced by the vortex motion in the superconductor. Baker and Rojo showed that for a 2DEG, normally $\eta_{\mathrm{SC}} \gg \eta_{\mathrm{2DEG}}$.

It is worth noting that Baker and Rojo predict a constant damping coefficient, whereas Maxwell's analysis leads to a non-monotonous[2] $\eta(v)$. The reason for this apparent discrepancy is that the Baker-Rojo approach is only justified at low velocities, when the magnetic flux lines have the time to fully penetrate into the metallic layer [107], whereas at high velocities, the influence of the magnetic field generated by the eddy currents on the moving vortex cannot be neglected anymore. The response of the system can also be described in terms of an electric circuit [105]. At low velocities, the conductor perceives low-frequency variations of the source magnetic field. In this case, the induced currents are weak and their contribution to the total magnetic field is negligible, so the system is mostly resistive. At higher frequencies however, the magnetic field generated by the eddy currents counteracts the source fields and can no longer be neglected. The flux lines are expelled from the conductor and the system response is subsequently dominated by self-inductance effects.

The fact that at a certain critical velocity $v_{\mathrm{c}} \simeq 1.27w$ the drag force becomes smaller as v increases, resembles the non-linear damping of individual vortices moving faster than an instability velocity v^* as described by Larkin and Ovchinnikov [97]. As we pointed out above, for a vortex moving in a superconductor capped with a metallic layer, both damping coefficients should be added and consequently two instability points will appear. The critical velocity v_{c} is determined by the relaxation time of the electrons in Cu, whereas v^* is given by the relaxation time of quasiparticles in Nb. In

[2]This is somewhat similar to the motion of a solid body in a shear-thinning non-Newtonian fluid as described in Ref. [111].

our particular case of a 500 nm thick Cu layer, we find that $v_c \sim 100$ m/s, whereas for Nb $v^* \simeq 100 - 1000$ m/s [112]. These values should be compared with the velocity of avalanches in thin superconducting layers [28], which can peak at 100 km/s. A report on the influence of a metallic layer on the Larkin-Ovchinnikov instabilities was recently published in Ref. [113]. Knowing that the Larkin-Ovchinnikov instabilities are the precursors for the development of phase-slip lines [114–116], it would be also interesting to explore the delay of formation of phase slip lines and hot spots in metal-coated superconductors.

3.3.2 Vortex repulsion by the border of a conducting layer

Incorporating the effect of borders is highly non-trivial, as discussed by Davis and co-workers, who considered a monopole moving over a conducting plane of semi-infinite extension [117, 118]. The receding image technique cannot be applied in this situation and no analytic solution is known. However, by using conformal mapping techniques, Davis and co-workers managed to obtain an analytic solution in the limit of an infinite electric conductivity σ. Since the diffusion velocity w is $\sim \sigma^{-1}$, the limit $\sigma \to \infty$ can also be seen as that of an infinite monopole velocity, with $v \gg w \to 0$ [117, 118]. In this case, additionally to the drag force, the monopole experiences a lateral force $F_{\rm lat}$ pushing it away from the region covered by the perfectly conducting plane. The effect can be understood as a consequence of the asymmetric eddy current distribution which is compressed by the border of the conductor [117]. An analytical expression for $F_{\rm lat}$ was calculated for a magnetic monopole close to the border of a perfect conductor, which is equivalent to the high velocity limit of a monopole moving parallel to the border [117]. If the monopole is at a vertical distance z_0 from a semi-infinite conducting plane $y > 0$, the force can be written as

$$\mathbf{F}_{\rm lat} = -C_{\rm m}\left(\frac{1}{y^2+z_0^2} + \frac{y}{(y^2+z_0^2)^{3/2}}\right)\mathbf{e}_y. \tag{3.3}$$

The first term corresponds to a symmetric Lorentzian peak centered at $y = 0$, while the second term is asymmetric. The general shape of $\mathbf{F}_{\rm lat}(y)$, as represented in Fig. 3.4, is thus an asymmetric peak with a maximum located inside the conducting plane. The maximum force is $F_{\max} = -32C/27z_0^2$, the position of the maximum is $y_{\max} = z_0/2\sqrt{2}$ and the half-height width is $W_{1/2} = 1.79z_0$.

3.3.3 Classical model for the deflection of a vortex

Based on the aforementioned results we will now develop a model describing the trajectory of a vortex when penetrating the region covered by the metallic layer. To tackle this problem, we approximate the magnetic field of a vortex by a magnetic

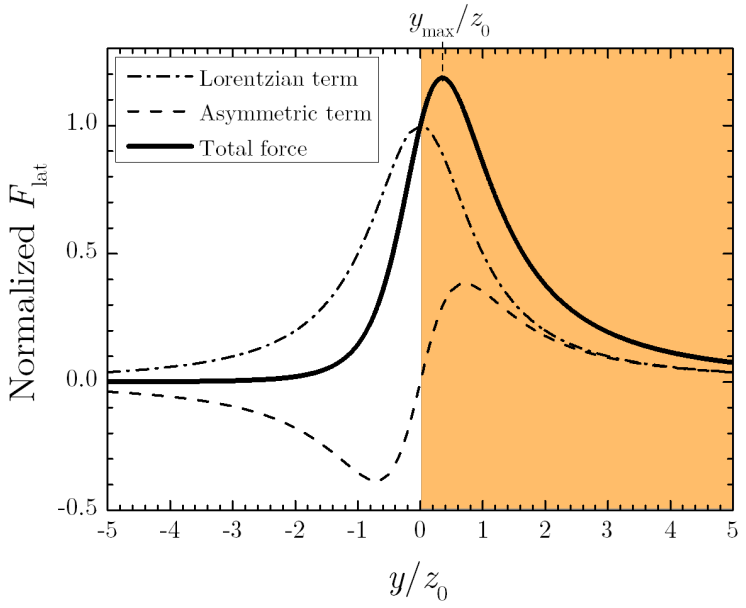

Figure 3.4: **Repulsive force acting on a monopole moving close to the border of a semi-infinite conducting layer.** Contribution of the two terms composing the lateral force $F_{\rm lat}$, given by Eq. (3.3), pushing a monopole away from a conducting plane, for $C/z_0^2 = 1$. z_0 is the vertical distance between the monopole and the conductor. The $y > 0$ half of the graph, corresponding to the location of the conductor, is colored in orange. In our simple model, we neglect the contribution of the asymmetric term and work on the main Lorentzian term.

monopole [96]. We consider the situation depicted in Fig. 3.2 where a magnet is launched from $y < 0$ towards a semi-infinite plane with perfect conductivity located at $y > 0$. Assuming perfect conductivity ensures a maximum effect of the metallic layer on the magnet. Let us consider the case where the magnet is pushed by a constant force $\mathbf{F}_0 = \eta \mathbf{v}_0$, where η is the viscosity of the medium. The initial velocity $\mathbf{v}_0$ has an angle θ with respect to the normal to the $y = 0$ interface.

The magnet is thus moving in a highly viscous medium where inertia plays no role at all, meaning that the response is determined by the instantaneous forces and by nothing in the past. This approximation is fully justified in the case of a superconducting vortex where inertial terms are known to be very small [15]. Moreover, we neglect the drag force $\mathbf{F}_{\rm D}$ (due to the eddy currents induced in the conductor) opposed to the velocity $\mathbf{v}$, as it will only slightly affect the trajectories and merely change the effective modulus of $\mathbf{F}_0$. This assumption is particularly valid in the limit $\eta \gg \eta_{\rm 2DEG}$ described by Baker and Rojo [93].

3.3.3.1 Vortex trajectories

As we anticipated above, due to the presence of the conductor, the magnet will experience a lateral force $\mathbf{F}_{\mathrm{lat}}(y)$ perpendicular to the interface. In order to obtain simple analytical expressions for the vortex trajectories, we retain only the dominant symmetric term of $\mathbf{F}_{\mathrm{lat}}(y)$ (see Fig. 3.4). Using the notations of Fig. 3.2, and writing $v_{0,x} = v_0 \sin\theta$ and $v_{0,y} = v_0 \cos\theta$, the equations of motion can be expressed as follows:

$$F_x = \eta v_{0,x} = \eta \frac{\mathrm{d}x}{\mathrm{d}t}, \tag{3.4}$$

$$F_y = \eta v_{0,y} + F_{\mathrm{lat}}(y) = \eta \frac{\mathrm{d}y}{\mathrm{d}t}. \tag{3.5}$$

By combining these two equations, we obtain the equation for the magnet trajectory:

$$x(y) = x_0 + \int_{y_0}^{y} \mathrm{d}y' \frac{y'^2 + z_0^2}{ay'^2 + az_0^2 - b}, \tag{3.6}$$

where we define the parameters $a \equiv v_{0,y}/v_{0,x}$ and $b \equiv C/\eta v_{0,x}$. From this equation, we can distinguish three cases, depending on the values of a, b and z_0.

If $z_0^2 > b/a$, i.e., when the magnet is launched close to the normal direction, we can integrate by substitution with respect to $u = y/\sqrt{z_0^2 - b/a}$. By doing this, we obtain the trajectory:

$$x(y) = x_0 + \frac{1}{a} y \Big|_{y_0}^{y} + \frac{b}{a^2 \sqrt{z_0^2 - \frac{b}{a}}} \arctan\left(\frac{y}{\sqrt{z_0^2 - \frac{b}{a}}} \right) \Bigg|_{y_0}^{y}. \tag{3.7}$$

When crossing the interface, the magnet is deflected in the direction of $\mathbf{v}_{0,x}$, as shown by the black line in Fig. 3.5. From this equation, we can extract the amplitude of the deflection Δx given by the difference between the third term of (3.7) at $y \to +\infty$ and $y \to -\infty$:

$$\Delta x = \frac{\pi b}{a^2 \sqrt{z_0^2 - \frac{b}{a}}}. \tag{3.8}$$

For given z_0 and b, the shift from the original direction, Δx, diverges when the angle of incidence of the magnet surpasses the critical angle

$$\theta_{\mathrm{c}} = \arccos\left(\frac{C}{F z_0^2} \right). \tag{3.9}$$

The evolution of $\Delta x(\theta)$ is shown in the inset of Fig. 3.5.

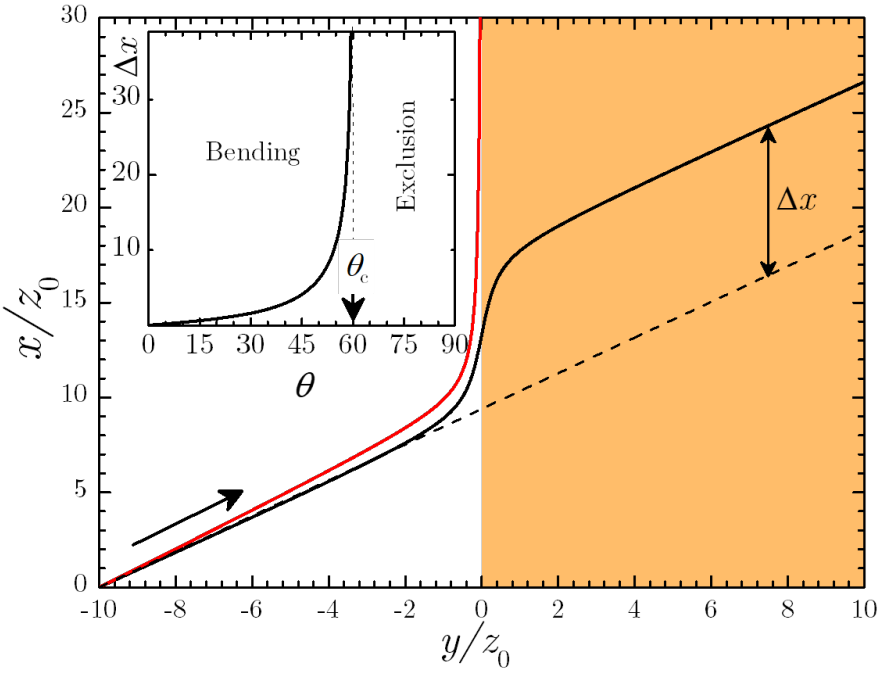

Figure 3.5: **Deflection of a magnet by a conducting layer.** Trajectory $x(y)$ of a magnet, following Eq. (3.6), launched from $x_0 = 0$, $y_0 = -10$ towards a conducting plane for $b = 1$, $z_0 = 1$ and (red) $a = 1$; (black) $a = 1.1$. The x and y coordinates are normalized by z_0. The deflection is larger as a decreases towards the critical value $a = b/z_0^2 = 1$. For smaller values of a, the magnet is completely repelled by the conductor. Inset: Δx as a function of the initial angle θ, according to Eq. (3.9), for $C = 0.5$, $F = 1$ and $z_0 = 1$. The critical angle θ_c above which the magnet does not penetrate in the region covered by the conducting layer is indicated. Bending (exclusion) of the vortex trajectory corresponds to the black (red) line in the main panel.

For $z_0^2 = b/a$, the trajectory is given by

$$x(y) = x_0 + \frac{y}{a}\Big|_{y_0}^{y} - \frac{b}{a^2}\frac{1}{y}\Big|_{y_0}^{y} . \tag{3.10}$$

In this case, the magnet never crosses the interface as the lateral force compensates exactly the driving force and therefore, the final trajectory approaches asymptotically the border of the conducting plane, following the red line in Fig. 3.5.

Finally, when $z_0^2 < b/a$ we obtain similar trajectories as that for $z_0^2 = b/a$, with the magnet running parallel to the interface but at a finite distance from it. This trajectory resembles the one followed by vortex avalanches shown in Fig. 3.1, thus suggesting that Faraday's induction law is responsible for the observed exclusion of

flux avalanches by the Cu layer.

3.3.3.2 Going beyond the classical model

A more precise calculation evaluating numerically the full expression of F_{lat} shows essentially the same results described above. Note that strictly speaking, the analysis based on Maxwell's receding images theory for an infinite plane is only valid when the skin depth δ is much bigger than the thickness of the metallic layer, $d \ll \delta$. However, a more complete analysis shows that the results are qualitatively the same in the high-frequency regime when $d \gg \delta$ [119]. In addition, we have also neglected in our analysis the fact that the magnetic images induced by the moving vortex in the conducting layer will, in turn, generate images on the superconducting layer. We would like to emphasize the fact that our classical model does not intend to *quantitatively* account for the deflection of avalanches, but to point out that, even without invoking thermal effects, Faraday's law alone should give rise to deflection of travelling magnetic flux. In our approximation, we assumed a constant force acting on the vortex. This condition can be experimentally realized when the system is driven into the free flux flow regime by applying an external current, but will certainly not be accurate enough to account for the case of vortices driven by thermomagnetic instabilities. Another important consideration is the fact that our analysis deals with a single vortex and therefore neglects collective effects. Indeed, as soon as vortices enter the region covered by the metal, they slow down and tend to accumulate at the interface, thus developing a vortex dam which impedes the motion of new incoming vortices. This effect may lead to a substantial reinforcement of vortex deflection or to a reorientation of the flux front trajectory at the interface with the metal, very much like refraction of a light beam when traversing two media with different refractive indices, and somewhat similar to the experimental results reported by Albrecht *et al.* [90]. While a theoretical model was developped to back up this hypothesis [120], supporting experimental evidence could not be found up to now.

3.4 Conclusion

Motivated by the experimental observation of the exclusion of magnetic flux avalanches in a Nb sample partially covered by a conducting capping layer, we have investigated the simplified case of the interaction of a magnetic charge (monopole and dipole) with a semi-infinite conducting plane. We have found that early theoretical descriptions for the vortex damping enhancement due to the metallic sheet needed a correction at large vortex velocities, where a decrease of the damping coefficient is expected. We also demonstrate that vortex trajectories are strongly modified when penetrating

into the area covered by the metallic sheet and may even be fully diverted from that area, thus providing a qualitative explanation for the bending of the trajectories of flux avalanches. Considering that typical MOI experiments with doped YIG films need an aluminum mirror of about 100 nm thick in close proximity to the surface of the superconductor, we question the general assumption that these measurements do not influence the experimental results. Our findings may be extended to study the damping of Larkin-Ovchinnikov vortex instabilities and phase-slip lines in current driven systems.

Chapter 4

Magnetic flux penetration in a superconducting film with a step in thickness

This chapter is largely based on the following work:

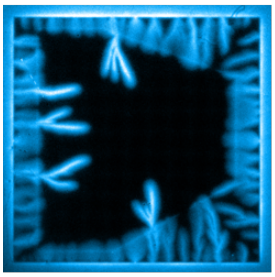

"Flux penetration in a superconducting film partially capped with a conducting layer"

J. Brisbois, V. N. Gladilin, J. Tempere, J. T. Devreese, V. V. Moshchalkov, F. Colauto, M. Motta, T. H. Johansen, J. Fritzsche, O.-A. Adami, N. D. Nguyen, W. A. Ortiz, R. B. G. Kramer, and A. V. Silhanek.

Physical Review B **95**, 94506 (2017).

Popular summary

In the previous chapter, we observed that the trajectories of flux avalanches in superconductors can be deflected when they penetrate in a region with a metallic coating. Indeed, the border of a conducting layer has a repulsive effect on moving magnetic entities, such as magnets or superconducting vortices, pushing them away from the layer. This comes from the fact that when a magnet approaches, eddy currents flow in the conductor and can be pictured as a virtual magnet, with opposite polarity compared to the real moving magnet. However, these currents, and thus the virtual magnet, lose their intensity with time, since the resistance of the conductor is responsible for energy dissipation, leading to a decay of the repulsive force.

In this chapter, we explore the effect of the conductivity of the capping layer on the efficiency of the flux shielding: the lower the resistance of the conductor, the longer the currents last, and thus the stronger the repulsion of magnets and vortices. We confirmed this by observing superconducting samples partially covered by different metallic layers, using the magneto-optical imaging technique. This investigation permitted us to address and quantify the invasiveness of the magneto-optical imaging technique, as the metallic mirror of the indicator might influence the results of the experiment under certain circumstances.

Normal metals exert a repulsive force on traveling vortices which depends on the material conductivity. This effect can therefore be maximized if the metallic capping layers are replaced by superconducting layers. After all, superconductors have zero resistance, so they produce the most efficient shielding of vortices, since the eddy currents produced by a moving vortex will not fade away. We studied this situation, corresponding to a superconducting sample with a thick central region, and we indeed observed that vortices cannot easily enter and are forced to stay outside the central area, even when they move slowly. In the opposite case, when the center of the sample is thinner than the border, vortices penetrate freely as expected for a large non-fully perforated hole.

4.1 Introduction

It has been shown in the previous chapter that magnetic flux avalanches triggered in a superconducting film are diverted from their initial trajectory when they encounter a metallic layer deposited on top of the superconductor, but electrically insulated from it [90,120–122]. This phenomenon arises from the electromagnetic braking of propagating flux, caused by the eddy currents induced in the conductive layer [86, 91–93]. The question as to whether a single element of the flux front, i.e., a superconducting vortex, could also undergo any deflection of its trajectory when entering in the region covered by a conducting layer, has been tackled by appealing to a classical analogy, consisting of a magnetic monopole (the vortex) moving in the vicinity of a conducting film.

For a conducting layer without borders, Faraday's induction law indicates that a positively charged magnetic monopole moving at a velocity v, at a constant distance from the top of the layer, generates a trail of positive and negative images, receding with a velocity given by

$$w = \frac{2}{\mu_0 \sigma d}, \tag{4.1}$$

where σ is the cap layer conductivity and d is its thickness [104–107]. Depending on the ratio v/w, two distinct limiting situations appear, as shown in Fig. 3.3. For low velocities, $v/w \ll 1$, the trail of negative images dominates over the positive images. This gives rise to a drag force ηv, where η is the damping coefficient, constant in this velocity regime. At high monopole velocities, $v/w \gg 1$, only the positive image located just below the monopole remains and the drag force tends to zero, i.e., $\eta \to 0$. In between these two regimes, the drag force reaches a maximum value at $v/w \sim 1.27$. Considering a 500 nm thick Cu layer, $w \sim 60$ m/s at 10 K, whereas v can be as high as 1000 m/s in a Nb film [112], so that flux quanta motion may cross over these two dynamic regimes.

A possible way to reach extreme high flux propagation velocities v consists in triggering flux avalanches [95] or kinematic vortices [123] with typical velocities much higher than those of Abrikosov vortices [124]. Recent experiments have indeed shown that a thick Cu layer on top of a superconducting Al film leads to changes in the dynamic response as seen in the voltage-current characteristics at high drives [113]. However, in the high speed regime, the nature of the vortex changes, the temperature locally rises, and the classical analogy brought up in the previous chapter is no longer strictly valid. An alternative way to explore the high velocity regime while keeping the Abrikosov vortex structure is to substantially decrease w, either by increasing σ or d. Notice however that when d becomes comparable to the skin depth δ, further increase of the metal thickness will not impact w. In this context, it is interesting to consider the limiting case of a conductive layer with infinite conductivity, where the damping

contribution of the eddy currents become negligible, in opposition to the velocity-dependent case when using a normal metal. The closest way to implement a perfect conductivity layer is to replace the metal by a superconducting film. As originally discussed by Giaever [125], the resulting superconducting bilayer separated by a thin insulating film exhibits electric and magnetic responses similar to those obtained for two films directly short circuited. This happens because the magnetic coupling between two collinear pieces of vortex increases as the thickness of the insulating film decreases. In the limiting case of no insulating layer at all, this corresponds to a superconductor with a step in thickness.

It is precisely the investigation of this limiting case that motivates the present chapter. To that end, we first extend the results presented in the previous chapter to explore the variations of the conductivity and thickness of a metallic layer deposited on top of a superconductor. Interestingly, these measurements suggest that certain precautions need to be taken to ensure that the invasiveness of the magneto-optical imaging (MOI) technique remains to a minimum level [126]. We then address the particular case of very high conductivity, corresponding to a superconducting film with a step in thickness, the central part of the sample being thicker than its borders. As anticipated above, this system can be considered as the superposition of two superconducting films of different thickness. The MOI technique shows that at low enough applied fields, the flux front is unable to penetrate into the thicker part of the sample. This effect is further reinforced by the increase of line vortex energy, not considered in our classical model. This behaviour contrasts with what is observed in a sample with a thinner center. In the last section, we discuss the flux penetration and interaction with a thickness step at the single vortex level as described by time-dependent Ginzburg-Landau simulations. The present study is also relevant for understanding the flux penetration in superconducting samples with terraces and thickness modulations [127], and complements early investigations of static flux distributions near surface steps [128, 129] and in mesoscopic samples [130].

4.2 Magneto-optical imaging on superconducting films partially covered by a conducting layer

In this section, the experimental results on superconducting films partially covered by a conducting layer, either metallic or superconducting, are presented. First, the fabrication process and the properties of the samples are described. Then, the effect of the capping layers is investigated in the smooth flux penetration and in the flux avalanches regimes via MOI, for metallic layers first, and subsequently for superconducting films with a step in thickness.

4.2.1 Samples fabrication and properties

The superconducting properties of a 140 nm thick 2×2 mm^2 Nb film, without capping layer, have been studied in Ref. [76] and are represented in Fig. 4.1. The main panel of Fig. 4.1 shows the upper critical field $H_{c2}(T)$ as determined from magnetization $M(H)$ loops. From these data, the transition temperature is $T_c = 9$ K, and by fitting with the Ginzburg-Landau expression $H_{c2}(T) = \phi_0/2\pi\xi^2(T)$, where $\xi(T) = \xi(0)/\sqrt{1-T/T_c}$, we deduce $\xi(0) = 9.7$ nm. The dashed area indicates the $H(T)$ region where thermomagnetic instabilities, precursor to flux avalanches, develop, as evidenced by sudden jumps in $M(H)$ [40]. This region may slightly change from one experimental instrument to another, depending of the refrigeration power, environment, and heat removal efficiency. The inset shows the field dependence of the critical current density $J_c(H)$ obtained from magnetization measurements at $T = 5$ K.

The superconducting samples partially covered by a metallic layer are 2×2 mm^2 Nb films with thickness of 140 nm, fabricated on a 2" Si wafer by e-beam evaporation in a UHV system. A sketch of the resulting heterostructure is represented in Fig. 4.2 (a). A 5 nm thick SiO_2 layer is deposited on top of the Nb by magnetron sputtering, in order to avoid proximity effects between the superconductor and the metal. In a subsequent process step, either a 500 nm thick copper or 100 nm thick gold layer of polygonal shape, defined by optical laser lithography, is evaporated on top of the structure. The metallic polygon is placed away from the sample borders so as to permit magnetic flux avalanches to be triggered freely at the borders of the Nb film. Moreover, this particular shape allows the flux front to reach the metal at different angles of incidence.

The samples with a central thickness step, represented in Fig. 4.3 (a) and (e), were fabricated according to the following protocol: a 200 nm thick Nb film was deposited by dc-sputtering on a 2" Si wafer, with a deposition rate of 0.67 nm/s while keeping the substrate at room temperature. It was then coated by a protective photoresist layer before dicing the substrate to a smaller size (20×30 mm^2). After cleaning with acetone, a negative tone photoresist mask was defined, shaping the polygonal central part of the sample. Ar ion milling was performed until the thickness of the uncovered Nb was reduced down to 140 nm, so they can be readily compared with the samples with a metallic capping layer. To fabricate the thin center samples, an additional step was realized, consisting in the preparation of a second soft mask of positive photoresist defining the central part of the Nb sample. This was followed by an ion milling of the thin center to reduce its thickness to 80 nm. A last soft mask of positive photoresist defining the square shape of the outer rims of the samples was then prepared, before etching away the surroundings of the squares with CF_4. A final dicing step was performed in order to have individual chips, each carrying one of the co-fabricated samples. For the sake of comparability, the geometrical shape

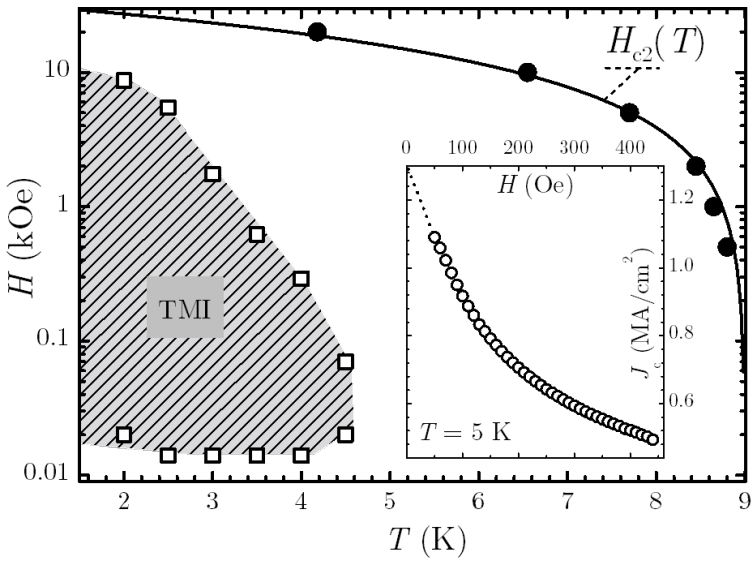

Figure 4.1: **Superconducting properties of bare Nb films.** The main $H(T)$ graph highlights the temperature dependence of the upper critical field, $H_{c2}(T)$, obtained from magnetization measurements in a 2×2 mm^2 bare Nb film without triangular indentations. The line is a fitting based on the Ginzburg-Landau expression. The dashed area indicates the $H(T)$ region where thermomagnetic instabilities (TMI) leading to flux avalanches develop. The inset shows the field dependence of the critical current density, $J_c(H)$, obtained from magnetization measurements at $T = 5$ K. The dotted line at low fields is a guide to the eye.

of the central thickness step has been made identical to that used for the polygonal metallic layers. At the middle of each side of the samples square outer rim, a $10\,\mu$m long and wide triangular indentation was lithographically defined in order to facilitate the penetration of magnetic flux through this point [76] and to better visualize the influence of the thickness step. The role of these indentations is addressed in more details in Appendix A.

4.2.2 Flux penetration in superconducting films partially covered by a metallic layer

In order to assess the influence of a metallic layer on the superconductor, we first recorded the flux penetration in Nb films partially covered by a metal (either 500 nm thick Cu or 100 nm thick Au), represented in Fig. 4.2 (a). Panel (b) shows the magnetic field in the Nb film with 500 nm thick Cu after cooling down to 5 K and subsequently applying an out-of-plane field $\mu_0 H = 4.8$ mT (zero field cooling procedure). From the image, it is clear that the flux penetration is undisturbed by the metal. This can be understood by comparing the velocity v at which the vortices move, typically

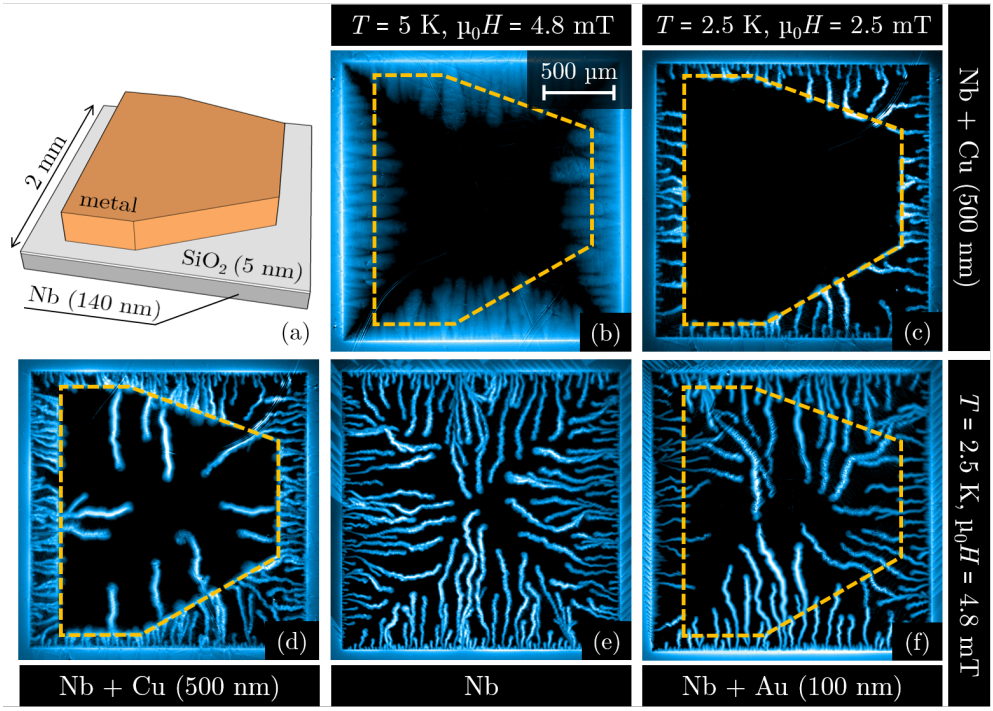

Figure 4.2: **Flux penetration in a superconducting film partially covered by a metallic layer.** (a) Sketch of the 140 nm thick Nb films partially covered by a polygonal metallic layer, either 500 nm thick Cu (panels (b-d)) or 100 nm thick Au (panel (f)). All the magneto-optical images were obtained after cooling down the sample before applying an out-of-plane magnetic field H (zero-field cooling procedure). (b) Smooth flux penetration in the Nb at $T = 5$ K and $\mu_0 H = 4.8$ mT. (c) Shielding of flux avalanches at $T = 2.5$ K and $\mu_0 H = 2.5$ mT. (d) When the magnetic field is increased to $\mu_0 H = 4.8$ mT, some avalanches are able to overcome the repulsive force from the interface. (e) Flux avalanches in a 140 nm thick bare Nb film for $\mu_0 H = 4.8$ mT. (f) Weak shielding of flux avalanches for Nb partially covered by 100 nm thick Au, a system where the influence of the normal-metal layer on the superconductor can be compared to that of the mirror of the indicator used in MOI.

a few meters per second, with the receding velocity of the images in the copper, $w_{\mathrm{Cu}} \sim 60$ m/s, estimated from Eq. (4.1) by using for the resistivity $1/\sigma$ the values listed in Ref. [131]. Since $v \ll w$ (low velocity regime), the braking force is small and the repulsion force at the metallic layer border, coming from the asymmetry in the eddy currents, is negligible.

In contrast to that, at low temperatures, the heat generated by the flux motion cannot be efficiently evacuated [26] and a thermomagnetic instability regime appears, giving rise to an abrupt avalanche-like flux penetration moving at velocities $v \sim 10 - 100$ km/s (see Fig. 6 (b) in Ref. [28]). In other words, in this regime where $v \gg w$,

a strong inductive response from the metallic layer is expected. This situation is represented in Fig. 4.2 (c), where the temperature has been decreased to 2.5 K, before applying $\mu_0 H = 2.5$ mT. In this case, the repulsive force at the interface tends to its maximum value and the flux is prevented from entering the region covered by the copper layer. By further increasing the magnetic field up to $\mu_0 H = 4.8$ mT (Fig. 4.2 (d)), the flux first accumulates at the border of the metallic layer and then overcomes the repulsive force of inductive origin, thus penetrating the covered area. The comparison with the flux penetration under the same conditions in a bare Nb film, represented in Fig. 4.2 (e), highlights the efficiency of the copper layer for shielding the central region of the sample. The efficiency of the screening can be evaluated with the parameter R, defined as

$$R = \frac{I_{\text{covered}}}{I_{\text{bare}}}, \tag{4.2}$$

where I_{covered} and I_{bare} correspond to the light intensity in grayscale, averaged over all the pixels lying respectively in the part of the sample covered by the polygonal metallic layer and in the bare superconductor. When the screening is perfect, R should be equal to zero. In Fig. 4.2 (c), the noise and the slight penetration at the borders of the Cu polygon give us a finite but small value $R = 0.10 \pm 0.02$. On the other hand, in the absence of capping layer, as in Fig. 4.2 (e), the ratio is maximum and has a value of 0.80 ± 0.10 for $\mu_0 H = 4.8$ mT, if we consider a fictive polygon covering an area of the same dimensions as in the other samples. The efficient screening we observed in Fig. 4.2 (d) gives $R = 0.35 \pm 0.05$ in the Nb film covered by 500 nm thick Cu, much smaller than the value for the bare Nb. It is interesting to point out here that such a thick Cu layer on top of the superconductor can increase the effective heat removal coefficient. In this case, it has been predicted [132] that the areal size of the avalanches is reduced when compared with an uncovered superconducting film. However, the situation discussed here is somewhat different since avalanches are first triggered from an uncovered rim of the film and only enter later on in a region covered by Cu.

Let us now consider the case where $w \sim v$. Under this condition, the repulsive force at the interface is smaller than for $v \gg w$, and hence the screening power of the metallic layer will be weakened. A way to increase w consists, according to Eq. (4.1), of changing the properties of the metallic layer, either by reducing its thickness or increasing its resistivity. Therefore, we used a 100 nm thick Au layer, having a resistivity between 2 and 8 times bigger than Cu [131]. This gives a corresponding value of $w \sim 3000$ m/s. The magnetic flux distribution for this sample is represented in Fig. 4.2 (f) and shows a weak screening in the area covered by the gold, associated with a ratio $R = 0.61 \pm 0.10$, indeed representing a very weak screening power. We can use this result to comment on the largely assumed non-invasiveness of the MOI

technique. Usually, the mirror deposited on the garnet is made of Al or Au with a typical thickness of 100 nm, similar to the configuration shown in Fig. 4.2 (f). However, unlike in Fig. 4.2 (f) where the metal is in contact with the superconductor, the distance between the mirror in the indicator and the sample surface normally falls in the micrometer range (see section 2.3.5), or at best a few hundreds of nanometers if the garnet is physically pressed against the sample surface. The mirror has therefore a minor effect on the structure of avalanches and triggering conditions. Nevertheless, as already pointed out in the previous chapter, special attention needs to be paid for thick mirrors or superconductors in direct contact with the mirror.

4.2.3 Flux penetration in superconducting films with a step in thickness

As we already pointed out, the maximum screening power of the metallic sheet is obtained in the dynamic regime where $v \gg w$. This was previously illustrated in the Nb-insulator-Cu trilayer invaded by flux avalanches. In this case, the high speed flux propagation does not actually correspond to a train of individual flux quanta, but rather to the propagation of a normal/superconductor interface. The question as to what extent the same behavior is expected for flux quanta keeping their tubular morphology (i.e., at low v) could be tackled by making w as low as possible. Equation (4.1) tells us that this condition can be met by increasing the conductivity of the layer to its upper limit, for instance, by using a superconducting film. The final superconductor-insulator-superconductor trilayer will effectively respond as a single superconducting layer with thickness modulation, represented in Fig. 4.3 (a), as long as the critical temperature of both superconducting layers is the same and the thickness of the insulator remains substantially smaller than the magnetic penetration depth.

The upper row of Fig. 4.3 summarizes the results for a Nb square film covered in the center by a Nb layer, thus forming a central step. The layout is the same as for the Nb films with metallic capping, except for 10 μm long triangular indentations at the middle of the sample's border, aiming to ease the flux penetration at that particular position. This feature will help us to identify the effect of the thickness step on the flux front propagation. Indeed, as clearly evidenced by the magneto-optical images in Fig. 4.3, the indentations act as flux faucets as a consequence of a combined effect of current crowding and the formation of parabolic discontinuity lines [76]. At low fields, when the sample is in the Meissner state, screening currents running around the sample perimeter are forced to circumvent the triangular indentations, leading to an increase of the streamline density at the vertices of the indentation [133–138]. This locally higher current density favors the penetration of flux quanta through this particular point of the structure (see Appendix A for more information).

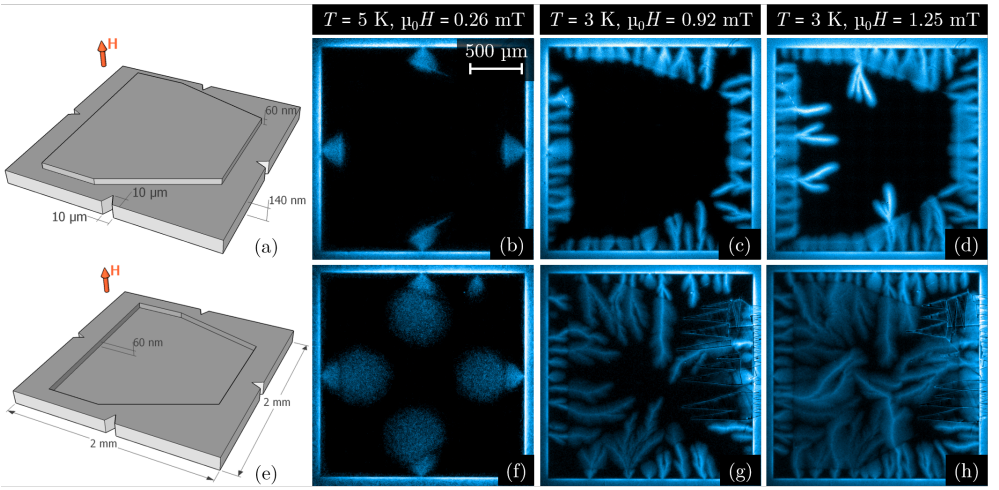

Figure 4.3: **Flux penetration in a superconducting film with a step in thickness.** Panels (a) and (e) show a sketch of the samples layout, consisting of vertically structured Nb thin films with a thicker or thinner center. For the sake of clarity, the illustrations do not respect relative dimension scaling. Magneto-optical images of the magnetic flux penetration into the samples are taken after zero-field cooling procedure. Panels (b-d) correspond to the sample with the thick center, whereas panels (f-h) show the results for the sample with thin center. The second column evidences the smooth flux penetration in the critical state regime at $T = 5$ K. The third and fourth columns show abrupt magnetic flux avalanches at $T = 3$ K for two different applied fields H.

Fig. 4.3 (b) clearly shows that in the smooth flux penetration regime, the parabolic flux penetration is arrested at the border of the step, where the sample thickens from 140 nm to 200 nm, and is guided along this border. This effect, particularly prominent for the tilted borders, has two distinct sources: the penetration barrier at the thickness step, produced by the increase of vortex core energy, and the electromagnetic braking. On the one hand, the thickness step leads to a change in the energy U associated to the vortex cores. The vortex-line energy per unit length ϵ is given by [139]

$$\epsilon = \frac{\phi_0^2}{4\pi\mu_0\lambda^2} \ln\left(\frac{\lambda}{\xi}\right), \tag{4.3}$$

where ϕ_0 is the fundamental flux quantum, λ is the magnetic penetration depth and ξ is the coherence length. Since the core energy $U(y) = \epsilon t(y)$ varies across the thickness step $\Delta t = 60$ nm, there appears a force, F_{core}, pushing the vortex towards the thinner regions of the sample:

$$F_{\text{core}} = -\frac{\partial U}{\partial y} \sim -\frac{\epsilon t(y_2) - \epsilon\left(t(y_2) + \Delta t\right)}{\xi} = \frac{\epsilon \Delta t}{\xi} \approx 375\,\text{pN}. \tag{4.4}$$

We took $\xi \sim 10$ nm, from section 4.2.1, and $\lambda \sim 100$ nm [140], a typical value obtained in samples similar to ours.

On the other hand, the flux deflection can be thought of as an extension of the previously reported results for a Nb film with a Cu layer to the case of very high conductivity ($w = 0$), for which an appreciable transverse force at the interface is expected no matter how slow the flux moves. In other words, for the structure under consideration, the condition $v \gg w$ is always satisfied. Therefore, unlike for the Cu layer, flux deflection is observed also in the smooth field penetration regime (i.e., in the isothermal critical state). Assuming that the vortex field is described by a magnetic monopole with charge $q = 2\mu_0\phi_0$, located at a distance λ below the surface of the superconductor [141], the repulsive force has a maximum close to the step, as shown in Fig. 3.4. The maximum force is given by Eq. (3.3):

$$F_{\text{eddy}} = -\frac{2\mu_0 q^2}{27\pi^2\lambda^2} \approx 2.6\,\text{pN}. \tag{4.5}$$

Note that while this force is significantly smaller than F_{core}, it has a much longer range. Indeed F_{core} acts on vortices located at distances from the step on the order of ξ, while the range of F_{eddy} is on the order of λ (half-width at half maximum).

Figure 4.3 (c) shows that within the regime of abrupt flux penetration at $T = 3$ K, for a field $\mu_0 H = 0.92$ mT, the Nb overlayer, likewise the Cu layer, impedes the flux to enter the region underneath ($R = 0.09 \pm 0.02$). Further increasing the field eventually forces some avalanches to enter into the protected area (Fig. 4.3 (d)), leading to an increased value of $R = 0.32 \pm 0.05$.

We would like to stress that caution must be exerted when thinking of the thick superconducting central area as a perfect conductor. Indeed, there is an additional constant damping force coming from dissipation in the normal cores of the vortices that can never be suppressed, regardless of the velocity. Therefore, as far as damping is concerned, a superconductor shows a different behavior compared to a perfect conductor, since the braking force is always zero in the latter. However, in the case of the deflection of a vortex, considering a perfect conductor or a superconducting capping layer is equivalent, as what matters is the distribution of the eddy/screening currents in the layer. Therefore the repulsive force felt by a vortex approaching the layer is the same in both cases. This is true as long as we are not too close to the step, i.e., at distances $\sim \xi$, where the energy associated with the flux lines dominates over the influence of the eddy currents. Replacing the perfect conductor by a normal metal only decreases the intensity of the repulsive force, accordingly to the eddy currents dependence to conductivity.

For the sake of completeness we have also investigated a sample where the thickness decreases from 140 nm to 80 nm at the central region, represented in the lower row

of Fig. 4.3. This could be considered either as the limiting case of a conducting layer covering the rim of superconductor, or simply as a reduction of the damping in that central area. As evidenced in Fig. 4.3 (f), nothing impedes the flux from invading the central part of the superconductor. In this panel, a non intentional second penetration point can be identified on the top border. This results from a sample imperfection smaller than the nanostructured indentation. We also observe the presence of a dark line in the flux penetration profile, outlining the thickness step. This is caused by the discontinuity in the value of the critical current across the step. In reality, the screening current streamlines - which would otherwise be parallel to the borders of the film - are deformed by the presence of the indentations, and are forced to circumvent them. As a consequence, nearly parabolic discontinuity lines are formed [76], as seen in Fig. 4.3 (f). When the applied magnetic field is increased, the deformation of the streamlines propagates further inside the film. As they encounter the thickness step and the associated decrease of the thickness-dependent critical current [142], a sudden bend of the lines is in order, expressing the fact that their densities are different on both sides of the step. This local change in the current direction is the cause of the discontinuity lines parallel to the step borders, which are clearly seen in Fig. 4.3 (f).

Figure 4.3 (g) shows the avalanche-like flux penetration at $T = 3$ K for $\mu_0 H = 0.92$ mT. As for the smooth penetration, there is no barrier for the flux penetration into the thinner central part. The branches of the avalanches seem to become wider and more blurred in the thinnest region. This effect is caused by the fact that the central region is further away from the indicator used for MOI than the rims of the sample, and therefore the stray field emanating from the avalanches is more spread when reaching the indicator. The large electric fields and the larger traffic of vortices at the border defects should cause the indentations to be preferred nucleation spots for the development of thermomagnetic instabilities [75, 143]. In contrast to that expectation, we do not observe more frequent occurrence of thermal flux avalanches at the indentations, but rather the opposite, as avalanches tend to avoid the indentation. This is also confirmed by a recent experimental report [76] (more information can be found in Appendix A).

In the pioneer work of Wertheimer and Gilchrist [95], it was shown that the speed of flux jumps in Nb decreases with increasing thickness and increasing normal state conductivity. This behaviour was explained in terms of speed limitation by eddy currents. In our study, since the rim of the samples with thinner and thicker center has always the same thickness, the avalanches are triggered with similar velocities. However, since the thickness is increased in the central part of the thick center sample, avalanches tend to decelerate their motion, while for the thin center, the thickness decreases and thus they accelerate. Recently Vestgården and co-authors [144] showed numerically that the threshold field H_{th} needed to trigger avalanches increases linearly

with sample thickness (see Eq. (1.30)). This was also confirmed by experimental studies [145], and avalanches become straighter with fewer and thicker branches. This seems to be in agreement with the experimental observation reported here.

4.3 Time-dependent Ginzburg-Landau simulations

In view of the fact that the reported magneto-optical investigation reflects, in a macroscopic scale, the interaction of vortices with the thickness modulation, it is interesting to review this phenomenon at the individual vortex level. To that end, Dr. Vladimir Gladilin (University of Antwerp) has provided simulations based on the time-dependent Ginzburg-Landau (TDGL) equations for a sample having a polygonal shaped thinner or thicker center, and triangular border indentations, as in the experiments. For the sake of keeping the computation time within reasonable limits, the simulated sample size is scaled down to a $2\,\mu$m $\times 2\,\mu$m square. Similar systems have been addressed numerically in Ref. [146–149]. The coherence length ξ is 16 nm and the (bulk) penetration depth λ is 120 nm. Therefore, the simulations can still be compared with our experimental results, since λ and ξ are much smaller than the sample dimensions.

4.3.1 Basics of time-dependent Ginzburg-Landau simulations

An effectively two-dimensional TDGL equation for the superconducting order parameter ψ, normalized to 1 and averaged over the inhomogeneous thickness $d(x, y)$ of the superconductor, can be written as [150, 151]

$$\left(\frac{\partial}{\partial t} + i\varphi\right)\psi = \frac{1}{d}\left(\nabla_2 - i\mathbf{A}\right) d \left(\nabla_2 - i\mathbf{A}\right)\psi + 2\psi(1 - |\psi|^2). \tag{4.6}$$

Here, φ and $\mathbf{A}$ are respectively the scalar and vector potentials, averaged over the superconductor thickness, and $\nabla_2 = \partial/\partial x\mathbf{e}_x + \partial/\partial y\mathbf{e}_y$. All the relevant quantities are made dimensionless by expressing lengths in units of $\sqrt{2}\xi$, time in units of $\pi\hbar/[4k_{\mathrm{B}}(T_{\mathrm{c}} - T)]$, magnetic field in units of $\phi_0/(4\pi\xi^2) = \mu_0 H_{c2}/2$, current density in units of $\phi_0/[2\sqrt{2}\pi\mu_0\lambda^2\xi]$, and scalar potential in units of $2k_{\mathrm{B}}(T_{\mathrm{c}} - T)/(\pi e)$. Here, $\phi_0 = \pi\hbar/e$ is the magnetic flux quantum, μ_0 is the vacuum permeability, and H_{c2} is the second critical field.

The distribution of the scalar potential φ is determined from the condition $\nabla\cdot\mathbf{j} = 0$, which reflects the continuity of currents in the superconductor. The total current

density $\mathbf{j}$ is given by the sum of the normal and superconducting components:

$$\mathbf{j} = \mathbf{j}_{\mathrm{n}} + \mathbf{j}_{\mathrm{s}}, \tag{4.7}$$

$$\mathbf{j}_{\mathrm{n}} = -\frac{\sigma}{2}\left(\nabla\varphi + \frac{\partial \mathbf{A}}{\partial t}\right), \tag{4.8}$$

$$\mathbf{j}_{\mathrm{s}} = \mathrm{Im}\left(\psi^{*}\nabla\psi\right) - \mathbf{A}|\psi|^{2}, \tag{4.9}$$

where σ is the normal-state conductivity, taken as $\sigma = 1/12$ in our units [152]. For a superconductor with varying thickness, the aforementioned condition of current continuity can be expressed [150] in a 2D form:

$$\frac{\sigma}{2}\nabla_2(d\nabla_2\varphi) = \nabla_2(\mathbf{j}_{\mathrm{s}}d). \tag{4.10}$$

The averaged vector potential $\mathbf{A}$ that enters in Eq. (4.6) can be represented as

$$\mathbf{A} = \mathbf{A}_{\mathrm{e}} + \mathbf{A}_{\mathrm{s}}. \tag{4.11}$$

Here the contribution $\mathbf{A}_{\mathrm{e}}$ corresponds to the externally applied magnetic field $\mathbf{B}_0$, while $\mathbf{A}_{\mathrm{s}}$ describes the averaged magnetic field, which is induced in the superconductor by the currents, given by Eq. (4.7) to (4.9). For a superconducting layer with inhomogeneous thickness, the latter contribution takes the form

$$\mathbf{A}_{\mathrm{s}}(\mathbf{r}_2, t) = \frac{1}{2\pi\kappa^2}\int \mathrm{d}\mathbf{r}_2' K(\mathbf{r}_2, \mathbf{r}_2') d(\mathbf{r}_2')\mathbf{j}(\mathbf{r}_2', t), \tag{4.12}$$

where $\kappa = \lambda/\xi$ is the Ginzburg-Landau parameter and $\mathbf{r}_2 = x\mathbf{e}_x + y\mathbf{e}_y$ is the in-plane radius vector. The time-independent symmetric kernel

$$\begin{aligned} K(\mathbf{r}_2, \mathbf{r}_2') \quad &= F\left(d(\mathbf{r}_2), d(\mathbf{r}_2'), |\mathbf{r}_2 - \mathbf{r}_2'|\right) \\ &+F\left(d(\mathbf{r}_2'), d(\mathbf{r}_2), |\mathbf{r}_2 - \mathbf{r}_2'|\right) \end{aligned} \tag{4.13}$$

is expressed through the function

$$\begin{aligned} F(d, d', D) = \frac{1}{d}\Bigg\{\ln\left(\frac{R(d, D)}{R(d'-d, D)}\right) + \frac{1}{2d'}\Big[\, R(0, D) \\ +R(d'-d, D) - R(d', D) - R(-d, D)\,\Big]\Bigg\} \end{aligned} \tag{4.14}$$

with

$$R\,(d, D) = d + \sqrt{d^2 + D^2}. \tag{4.15}$$

Equation (4.6) with the scalar and vector potentials defined by Eq. (4.10) to (4.12) and the superconductor-insulator boundary conditions, which assure zero values for both the superconducting and normal components of the current across the boundary, is solved numerically using the approach described in Ref. [[147, 153, 154]].

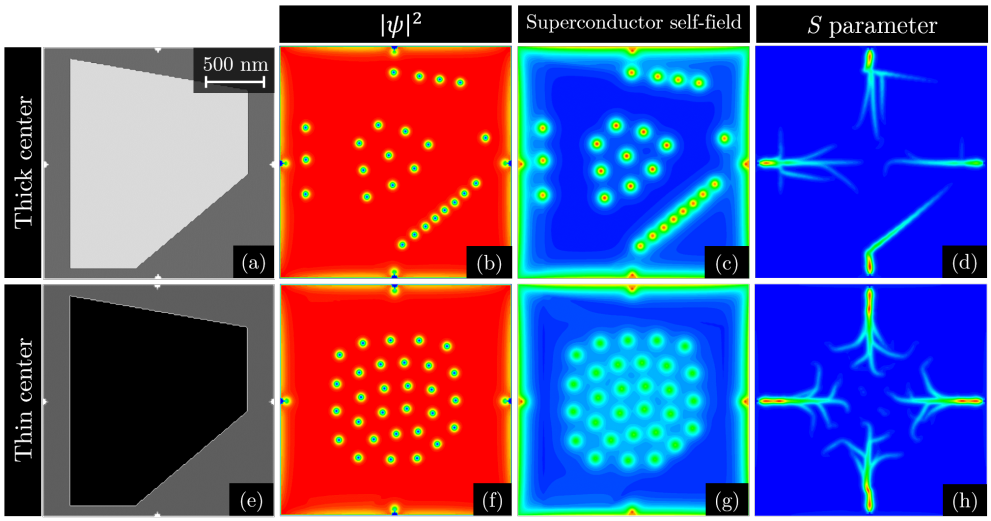

Figure 4.4: **Time-dependent Ginzburg-Landau simulations on a superconducting film with a step in thickness.** Results of the time-dependent Ginzburg-Landau simulations on a $2 \times 2\,\mu\text{m}^2$ Nb film with a step in thickness, from 140 nm in the peripheral region to 200 nm (upper row) or 80 nm (lower row) in the central region. For each of the plotted quantities, blue, green, and red correspond respectively to low, intermediate, and high values. The first column shows the thickness distribution of the superconductor. The second column displays the squared modulus of the superconducting order parameter $|\psi|^2$ once the system reached a (meta)stable state. The third column is the mapping of the superconductor self-field in the reached (meta)stable state. The last column illustrates the S parameter, representing the trace of the vortex trajectories on the time interval from switching on the field until reaching a stable vortex configuration.

4.3.2 Results of the simulations

The results of the simulations are shown in Fig. 4.4. For all quantities represented in the images, red (blue) corresponds to the highest (lowest) values, while green is associated to intermediate values. The first column shows the thickness distribution in the sample: the outer part is 140 nm thick, while the central part is 200 nm thick

(Fig. 4.4 (a)) or 80 nm (Fig. 4.4 (e)). We start with a vortex-free state at zero magnetic field, then a field of $0.06H_{c2}$ is applied, so that penetration of vortices is initiated. The simulations continue until a (meta)stable vortex state is reached. The second column (Fig. 4.4 (b) and (f)) shows the squared superconducting order parameter $|\psi|^2$ whereas the third column (Fig. 4.4 (c) and (g)) corresponds to the self-field in the (meta)stable state. The upper images evidence the fact that the step at the thick-center acts as a barrier for the incoming vortices, while nothing impedes vortex motion towards the center in the thin-center sample. The last column (Fig. 4.4 (d) and (h)) represents the trajectories of the vortices captured by the parameter $S(x, y)$, which is defined [155] as the root mean square of the rate of changes in the local Cooper pair density:

$$S(x,y) = \sqrt{\frac{1}{t_2 - t_1}\int_{t_1}^{t_2} \mathrm{d}t \left(\frac{\partial|\psi(x,y)|^2}{\partial t}\right)^2}, \tag{4.16}$$

where t is the time variable and $t_2 - t_1$ is the time integration interval. The parameter S in a given point (x, y) strongly increases when this point is passed by a moving vortex core. Figures 4.4(d) and (h) demonstrate that the indentations at the superconductor edges act as flux taps and favor the penetration of vortices, as also clearly evidenced in our experimental results shown in Fig. 4.3. Interestingly, the branching of trajectories observed in the experiments is also featured in the simulations, as the S parameter shows that vortices take different trajectories when they cross the thickness step, leading to the formation of several paths for flux penetration. It is worth emphasizing that the physics of individual vortices substantially differs from that of flux avalanches, and therefore particular care has to be exerted when drawing analogies between them.

4.4 Conclusion

In summary, we have used MOI to characterize the effect of a conductive layer on the magnetic flux propagation in a superconductor, for the smooth penetration as well as for the thermomagnetic instabilities regime. Magnetic flux moving at a velocity v in the vicinity of a conductor induces eddy currents, which in turn generate (i) a force repelling the flux from the border of the conductor, due the asymmetry of the current distribution there, and (ii) a braking force slowing down the flux propagation inside the conductor. When $v \gg w = 2/\mu_0\sigma d$, as in the Nb film partially covered by 500 nm thick copper, magneto-optical images show the clear deflection of flux avalanches, since the repulsive force is nearly maximal in this regime. However, when the Nb is covered by 100 nm thick gold, $v \sim w$ and the repulsive force is strongly weakened, leading to weak shielding of the flux from the central part. These measurements show that MOI can be considered as a non invasive technique as long as the distance between the indicator

mirror and the sample surface lies in the micrometer range. In all cases, the metallic layer is inefficient to shield the flux in the smooth penetration regime, where $v \ll w$. A way to keep a maximum repulsive force, even in the low velocities regime, is to replace the metallic layer by a superconductor ($w \approx 0$). This situation has been approached using Nb films with a central step in thickness. The repulsive force is present at all flux velocities in the thick center samples, unlike in normal metals. However, in contrast to perfect conductors, there is a constant braking force in superconductors coming from the dissipation in the normal vortex cores, as well as a repulsive force in the vicinity of the border, coming from the vortex core energy. As expected, samples with a thin center area do not impede the flux penetration, but rather feature some blurring of the flux front in the central part. Time-dependent Ginzburg-Landau simulations performed for a smaller sample reproduce the features we highlighted experimentally, including the deflection and the branching of flux trajectories at the thickness step in the thick center sample.

Chapter 5

Imprinting superconducting vortex footsteps in a magnetic layer

This chapter is largely based on the following work:

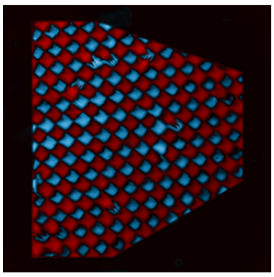

"Imprinting superconducting vortex footsteps in a magnetic layer"

J. Brisbois, M. Motta, J. I. Avila, G. Shaw, T. Devillers, N. M. Dempsey, S. K. P. Veerapandian, P. Colson, B. Vanderheyden, P. Vanderbemden, W. A. Ortiz, N. D. Nguyen, R. B. G. Kramer, and A. V. Silhanek.

Scientific Reports **6**, 27159 (2016).

Popular summary

In this chapter, we investigate a system composed by a magnetic material placed on top of a superconducting film. The interaction between the vortices and the magnetic layer gives rises to a plethora of phenomena, depending on which layer dominates the structure. On the one hand, if the ferromagnetic layer is thick, it provides a very flexible way to control magnetic flux motion in the superconductor, since it can be tuned to guide the vortices in a particular direction or to block their progression towards the sample center. On the other hand, when the ferromagnetic layer is thin, its magnetization can be easily modified by the vortex magnetic field.

Based on this consideration, we adapted the principle of the magic drawing board toy and built up a microscopic magnetic board, by combining a superconductor and a magnetic layer. Everybody already got the chance to practice his/her drawing skills on a magic drawing board: with the help of a pen, containing a small magnet attracting the board's iron fillings, the user can draw lines or more complex shapes. In our hybrid structures, the superconductor hosts vortices, acting as tiny magnetic pens, and the thin layer of magnetic material plays the role of the magic board. In this way, we are capable of recording traces of only a few millionths of meter. Hence, the magnetic imprint of the superconductor could be observed at more than 290°C above the temperature at which the superconductivity disappears. Our findings provide a powerful, though appealingly simple, tool to visualize and track the footsteps of the rather elusive magnetic flux in superconductors. This is particularly interesting when the sample cannot be seen from outside the cryostat: the imprints of the flux distribution of the superconductor can be observed at room temperature and *a posteriori*, using any field-sensitive technique available, such as magnetic force microscopy or scanning Hall probe microscopy. Moreover, the sample can be reused for an unlimited number of experiments, since the imprints can be easily erased very much like in a magnetic drawing board toy.

Finally, the magnetic layer can also record traces of other magnetic field sources than vortices, even at room temperature. For instance, a chessboard pattern, designed in a magnet with regions alternating up and down magnetic moments, was pressed against the magnetic layer and left a clear imprint. This provides an easy and versatile way to tune at will the pinning landscape for vortices, once the structure is cooled to low temperatures. We exploited this system to guide the flux penetration in the superconducting film and found that vortices tend to follow the features of the imprinted chessboard pattern.

5.1 Introduction

Quantum magnetic flux units in type-II superconductors can be regarded as small solenoids, producing localized magnetic field variations extending over distances of 2λ perpendicularly to the applied field, where λ is the magnetic penetration depth. These flux lines interact with inhomogeneities *inside* the superconducting material, leading to a plethora of well-known pinning mechanisms. Furthermore, the static and dynamic response of individual vortices can also be modified if their stray field *outside* the superconducting volume is altered. This is precisely the reason why multilayered hybrid systems combining superconducting and non-superconducting materials have been an active field of research in the last decade.

We have seen in the previous chapters that the stray field of an isolated moving vortex can induce eddy currents in a nearby conductive layer, leading to a velocity dependent damping force [92, 121]. This effect can be exploited to provide better stability and quench protection in superconducting cables by reducing the speed of flux jumps [86, 156]. More spectacular is the possible use of the monopolar magnetic field emanating from a vortex as submicron-sized magnetic tweezers to locally polarize spin carriers in a diluted magnetic semiconductor [157]. Among these hybrid devices, the heterostructures combining superconductivity and magnetism, two antagonistic quantum macroscopic states, arguably represent the most investigated systems so far [158–161].

A simple attempt to classify the superconductor (S-layer) - ferromagnet (F-layer) hybrids, where the F-layer and the S-layer are in close proximity and interact only through their stray fields, consists of comparing the relative field strength scales of each subsystem. Indeed, if the coercive field H_{coe} of the ferromagnetic layer is much larger than the upper critical field H_{c2} of the superconducting layer, changing the magnetic landscape in the S-layer will have no major effect on the F-layer. In contrast to that, modifications in the F-layer can lead to profound changes in the response of the S-layer. This effect has been successfully implemented to obtain fluxonic elemental devices such as tunable pinning centres and vortex rectifiers [162–164]. In the opposite case where $H_{\mathrm{coe}} \lesssim H_{c2}$, i.e., combining a hard type-II superconductor and a soft magnetic material, it has been shown that magnetic domains in the F-layer shrink compared to their size without the superconducting layer [165–167] and that vortex-antivortex lattices can be spontaneously induced [168, 169] when cooling down in zero applied field below the superconducting critical temperature T_{c}.

A particularly interesting phenomenon, previously evoked to explain the increase of pinning in Nb with ferromagnetic Gd inclusions, is the possibility to locally polarize a ferromagnetic material by the stray field of a single vortex [170]. If this were indeed feasible, we could imagine a single vortex as a tiny magnetic scriber, leaving on the

magnetic material a clear imprint consisting of locally polarized magnetic moments. It is precisely this possibility of using vortices as magnetic tweezers that we experimentally investigate in this chapter via the magneto-optical imaging (MOI) technique. Our hybrid system consists of a superconducting Nb film separated from a permalloy (Py) film by a thin insulating SiO_2 layer. The Py layer only covers partially the Nb film, thus allowing us to compare the behaviour of flux penetration in the Nb layer without and with a soft magnet on top. We demonstrate that regardless of the Py thickness, a net in-plane polarization of the F-layer introduces an asymmetry on the flux penetration in the Nb layer. This magnetic landscape also influences the much faster flux motion in thermomagnetic instabilities. Thick Py layers show reorientable stripe domains that can guide the flux motion as reported by Vlasko-Vlasov *et al.* [171]. For thin Py layers without stripe domains, we observe that the flux in the superconductor leaves clear imprints on the Py layer. This effect is particularly prominent for vortex avalanches. Our findings extend recent reports on YBCO/CoFeB bilayers by Stahl *et al.* [172], where mapping of the supercurrent flow on the magnetic layer is shown. Given the fact that the Curie temperature of Py is much higher than the critical temperature of the superconductor, the footsteps left by vortices on the Py layer can survive up to room temperature, thus allowing for *ex situ* analysis as in magnetic decoration techniques. This is further confirmed by imprinting a hard magnetic template into the Py layers at room temperature. The resulting tailored pinning landscape is subsequently exploited to guide vortex motion at low temperatures.

5.2 Characterization of the superconductor-ferromagnet hybrids

In this section, we review the fabrication of the superconductor-ferromagnet structures, consisting of a Nb film partially covered by a Py layer. We then describe the magnetic properties of the Py layers. The superconducting properties of the Nb films were already detailed in section 4.2.1.

5.2.1 Fabrication of the Nb/Py hybrid structures

The investigated hybrid system, represented in Fig. 5.1, is composed of a Py ($Fe_{19}Ni_{81}$) polygonal-shaped layer (F) of three different thicknesses t = 50 nm, 100 nm and 460 nm, deposited on top of a 140 nm thick Nb film (S) of 2×2 mm^2. A 5 nm thick SiO_2 film was deposited between the S and F layers to ensure electrical insulation between them, and thus reduced proximity effects. In other words, the mutual interaction between the S and F layers is purely of magnetic origin and occurs through their respective stray fields.

The 140 nm thick Nb films covered by a 5 nm thick SiO_2 layer were prepared in a home-built electron beam UHV evaporator. The Py layers were deposited in an Alliance Concept rf/dc sputtering machine. The base pressure in the introduction chamber was 10^{-7} mbar. To improve the sticking of the Py on top of the SiO_2, a 3 nm thick Ta buffer layer was first deposited using dc-sputtering with the following parameters: power of 40 W, 20 sccm argon flux and 1.3 Å/s deposition rate at 100 mm distance. The permalloy layer is composed of 81% Ni and 19% Fe and was deposited with 20 W power and 20 sccm argon flux. The sputtering of the 50 nm thick (460 nm thick) Py was done at a distance of 100 mm (50 mm) with a rate of 1.3 Å/s (5.2 Å/s). The magnetic anisotropy in the Py layer comes from the magnetron field. The RMS roughness of the Py films is 0.83 ± 0.16 nm in a $10 \times 10\,\mu m^2$ area.

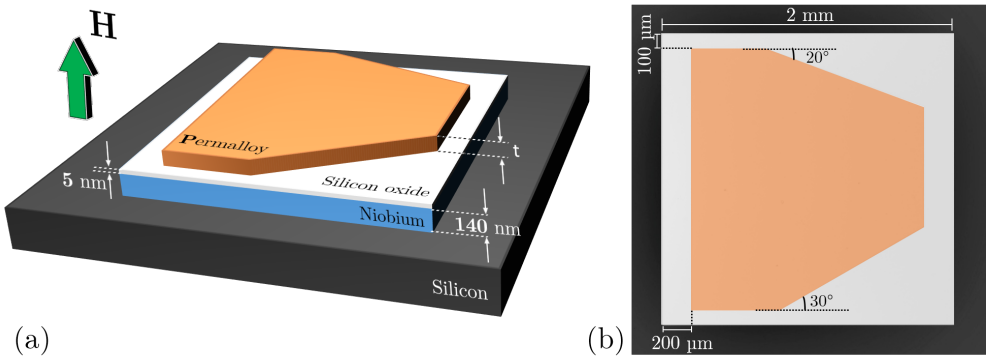

Figure 5.1: **Superconductor-ferromagnet hybrid structure layout.** (a) Schematic representation of the sample layout. For the magneto-optical images, a magnetic field H is applied perpendicularly to the plane of the sample. Three thicknesses t of the Py layer were investigated: 50 nm, 100 nm, and 460 nm. Panel (b) shows an artificially colored top-view optical image of one of the samples.

The polygonal shape of the Py layer aims to explore different angles of penetration of the magnetic flux entering through the sides of the Nb square. In addition, the fact that the Py does not cover the Nb borders allows flux avalanches to develop freely. Magnetization measurements presented in section 4.2.1 reveal a superconducting transition $T_c = 9$ K and show that flux avalanches of thermomagnetic origin develop below 4.5 K. The flux penetration in the Nb layer is rather smooth above this temperature, where it can be properly described by the isothermal Bean model. Direct visualization of the magnetic flux landscape was obtained by MOI.

5.2.2 Magnetic properties of the Py layer

Let us first dig into the magnetic behavior of soft magnetic alloys of the type Fe-Ni, known as permalloy. These compounds are characterized by a weak uniaxial anisotropy energy K, implying a broad domain wall size $\delta = \pi\sqrt{A/K}$, where A is the exchange constant, proportional to the coupling between neighbouring spins. Broad domain walls are relatively easy to displace and therefore, the magnetization loops of these materials exhibit a rather small irreversibility. Ni-rich permalloy compounds, as the one used in this work, have a perpendicular anisotropy that dominates over shape anisotropy imposed by the thin film geometry above a critical thickness $t_c \sim 200$ nm [173–178]. Increasing the film thickness above t_c leads to out-of-plane up and down stripe domains separated by a Bloch-type domain wall [179–181]. It has been shown [182] that the domain structure for thicknesses smaller than t_c corresponds to large domains with antiparallel in-plane magnetization separated by broad Néel or cross-tie domain walls. More recently, however, Uspenskaya *et al.* [183] have reported that Py deposited on top of a Nb film thicker than 100 nm, as in our experiments, can exhibit Bloch head-to-head domain walls, which the authors attribute to the roughness-induced anisotropy.

Figure 5.2 summarizes the most interesting results of the magnetic characterization of these hybrid samples, relying on SQUID magnetometry and magnetic force microscopy (MFM). Magnetization measurements were obtained in a Quantum Design SQUID magnetometer. MFM images were acquired in a Multimode AFM system (Digital Instruments Nanoscope III - VEECO) in interleave tapping mode (scan lift of 20 nm) with a SSS-MFMR probe from NANOSENSORS, magnetized with an external magnet. Since the 50 nm thick and the 100 nm thick Py samples exhibit very similar behavior, we will only focus on the two extreme thicknesses in the remainder of this chapter. Panels (a) and (c) show out-of-plane magnetization loops at 10 K for an external field H applied perpendicularly to the sample. The remanent magnetization $M_{\rm rem} \approx 0.08$ MA/m in the 50 nm thick Py is significantly larger than in the 460 nm thick Py layer, where $M_{\rm rem} \approx 0.025$ MA/m. However, $M_{\rm rem}$ can be erased in both samples by applying a rather small field $\mu_0 H_{\rm coe}^{\perp} \approx 5$ mT. The $M(H)$ loops show little change at 300 K, with analogous values for the characteristic fields.

In agreement with previous reports [179], MFM images at room temperature show no magnetic contrast for Py films thinner than 100 nm (Fig. 5.2 (b)). The thicker Py layer exhibits a stripe domain structure (Fig. 5.2 (d)) which can be readily oriented with an in-plane magnetic field of a few mT. The stripes have a width $w \approx 280$ nm. The contrasting magnetic landscapes observed in the thin and the thick Py layers give rise to remarkable and non-trivial differences in the flux penetration, that will be addressed in the following sections.

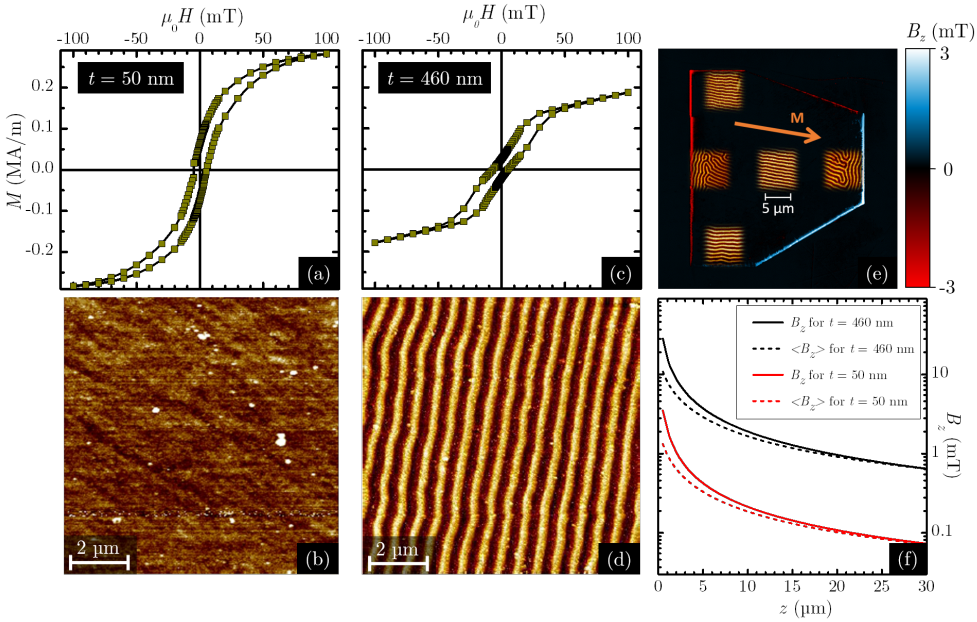

Figure 5.2: **Magnetic characterization of the Py layers.** Out-of-plane magnetization M as a function of the external magnetic field H, applied perpendicularly to the plane of the sample at 10 K for a Py layer of (a) 50 nm, and (c) 460 nm. Panels (b) and (d) show MFM images obtained at room temperature for the 50 nm and 460 nm thick Py layers, respectively. (e) Magneto-optical image of the stray field arising from the macroscopic in-plane magnetic moment (orange arrow) in the polarized 460 nm thick Py layer. The insets show MFM images of the magnetic domains at various positions on the Py. (f) Numerical simulations show the decay of the magnetic field B_z at the border of the Py layer as a function of the vertical distance z from the top surface of Py (solid lines). The calculations give values of $M_{\mathrm{rem}}^{\parallel} \sim 0.08$ MA/m, based on the experimental mean magnetic field picked up by MOI, i.e., the average of the field $\langle B_z \rangle$ over the indicator active layer thickness $d = 3\,\mu$m (dashed lines).

The observed magnetic history of the Py layers leads us to adopt a clear measurement protocol. Starting from a temperature $T = 10$ K just above the superconducting transition, we then applied an in-plane magnetic field to clearly define the direction of the stripe domains as those illustrated in Fig. 5.2 (d). This procedure not only orients the stripe domains, but also induces a macroscopic in-plane magnetic moment. Indeed, Fig. 5.2 (e) shows a magneto-optical image of the 460 nm thick Py layer at 10 K after magnetizing it along the direction indicated by the orange arrow. The blue-white and red stripes outlining the borders of the Py correspond to B_z, the component of the stray field perpendicular to the sample plane. White indicates a stray field in the same direction as the applied field (i.e., positive field) and red indicates a stray field antiparallel to the applied field (i.e., negative field). Complementary MFM

images obtained at remanence and over different places of the Py layer are also shown in Fig. 5.2 (e). Interestingly, the stripe domains align mostly parallel to the previously applied in-plane field everywhere in the Py layer, except at distances of about 5 μm from the borders perpendicular to the magnetization. Measurements of the in-plane magnetization show a saturation magnetization $M_{\rm sat}^{\parallel} \approx 0.9$ MA/m. In contrast to the case of perpendicular saturation magnetization, $M_{\rm sat}^{\parallel}$ can be reached by applying small in-plane fields of around 15 mT for the thick Py, and 2 mT for the thin Py layer. However, fields around 3 mT (1 mT) were enough to change the direction of the in-plane magnetization in the thick (thin) Py.

Quantitative MOI allows us to estimate the mean out-of-plane component of the magnetic stray field B_z at the extremes of the Py layer. Since B_z decays as the distance z measured from the top of the Py surface increases, each slice of the magneto-optical indicator gives a different contribution to the magneto-optical signal. Therefore, the experimentally picked up signal, shown in Fig. 5.2 (e), corresponds to the average z-component of the stray field in the indicator:

$$\langle B_z(z)\rangle = \frac{1}{d}\int_z^{z+d} B_z(z')dz', \tag{5.1}$$

where $d = 3\,\mu$m is the thickness of the indicator. From Fig. 5.2 (e), we found $\langle B_z(z)\rangle \approx 2.9 \pm 0.2$ mT (0.35 ± 0.2 mT) at 10 K in the thick (thin) Py layer for a typical gap between the sample and the indicator of $z \sim 5\,\mu$m. It is then possible to calculate the remanent magnetization $M_{\rm rem}^{\parallel}$ of the magnetic layer, based on the measured $\langle B_z(z)\rangle$. To that end, numerical calculations using the COMSOL Multiphysics software were performed by Dr. J. Avila, for Py layers respecting exactly the same dimensions as the investigated samples. They are based on the following equation:

$$B_z(\mathbf{r}) = \frac{\mu_0}{4\pi}\int_S \frac{(z-z')\,\hat{n}\cdot\mathbf{M}_{\rm rem}}{\mid \mathbf{r}-\mathbf{r}' \mid^{3/2}}\,dS', \tag{5.2}$$

where S is the total surface of the magnetic layer and $\hat{n}$ is the unit vector perpendicular to the surface. Combined with Eq. (5.1), Eq. (5.2) links $M_{\rm rem}^{\parallel}$ with $\langle B_z(z)\rangle$. Using the experimental values for $\langle B_z(z)\rangle$ and z, we find $M_{\rm rem}^{\parallel} \approx 0.21$ MA/m (0.22 MA/m) for the thick (thin) Py layer. The decay of $B_z(z)$ (solid lines) and $\langle B_z(z)\rangle$ (dashed lines) with increasing z is shown in Fig. 5.2 (f) for the 460 nm thick Py (black) and for the 50 nm thick Py (red) and were found to be very similar to the analytical solution valid for a parallelepiped magnetic layer, given by Eq. (2.32). Note that we considered a constant in-plane magnetization all over the Py layer, while in reality, as appears clearly in Fig. 5.2 (e), the magnetization may change direction close to the borders to reduce the stray field, thus leading us to underestimate $M_{\rm rem}^{\parallel}$.

The simulations suggest that the stray magnetic field at the Nb layer will reach

much higher values than those detected by the indicator. Indeed, Fig. 5.2 (f) shows that B_z is above 10 mT (1 mT for the thin Py) at the surface of the Py layer, which corresponds also to the field at the top surface of the superconductor. Note that the stray field polarity in the superconductor is reversed compared to the one detected by the magneto-optical indicator, as it is indicated in the sketch of Fig. 5.3 (a). The question now arises as to whether the magnetic charge and the associated stray field is large enough to induce vortices of opposite polarities at the extremes of the Py layer. Milošević and Peeters [184] have addressed this problem within the London formalism and they have shown that the number of vortices induced by the stray field depends on the ratio between the in-plane magnetization M and $M_0 = 4\pi\phi_0\lambda/\mu_0 \sim 1$ MA/m for Nb at zero temperature. The high values of $M^{\parallel}_{\mathrm{rem}}$ we calculated guarantee the creation of vortices at the extremes of the Py layer. Moreover, values of B_z at the superconductor surface are much higher than the typical values for the first vortex penetration.

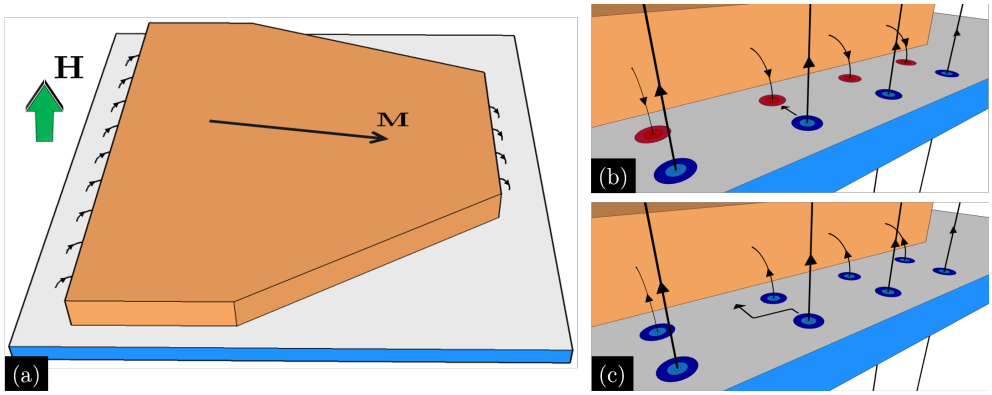

Figure 5.3: **Interaction between vortices created by the Py layer and the applied field.** (a) Sketch representing the stray field induced by the Py layer in the superconductor. When cooling down below T_c, stray field flux lines are trapped in the Nb film and (b) antivortices (colored in red) and (c) vortices (in blue) are generated at the Py borders perpendicular to the in-plane magnetization. In (b), the antivortices attract and annihilate entering vortices created by the applied field, while in (c), both types of vortices interact repulsively.

5.3 Flux penetration in Nb/Py hybrid structures

As the magnetic properties of the Py layers are strongly dependent of the thickness, the experimental results obtained by MOI are presented separately for the thick and thin Py layers.

5.3.1 Anisotropic flux penetration in a thick Py layer

Having identified the magnetic landscape imposed by the Py layer, we are now in a position to explore its influence on the flux penetration in the underlying superconducting layer. Figure 5.4 summarizes the most salient results for the hybrid system with a 460 nm thick Py layer, for two nearly perpendicular directions of in-plane polarization, as shown in panels (a) and (e). The first column images (panels (a) and (e) in Fig. 5.4) were obtained at $T = 10$ K $> T_c$ in the remanent state. Subsequently, the sample was cooled down to 6 K and the out-of-plane magnetic field was increased in steps of 0.1 mT. Figure 5.4 (b) corresponds to $\mu_0 H = 2.4$ mT and Fig. 5.4 (f) corresponds to $\mu_0 H = 1$ mT. Under these zero-field cooling conditions, the flux penetrates from the borders of the superconductor and the flux front progresses smoothly until it reaches the border of the Py layer, indicated by a yellow dashed line. Increasing H further leads to a distinctive field penetration into the region covered by the Py layer. Indeed, firstly, the flux front progression is arrested at the side of the Py layer generating a negative field in the Nb layer (top side in (b), right side in (f)), whereas it easily crosses the Py border that creates a positive field in the Nb layer (bottom side in (b), left side in (f)).

This behavior can be explained by the fact that antivortices (vortices) are created at the white (red) border of the Py layer as illustrated in Fig. 5.3 (b) and (c). Indeed, incoming vortices first annihilate with antivortices before moving further into the area covered by the magnetic layer (top side in Fig. 5.4 (b), right side in (f)), as shown in Fig. 5.3 (b). The antivortices at the Py border therefore act as attractive pinning centres for the vortices. On the contrary, vortices entering from the side where the Py layer induces vortices of the same polarity (Fig. 5.3 (c)), find just a permeable wall of repulsive centers created by the vortices generated by the Py layer, thus not impeding the flux penetration beneath it (bottom side in Fig. 5.4 (b), left side in (f)). As expected, when a negative field H is applied, the sides of the Py layer where the flux penetration is eased or delayed are inverted. Once the flux is pushed inside, it is guided by the stripe domains, giving rise to clear finger like magnetic structures, resembling those reported by Vlasko-Vlasov *et al.* [171]. It is interesting to note that a somewhat similar asymmetry in the flux penetration has been discussed by Vodolazov *et al.* [185] in micrometer scale structures. In addition, at the sides perpendicular to the in-plane magnetic moment of the Py layer (i.e., left and right borders in (b), upper and lower borders in (f)), field penetration is also delayed. This can be explained by the strong reduction of the vortex mobility perpendicular to the stripe domains [186, 187]. Although similar features in the highly anisotropic field penetration are observed in panels (b) and (f), the effect is less prominent in (b) due to the particular geometrical shape of the Py layer. Indeed, firstly the distance between the Py layer and the Nb

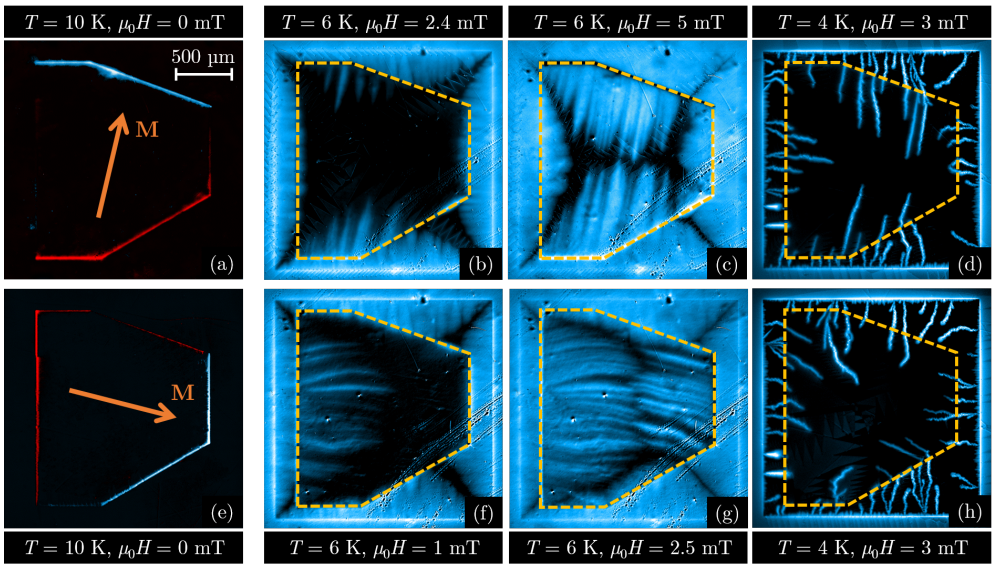

Figure 5.4: **Highly anisotropic flux penetration into a Nb film covered with a 460 nm thick Py layer.** Magneto-optical images of a Nb film with a thick (460 nm) Py layer after applying an in-plane field of 10 mT along a direction close to the vertical (upper row) and horizontal (lower row) axes. First column: images obtained at $T = 10$ K $> T_c$. The white (red) rims evidence the positive (negative) stray field at the borders of the Py layer. Second and third column: images obtained at $T = 6$ K in the smooth flux penetration regime, for an applied field pointing out of the images, (b) $\mu_0 H = 2.4$ mT, (c) $\mu_0 H = 5$ mT, (f) $\mu_0 H = 1$ mT, (g) $\mu_0 H = 2.5$ mT. Last column: images taken at $T = 4$ K and $\mu_0 H = 3$ mT in the thermomagnetic instabilities regime.

border where the penetration occurs is twice smaller in (b) compared to (f). Secondly, the angle between the Py and the Nb borders is larger for the bottom side of the sample than for the top side, thus increasing the distance that flux has to cover before reaching the Py border.

Further increasing the field (panels (c) and (g)) better reveals the underlying configuration of the magnetic domains, as evidenced by the morphology of the flux penetration. It is interesting to note that the stripe domains in the Py layer do not only act as channels for the smooth and isothermal flux penetration occurring at high temperatures, but also influence the dynamics of flux avalanches of thermomagnetic origin at low temperatures. This is shown in panels (d) and (h) obtained at $T = 4$ K after applying $\mu_0 H = 3$ mT. Smaller avalanches are prevented from penetrating into the Py layer, resulting in some flux accumulating at the interface. The avalanches entering the Py tend to align with the direction of the magnetic domains, resulting in a bending of their trajectories at the interface, in order to follow the easiest path

towards the center of the Py. Moreover, the magnetic field on top of the avalanches is weaker compared to the bare Nb film. This effect is attributed to the high magnetic permeability of the Py layer which, as in μ-metal screening sheets, favors the diffusion of magnetic field inside the Py.

5.3.2 Imprinting vortex footsteps in a thin Py layer

In the previous section, we have shown that the magnetic landscape produced by a thick Py layer shapes the flux penetration in the superconductor. Attempting to revert this scenario, so that the superconducting flux rules over the magnetic template, can be achieved by reducing the volume of the magnet in such a way to decrease its associated magnetic energy.

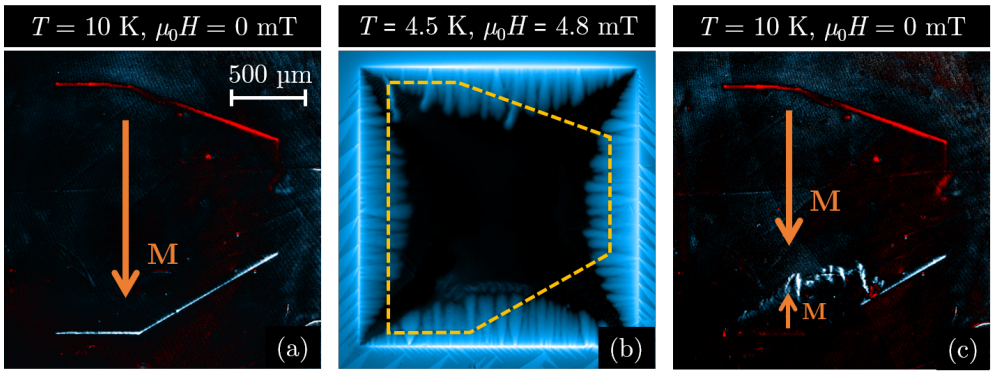

Figure 5.5: **In-plane magnetization reversal induced by smooth flux penetration in the Nb film.** Magneto-optical images of a Nb film with a thin (50 nm) Py layer, after applying an in-plane field of 10 mT along a direction close to the vertical axis. (a) Image at $T = 10$ K $> T_c$. The white (red) rims evidence the positive (negative) stray field at the borders of the Py layer. (b) Image obtained at $T = 4.5$ K in the smooth flux penetration regime for an applied field pointing out of the image, $\mu_0 H = 4.8$ mT. After obtaining image (b), the temperature is increased to $T = 10$ K and $\mu_0 H = 0$ mT, resulting in the image in panel (c). Panel (c) shows clear reversal of the in-plane magnetization induced by the flux penetration.

Figure 5.5 (a) shows a magneto-optical image of the thin Py layer after applying an in-plane field of 10 mT at $T = 10$ K $> T_c$. As pointed out previously, the net in-plane magnetic moment of the thin film is about 6 times weaker than for the 460 nm thick Py layer. Panel (b) shows the smooth flux penetration in the superconductor at $T = 4.5$ K for $\mu_0 H = 4.8$ mT. As expected from the radically different magnetic domain landscape featured in the MFM images in Fig. 5.2, there is no flux guiding inside the thin Py layer, in sharp contrast to the behavior observed in the thick Py layer. Moreover, due to the weaker value of B_z estimated from Fig. 5.2 (f), the

asymmetry in the flux penetration in the thin Py is less pronounced, although a slight delay for the vortex entrance can still be observed at the white Py side, populated by antivortices. There is no noticeable influence on the flux penetration at the borders perpendicular to the in-plane magnetization.

Strikingly, when the temperature is increased up to 10 K and H is subsequently decreased to zero (Fig. 5.5 (c)), we observe that the smooth flux penetration in the Nb layer has left a clear imprint into the Py layer. This imprint corresponds to a reversal of the in-plane magnetic domains as indicated by arrows in Fig. 5.5 (c). Note that the smooth flux penetration leaves no traces at the other borders of the Py layer. In order to account for this effect, we start by reminding that $\mu_0 H_{\rm sat}^{\parallel}$ is smaller than 2 mT, meaning that the magnetic state of the Py layer can be easily switched by an in-plane field [183]. Considering that the flux front advancing in the Nb layer is made of vortices which generate an in-plane magnetic field component at the Py layer, we wonder if that field component is large enough to switch the in-plane magnetic moment. In the case of a single Pearl vortex [20] in Nb, it is easy to calculate [157] that the in-plane field component at a distance $z = 10$ nm from the top surface of the superconductor reaches a maximum value ~ 10 mT at a distance $r \sim \lambda$ from the vortex center and decays as $1/r^2$, producing a significant $B_{\parallel}$ even at a few hundreds of nanometers from the vortex core. This is further confirmed by calculations for thin Nb films similar to ours [21]. We can then safely assume that this in-plane magnetic field will be even reinforced by the joint contributions of the vortices located in the vicinity of the superconducting flux front in our sample. This discussion leads us to conclude that $B_{\parallel}$ at the flux front is strong enough to flip locally the magnetic moment of the Py layer. This argument naturally explains why the flux penetration does not leave imprints at the other borders of the Py layer where $B_{\parallel}$ is either in the same direction or perpendicular to the original magnetic moment orientation.

Figure 5.6 summarizes the results obtained for a 50 nm thick Py layer. The first column (panels (a) and (e)) corresponds to the magneto-optical images recorded above $T_{\rm c}$ and showing the stray field of the thin Py layer, estimated around 0.35 mT in the indicator. The second column of Fig. 5.6 shows the smooth flux penetration occurring at 6 K for $\mu_0 H = 5$ mT (panel (b)) and $\mu_0 H = 4.5$ mT (panel (f)). In sharp contrast to the highly anisotropic flux penetration observed for the thick Py layer, now the flux front morphology is very similar to an uncovered Nb film. As we discussed above (see Fig. 5.2 (b)), for this sample, there are no domains with out-of-plane magnetization to impede or guide the motion of vortices.

At lower temperatures, within the thermomagnetic instability regime, flux avalanches undergo a deflection of their trajectories when penetrating the area covered by the Py layer (Fig. 5.6 (c) and (g)). Similar behaviour has been observed in superconductor/metal hybrid systems, studied in the previous chapters, and attributed to the

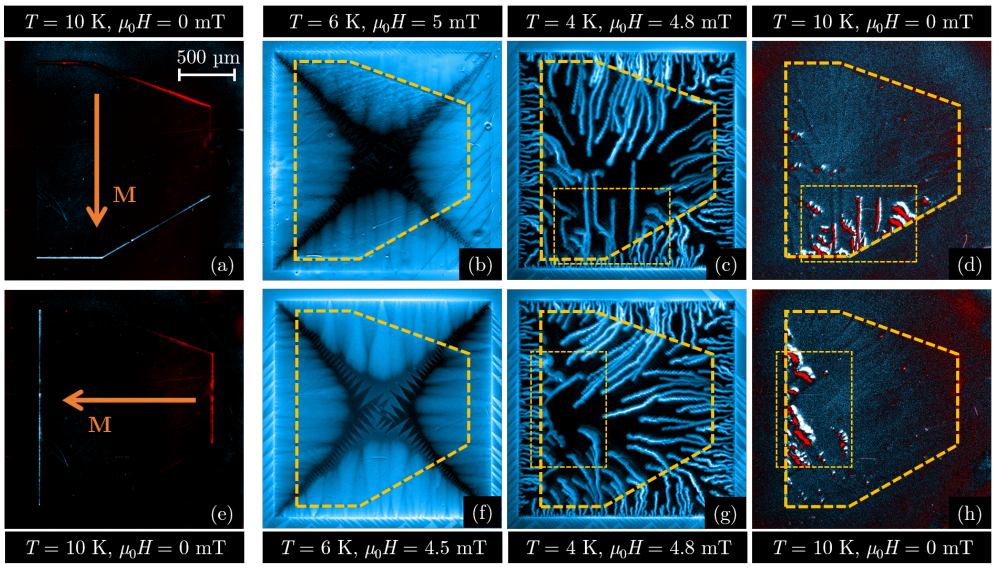

Figure 5.6: **Interaction between a 50 nm thick Py layer and a Nb film.** Magneto-optical images of the Nb film with a 50 nm thick Py layer on top, after applying an in-plane field of 10 mT close to the vertical (upper row) and horizontal (lower row) directions. First column: images obtained at $T = 10$ K $> T_c$. The white (red) rims evidence the positive (negative) stray field at the borders of the Py layer. Second column: images obtained at $T = 6$ K in the smooth flux penetration regime, for an applied field pointing out of the images, (b) $\mu_0 H = 5$ mT and (f) $\mu_0 H = 4.5$ mT. Third column: images corresponding to $T = 4$ K and $\mu_0 H = 4.8$ mT in the abrupt flux penetration regime, where flux avalanches of thermomagnetic origin are observed. Last column: images obtained at $T = 10$ K $> T_c$ and $\mu_0 H = 0$, starting from the state in the third column. The remanent state of the Py layer shows clear imprints of flux avalanches. The yellow dashed rectangles mark the area studied more carefully in Fig. 5.7.

eddy currents induced in the thick metallic layer. However, in the present case, the thickness of the Py layer is too small to induce avalanche deflection and therefore another deflection mechanism needs to be invoked. Likely the source of this deflection has a magnetic origin, since avalanches tend to align with the magnetization direction. The cause of the observed preferential direction for the avalanche propagation lies on the energy needed to switch the in-plane magnetic moment. Indeed, avalanches propagating parallel to the in-plane magnetic moment do not induce in-plane **M** flipping, whereas avalanches propagating antiparallel to the in-plane moment are damped by the energy they spent in inducing in-plane **M** flipping. A closer inspection to Fig. 5.6 (c) and (g) indeed shows that avalanches entering from the red side of the Py tend to advance more easily following the direction of the magnetization, whereas avalanches

entering from the white side penetrate less under the Py layer. The smoking gun evidence for this interpretation comes from the last column of Fig. 5.6.

Starting from the state presented in the third column of Fig. 5.6, we increased the temperature above T_c and set $\mu_0 H = 0$. We then recorded the resulting magnetic landscape, as shown in Fig. 5.6 (d) and (h). We observe the presence of a clear magnetic signal corresponding to traces left by flux avalanches, but mainly on the side where the flux has been forced to switch the in-plane magnetic moment of the Py layer. These imprints of avalanches were seldom visible in the 460 nm thick permalloy layer, while they were also observed in the 100 nm thick Py. This seems to point at the importance of the magnetic pattern of the Py layer in order to print the magnetic flux, and especially at the crucial role played by interfaces between domains with different in-plane magnetization. These imprints seem to correspond to head-to-head Bloch domain walls pointing up and down, and delimiting interfaces between regions of different **M**, as also observed in Ref. [183].

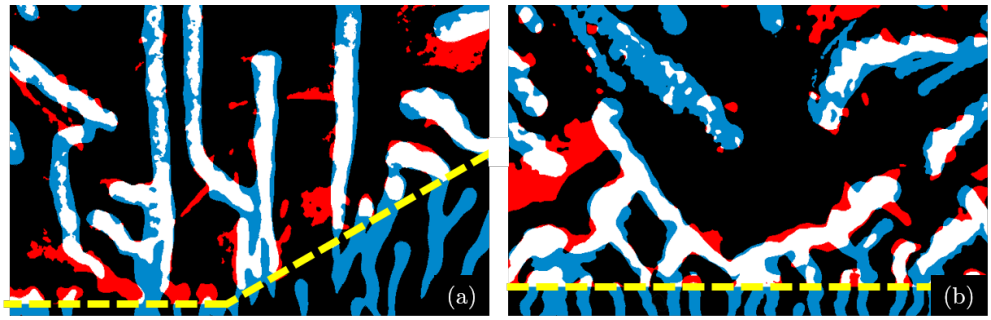

Figure 5.7: **Spatial correlation between flux avalanches and their imprints in the 50 nm thick Py layer.** Binary images of the region marked by a yellow dashed rectangle (a) in Fig. 5.6 (c-d), and (b) in Fig. 5.6 (g-h). The superposition of flux avalanches (in blue) and their negative field imprints (in red) is represented in white.

Even though the signal is stronger on the white side of the Py, weak traces induced by the vortex avalanches can be seen on the whole surface of the magnetic layer. These type of traces are formed by pairs of lines with opposed polarity, as observed in Fig. 5.6 (d) and (h). For a given initial **M**, these traces always respect the same polarity through the whole magnetic layer, i.e., dark stripe on one side of the trace, bright stripe on the other side. This type of magnetic structures are the same as the patterns observed by Uspenskaya *et al.* [183] in similar hybrid structures and are correlated with the direction of **M**. They were identified as Néel domain walls, whose footprints are dark and bright stripes, produced by the local poles appearing at both sides of the in-plane **M** inside the wall.

In order to highlight the correlation between the flux avalanches and their imprints

in the magnetic layer, we will now focus on certain particular areas of the sample, marked by a yellow dashed rectangle for each series of measurements shown in Fig. 5.6. Figure 5.7 (a) and (b) shows the superposition of two binary images, where low fields are represented in black and high field are colored. Flux avalanches at 4 K represented in Fig. 5.6 (c) and (g) are painted in blue, while their negative field imprints at 10 K featured in Fig. 5.6 (d) and (h) are in red. The reason for this choice is that, surprisingly, avalanches happen to be spatially strongly correlated to the stripes with stray field opposed to the applied field, as shown by the regions colored in white, where avalanches and their imprints overlap. Strikingly, the imprints in the magnetic layer reveal an excellent correlation with the position of the flux avalanches. Moreover, the magnetic printings left by avalanches could even be maintained and observed up to 300 K, opening the path for a new way to visualize flux avalanches *ex situ*. Indeed, much like magnetic particles highlight the flux pattern in the Bitter decoration technique, the magnetic layer can be used here to record avalanches and observe them at temperatures well over T_c. A recent work on Nb/Al_2O_3/Co structures [188] has shown an improved imprinting of avalanches, as traces could be recorded in the Co layer irrespective of the sample side from where the avalanches originate.

5.3.3 Controlling flux penetration by magnetic patterning of a Py layer

In the remainder of this chapter, we study the room temperature imprinting of a hard ferromagnetic sample in the thick and thin Py layers to shed light on their different behavior under these conditions. We then investigate the influence of the imprinted pattern on the flux penetration in Nb/Py structures at low temperatures.

5.3.3.1 Room temperature imprinting of thermomagnetically patterned NdFeB ferromagnets in Py layers

Recently, a promising technique, thermomagnetic patterning (TMP), has been developed to produce magnetic fields spatially modulated in the range from tens to hundreds of microns. In this technique, the magnetization of a hard ferromagnetic film is initially saturated in one direction. The film is then irradiated by a pulsed laser through a mask, while an external field is applied, in the direction opposite to the magnetization of the film. The applied field must be weaker than the room temperature coercive field of the film. Regions exposed to the irradiation are heated up, resulting in local reduction of coercivity and hence reversal of the magnetization in these regions. The final structure consists of an array of micromagnets with opposite magnetization. Further details about the technique can be found in Ref. [189]. Patterning of a few microns thick NdFeB hard magnetic films has been achieved using this technique, that can

be used to produce a variety of configurations of micromagnets, such as chessboard, stripes, and periodic arrays of circular/square domains, to name a few.

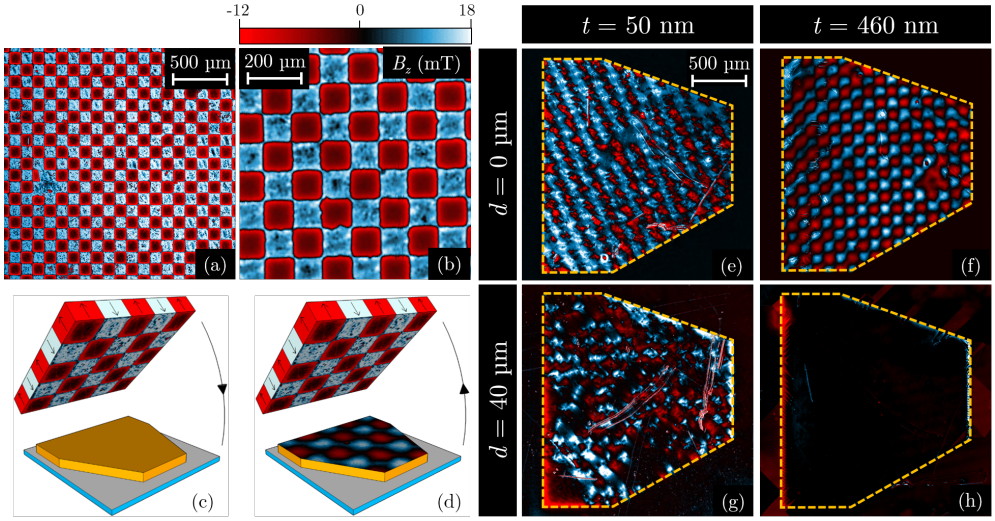

Figure 5.8: **Room temperature imprinting of an inhomogeneous magnetic landscape in the Py layers.** (a) Magneto-optical and (b) SHPM images of a NdFeB magnetic pattern with $100 \times 100\,\mu\text{m}^2$ domains alternating up (white) and down (red) magnetization. This pattern is then (c) laid upside down against the Py layer and (d) removed from the Py, leaving an imprint of the magnetic template in the magnetic layer. Images in (e) and (f) show that this procedure is efficient to print the magnetic pattern in the 50 nm thick Py as well as in the 460 nm thick. When a $40\,\mu$m pergamine sheet is inserted between the magnetic pattern and the Py during the transfer, the printing is still observed in the thin Py film, while it is completely absent in the thick layer (panels (g) and (h)).

The 3 μm thick NdFeB film we exploited consists of a chessboard pattern of $100 \times 100\,\mu\text{m}^2$ squares with alternate opposite magnetization. It has been deposited by high rate triode sputtering on a thermally oxidized 100 mm Si wafer covered by a 100 nm thick buffer layer of Ta. A capping layer of 100 nm thick Ta was also deposited on top of the NdFeB to avoid oxidation. The coercive field is around 1.9 T at 300 K and the magnetization was locally reversed by heating over a thickness of 1.2 μm. The relatively large size of the patterned magnetic domains in NdFeB can be revealed by MOI. Figure 5.8 (a) shows a magneto-optical image of the sample obtained at room temperature. Further information can be obtained from scanning Hall probe microscopy (SHPM) measurements performed at room temperature. A Hall probe with $5 \times 5\,\mu\text{m}^2$ active area was used for the measurements. The scan resolution is $2.5\,\mu$m. Further details on the SHPM setup can be found in Ref. [190]. Figure 5.8 (b) shows a SHPM image of the sample obtained at the closest scan height $z \sim 4$ μm, in

the range of the typical heights z_{MOI} in MOI experiments. From both the magneto-optical and SHPM images, it is clear that the magnetic landscape inside the two sets of squares in the pattern are distinct from each other. While the red squares in the SHPM image appear quite smooth, the blue squares look rather coarse in comparison. This is a result of the TMP process, as magnetization reversal by the laser, occurring in the red squares, leads to smoothing of the coarse magnetic profile of the as-grown sample.

In order to unambiguously demonstrate that imprinting of an inhomogeneous magnetic field landscape is possible in the thin Py layer, even at room temperature, we use this hard ferromagnetic NdFeB film with a chessboard pattern. According to the SHPM measurements, at the distance $z \sim 4\,\mu$m at which the scanning was performed, the magnetic field B_z is as high as 18 mT. Therefore, the maximum magnetic field in the vicinity of the sample surface is expected to reach values of several hundreds of mT.

Before all imprintings, the magnetic history of the Py layers was first erased by applying an in-plane magnetic field of 20 mT. In practice, the imprinting of the chessboard pattern was obtained by approaching the NdFeB sample upside down on the Py layer as schematically shown in Fig. 5.8 (c). The chessboard pattern was then removed (Fig. 5.8 (d)), leaving an imprint that was observed by MOI. The resulting imprints after the Py layer and the NdFeB have been in contact ($d = 0\,\mu$m) are shown in Fig. 5.8 (e) and (f) for the 50 nm thick and 460 nm thick Py layers, respectively. In both cases, the imprints of the chessboard pattern are very clear. This may seem in contradiction with the low temperature results for the thick Py layer, where we could not record flux avalanches. However, it should be stressed that the magnetic field generated by the NdFeB pattern is several times larger than the field of an avalanche, which is roughly a few dozens of mT [191]. Therefore, the field is high enough to change the microscopic domain distribution inside the thick Py layer, leading to domains with significant out-of-plane remanent magnetization.

If we repeat the printing process, but now inserting a 40 μm thick piece of pergamine paper between the Py layer and the NdFeB chessboard pattern, we obtain the images shown in Fig. 5.8 (g) and (h). Strikingly, the magnetic imprint is completely absent from the 460 nm thick Py layer, while it is still visible in the 50 nm thick Py. This clearly pinpoints to the main difference in the behavior of the two Py layers with respect to magnetic imprinting: high out-of-plane fields are necessary to leave a mark in the thick Py, where domains with out-of-plane magnetization exist, whereas weak in-plane fields are sufficient to imprint magnetic patterns in the thin Py, by flipping the in-plane magnetization locally.

5.3.3.2 Magnetic flux penetration in a magnetically patterned Nb/Py structure

Since changing the thick Py layer magnetization requires relatively large magnetic fields, it can be magnetically patterned and then used to guide the flux penetration in the underlying superconducting layer. The imprinting process starts from a state where the Py layer is magnetized in-plane along the direction indicated by the orange arrow in the magneto-optical image of Fig. 5.9 (a). With the help of the patterned NdFeB film, two different magnetic configurations are generated in the Py layer, as shown in Fig. 5.9 (b) and (c). The chessboard pattern is approximately aligned (panel (b)) and at $\sim 45°$ (panel (c)) with respect to the long border of the Py layer.

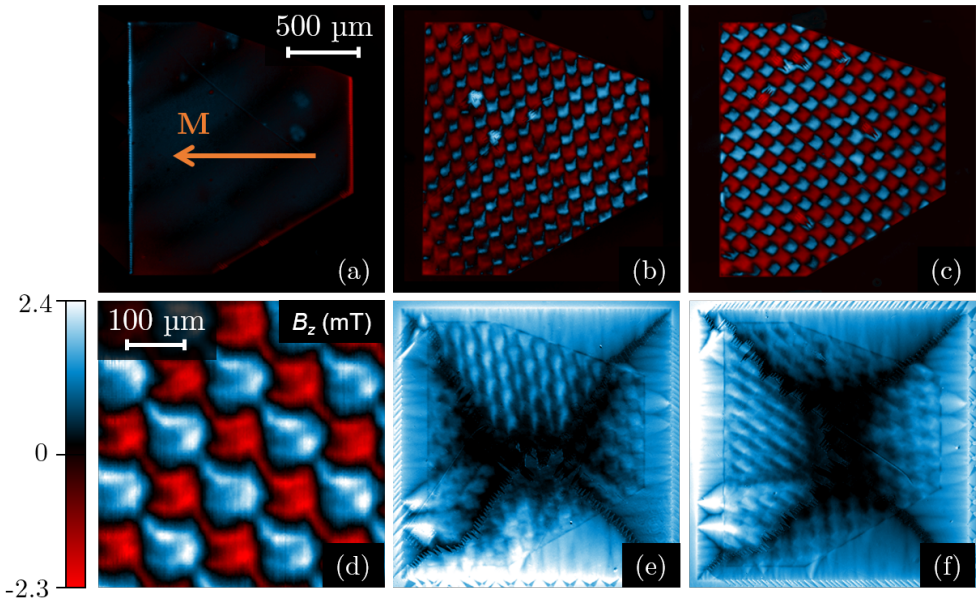

Figure 5.9: **Magnetic flux penetration in a magnetically patterned Nb/Py structure.** (a) Nb/Py sample magnetized in-plane, with the magnetization direction indicated by the orange arrow. The TMP NdFeB sample with chessboard pattern is imprinted in the Py layer along two directions, with respect to the long Py border: (b) approximately aligned with the border and (c) at $\sim 45°$. (d) SHPM image at room temperature showing a part of the imprinted Py layer, obtained at a scan height $z \sim 4\,\mu$m. Panels (e) and (f) show magneto-optical images of the smooth flux penetration at 6 K in the Nb/Py sample, with the imprinted patterns shown in (b) and (c), respectively. These images are obtained by subtracting the image at $\mu_0 H = 0$ mT in each set, to remove the signal from the magnetic pattern. After zero-field cooling, the magnetic field H was increased to (e) $\mu_0 H = 4.9$ mT, and (f) $\mu_0 H = 5.9$ mT.

In order to expose the small scale details of the imprinted magnetic landscape, the Py layer has been characterized using SHPM performed at room temperature. The

SHPM image in Fig. 5.9 (d) shows the chessboard pattern in the Py obtained at the closest scan height $z \sim 4\,\mu$m. The magnetic field B_z varies by 5 mT, which is ~ 6 times less than in the NdFeB film (see Fig. 5.8 (b)). This is consistent with the fact that Py is a much softer ferromagnetic material than NdFeB.

The flux penetration is observed by cooling the sample down to 6 K in zero field. Figure 5.9 (e) shows a magneto-optical image of the flux penetration in the configuration of panel (b), for an applied field $\mu_0 H = 4.9$ mT. The corresponding image for the configuration of panel (c) is shown in panel (f) for $\mu_0 H = 5.9$ mT. Both images are obtained by subtracting the image at $\mu_0 H = 0$ mT to remove the signal from the magnetic pattern.

These images allow us to clearly establish the modulation of the flux path in the Nb by the magnetic pattern. This is evidenced by the staircase-like paths of flux flow, following the chessboard pattern of the Py layer. Furthermore, similar to our observations in section 5.3.1, flux motion is observed to be asymmetric with respect to the different edges of Py. Flux guided by the chessboard pattern penetrates much quickly from one border of the Py layer with respect to the others (top border in Fig. 5.9 (e) and left border in Fig. 5.9 (f)). This indicates that the underlying in-plane magnetization might still play a significant role even after imprinting the out-of-plane magnetic pattern in Py. A preliminary investigation of the flux jumps in this system shows that large dendritic avalanches develop at low temperatures and present the same tendency to follow a staircase-like pattern.

5.4 Conclusion

In summary, we have experimentally demonstrated the possibility to visualize *ex situ* both smooth and abrupt magnetic flux penetration in a Nb film, by depositing a thin Py layer on top. The imprints left by the flux seem to be made of Bloch type domain walls, separating head-to-head in-plane magnetic domains. We show that flux avalanches progress less when they are forced to invert the polarization of the Py layer as compared to the case where no magnetization switching occurs. We attribute this effect to the work needed to revert the polarization orientation, but other possible damping mechanisms should be considered, as for instance the generation of magnons [192] or the fact that vortex avalanches may be limited by the much slower Walker velocity of propagation of magnetic domain walls [193]. The undeniable appeal of the technique lies in its simplicity and the possibility to explore high T_c superconductors. We expect to trigger further experimental and theoretical studies to discover new magnetic compounds optimizing the resolution of the technique down to single vortex imprints.

The method introduced here is actually not limited to thin Py layers, although

much larger fields are needed to leave imprints in thick Py layers. In addition, thick Py layers tend to severely modify the flux propagation in the superconducting film and the technique could therefore no longer be considered as non invasive. This effect can however be exploited to guide vortices, which tend to follow the magnetic pinning landscape imposed by imprinting a magnetic template in the thick Py layer. To that end, the field distribution generated by thermomagnetically patterned micromagnets was successfully imprinted in the Py at room temperature. The flux penetration in the Nb film at low temperatures was found to be strongly affected by the imprinted pattern, providing a flexible and efficient way to guide flux motion.

Conclusion and perspectives

In this thesis, we envisaged the possibility to reduce dissipation in superconductors by increasing the damping of the vortex motion. This approach relies on the fact that the stray field of a vortex can interact with materials placed outside the superconductor. We exploited the versatility of superconducting hybrid structures, made of a superconducting film combined with a capping layer, to explore different mechanisms of vortex damping, that we evidenced with the help of the magneto-optical imaging technique.

Magnetic flux moving in the vicinity of a conductor induces eddy currents, which in turn generate (i) a braking force slowing down the flux propagation inside the conductor, and (ii) a force repelling the flux from the border of the conductor, due to the asymmetry of the current distribution there. Using a classical analogy, describing the vortex as a magnetic monopole, we were able to explain the shielding and deflection of avalanches by a metallic layer as well as the unaffected flux penetration at low velocities. Our measurements shed some light on the invasiveness of the magneto-optical imaging technique, when the metallic mirror of the indicator is placed at submicrometer distances from the sample surface. From a stand point of fluxonics devices, it is interesting to highlight the fact that metallic capping layers become active elements only at high vortex speeds. Therefore, by patterning the metallic layer, the mean vortex displacement direction can be affected progressively as vortex velocity increases. This approach can be thought of as introducing an anisotropic damping constant $\eta(x, y)$ imposed by the predefined design of the patterned metallic layer. Since the repulsive force coming from the border of the conductor increases with its electric conductivity, we explored the situation where the metallic capping layer is replaced by a superconductor, in superconducting films with a step in thickness. We observe shielding in the thick central region for all flux velocities, further enhanced by the increase in the vortex core energy at the interface, not taken into account in our model. Since avalanches are made of millions of vortices, qualitative predictions on the deflection angle are out of reach of the classical description we proposed, working at the single vortex level. Therefore, further theoretical developments should focus

on the impact of the interaction between vortices, which might give rise to collective phenomena not accounted for in our model.

Interesting phenomena also arise in superconducting-ferromagnetic hybrid structures, where a superconducting film is partially covered by a ferromagnetic layer. In this system, flux motion in the superconductor is strongly dependent on the stray field and the magnetization domains structure of the ferromagnet. In all cases, flux penetration is asymmetric and guided by the magnetic structure, an effect that is more prominent as the ferromagnetic layer grows thicker. The impact of vortex motion is nonetheless more visible on a thin ferromagnetic layer, where the small in-plane magnetic field of a vortex is sufficient to flip the in-plane magnetization. In this situation, vortex trajectories can be imprinted in the magnetic layer, both in the avalanche and smooth flux penetration regimes, to be observed above the critical temperature of the superconductor, even up to room temperature. Recent results have shown that this effect is quite general and has been seen in other magnetic materials [188]. However, further studies are still required to optimize the resolution of this new technique meant to observe *ex situ* the flux distribution in a superconductor. For instance, by a careful choice of the magnetic compound and the layer thickness, it might be possible to enhance the spatial resolution to visualize single vortex imprints. Concerning the increased damping produced by a magnetic layer, it would be interesting to separate the contribution emanating from repolarization of the local magnetic moments from other effects such as eddy currents or magnons generation [192]. The former effect could be isolated by using non-conducting magnetic materials or tunable multiferroic systems, allowing to adjust the magnetic irreversibility by an external voltage source. Moreover, we illustrated the possibility to tune the magnetic pinning landscape at will by imprinting a hard ferromagnetic template with high out-of-plane magnetic field in a thick ferromagnetic layer. This flexible procedure offers a versatile way to shield or guide the flux penetration at low temperatures, according to the desired pattern, and might be further explored to enhance fluxonic devices.

Although we provided a first experimental analysis of damping phenomena in micropatterned superconducting films, further experimental and theoretical efforts are needed to understand the influence of metal and ferromagnetic damping on the generation of phase slips, ultrafast vortex displacements, and vortex instabilities. Structures made of a superconducting film and a diluted magnetic semiconductor, i.e., a semiconductor doped with magnetic impurities, might constitute an interesting step to undertake in future investigations. Indeed, this system combines both electromagnetic and magnetic damping mechanisms explored in this thesis and offers the possibility to use the stray field of vortices as magnetic tweezers, to form spin clouds in the semiconductor and control them. Moreover, the Curie temperature of these materials might be tuned to see the impact of the irreversibility of the hysteresis loop on the

damping mechanism. While theoretical studies have addressed this problem [157], an experimental realization of these structures remains to be demonstrated.

Further advances are also conditioned by the enhancement of the experimental setup for magneto-optical imaging. The sensitivity and the spatial resolution of the technique would benefit from a reduction of undesirable depolarization of the light beam occurring in the microscope and the cryostat. Considering our particular system, this can namely be achieved by using thinner cryostat windows, to reduce the depolarization, or by upgrading the optics with Glan-Thompson polarizers, increasing substantially the initial polarized/unpolarized light intensity ratio. Another option to consider consists in replacing the mercury lamp by a more powerful light source, such as LED or laser, to enhance significantly the signal picked-up by the CCD camera.

Appendix A

Flux penetration in samples with border defects

In this appendix, largely based on Ref. [76], we review the influence of defects in the border of a superconducting film on the magnetic flux penetration. After detailing the sample fabrication and layout, we describe the effect of a lithographically defined indentation at the sample edge on the smooth flux penetration following the Bean model and in the flux avalanches regime.

A.1 Samples fabrication and layout

The superconducting samples are 100 nm thick Nb films prepared in a home-built electron beam UHV evaporator. The base pressure before evaporating the film was 2×10^{-10} Torr and reached 2.5×10^{-8} Torr during the evaporation. The film was evaporated at a rate of 0.1 nm/s on a silicon substrate which was at room temperature (28°C before and 45°C after the process). The structures were patterned using a Zeiss scanning electron microscope equipped with Raith patterning generator. The mask was a 270 nm thick PMMA single layer resist (AR-P 679.04). After development of the resist, a 50 nm thick aluminum mask was evaporated in a Plassys electron beam evaporator. After lift-off of the aluminum film the niobium film was dry etched by a reactive ion etch (2 min with SF6 gas). Finally the remaining Al on top of the Nb structures was removed with a basic solution (Megaposit MF 26A Developer).

The layout of some of the investigated samples is represented in Fig. A.1. Several rectangular samples of 400 μm $\times$ 800 μm size evaporated on the same substrate were measured at the same time. Performing simultaneous measurements guarantees the same magnetic field H and temperature T for all samples, thus allowing a reliable

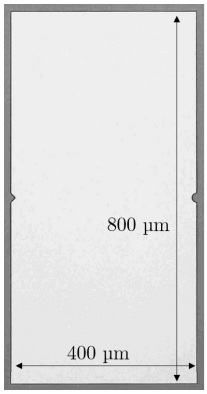

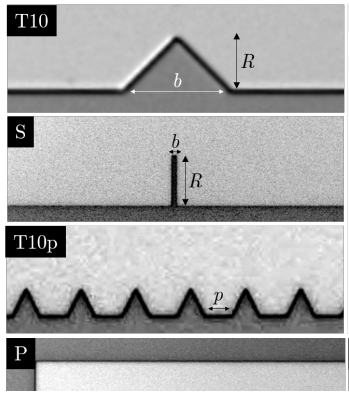

TAG	SHAPE	SIZE	PERIOD
T10		$R = 10$ µm $b = 20$ µm	∞
S		$R = 10$ µm $b = 1$ µm	∞
T10p50		$R = 10$ µm $b = 10$ µm	$p = 50$ µm
T10p100		$R = 10$ µm $b = 10$ µm	$p = 100$ µm
P	plain film with smooth borders		
R	films with rough borders		

Figure A.1: **Layout of the Nb films with artificial edge defects.** On the left, an optical microscopy image shows the dimensions (400 μm × 800 μm) and the position of the artificial defects on the longest side for one of the Nb films. We study here 2 shapes of defects: triangular (T) and rectangular (S). The corresponding panels show optical images of these indentations with the relevant distances reported in the table on the right side. The influence of the defect periodicity, as illustrated in panel T10p, is studied for the triangular defect, where periods of 50 μm and 100 μm are considered. In addition to the films with smooth borders of rugosity smaller than 0.2 μm (P), we also consider the same samples with rough borders of rugosity 0.8 μm (R).

comparison between them. The indentations were introduced along the longest sides of the rectangular films. Single indentations were located at the mid-point of the longest side. We studied two different motifs here: triangular (T) and rectangular slit (S), as shown in the optical images of Fig. A.1. Moreover, for the 10 μm-size triangular indentation, we investigated different separations between neighboring defects: 100 μm and 50 μm separation. The tags referring to each individual case are listed in the table of Fig. A.1. In addition to the previous samples, characterized by a roughness with a standard deviation of 0.03 μm, we have repeated the same set of samples, but now with an artificial roughness of 0.1 μm standard deviation along the long sides of the rectangular samples.

A.2 Influence of border defects on the flux penetration

The fact that the current streamlines running parallel to the sample border must abruptly circumvent a defect encountered in their path gives rise to so-called discontinuity lines (d lines). Along these lines, the external magnetic field is efficiently screened by the sharp bending of the current [194], leaving clear imprints visible in the flux profile as local minima in the magnetic flux landscape. This is illustrated in the

magneto-optical image in Fig. A.2, showing the flux penetration in the vicinity of the T10 indentation. The d lines approximately take a parabolic shape, highlighted by the white dashed line. It is noteworthy that independently of the shape of the indentation, the d lines take the following asymptotic form far from the defect, for $y \gg R$:

$$y \simeq \frac{x^2}{2R}, \tag{A.1}$$

where R is the height of the defect.

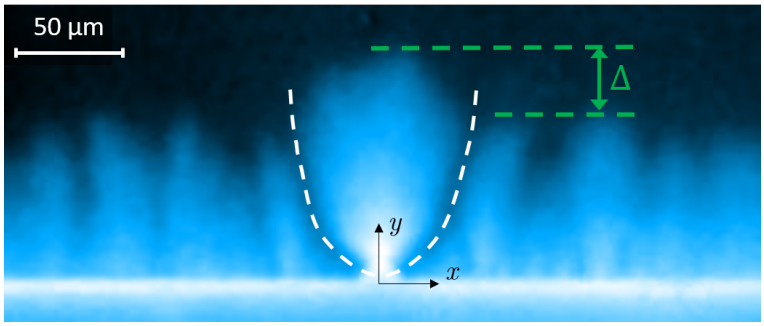

Figure A.2: **Smooth flux penetration at a triangular border defect.** Magneto-optical image of the magnetic flux in a Nb film with a triangular (T10) border indentation at 3.6 K. The defect produces an excess flux penetration over a distance Δ compared to flux front at the smooth border. The d lines marking the local minima in the flux distribution are highlighted by the white dashed line.

An additional consequence of border defects is that flux penetrates deeper into the sample, by an amount Δ, as compared to the penetration without indentations [137]. Even at the smooth border, the penetration of the magnetic flux is inhomogeneous and leads to an irregular flux front. This may be caused by uncontrolled edge defects of size comparable to $\xi(T) \simeq 15$ nm or local changes in the material properties.

Moreover, due to the large electric fields and the larger traffic of vortices at defects, it is widely believed and repeatedly predicted that indentations should represent preferred nucleation spots for the development of thermomagnetic instabilities. [137, 194, 195] In order to corroborate this hypothesis we performed both field cooling and zero-field cooling experiments to observe the position of avalanches in the Nb film with a periodic row of indentations (T10p100 and T10p50) as well as in the T10 and S sample borders.

In Fig. A.3 (a), we show the flux penetration in a sample with optimum borders after zero-field cooling at 3.6 K and applied field $\mu_0 H = 2$ mT. In this sample, the top defect is S and the bottom corresponds to T10. No evidence of flux avalanches is observed. However, by applying a magnetic field of 12.5 mT before cooling down to 3.6 K, and subsequently reducing the field to 1 mT, clear avalanches of negative

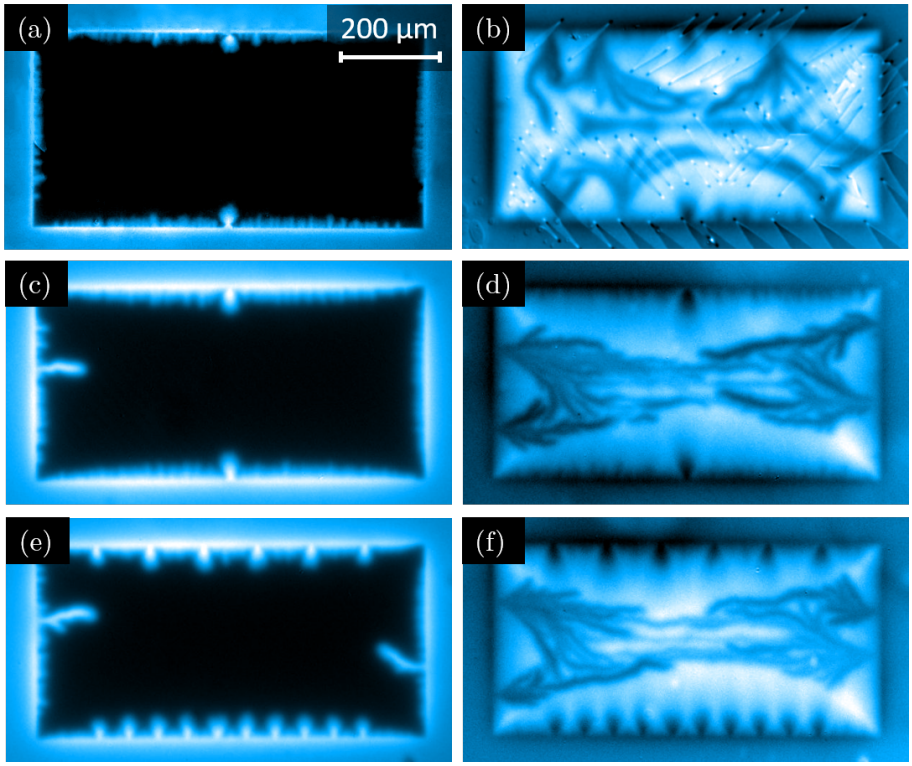

Figure A.3: **Flux avalanches in a superconducting film with edge defects.** Magneto-optical images of the Nb film at 3.6 K show the flux penetration when a 2 mT magnetic field is applied after zero-field cooling (left column) or in a 1 mT field after field in 12.5 mT (right column). In panels (a-d), the samples feature the S (top) and T10 (bottom) indentations, while (e) and (f) show the T10p100 (top) and T10p50 (bottom) indentations. Contrarily to what was predicted in the literature, avalanches are not preferentially triggered at indentations, as they decrease the magnetic pressure, but tend to appear at the smooth borders. The comparison of samples having four smooth sides (first and third lines) with those having rough long-sides (second line) shows the importance of smooth borders to trigger avalanches.

flux (i.e., polarity opposed to the applied field) are observed as shown in Fig. A.3 (b). Note that the thermomagnetic instabilities are not triggered at the indentations, in striking contrast to what was expected.

Panels (c) and (d) of the same figure show a geometry similar to panels (a) and (b), but now the indentations are positioned along rough (R) borders (Fig. A.1), while the short indentation-free borders are smooth (P). In this case, for both zero-field-cooling (Fig. A.3 (c)) and field-cooling (Fig. A.3 (d)), avalanches are triggered at the smooth short side of the sample, not in the vicinity of the indentations. This confirms the fact that smooth borders are more prone to exhibit avalanches than rough borders. Adding more indentations, as shown in Fig. A.3 (e) and (f), does not help to force the

instabilities to be triggered at this electric field hot spots.

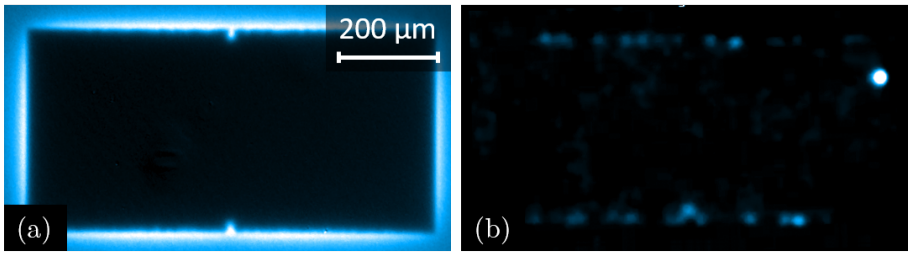

Figure A.4: **Dynamics of the flux penetration in a film with edge defects.** (a) Magneto-optical image of a 100 nm thick Nb film with T10 (top border) and S (bottom border) indentations at 3.6 K in a field $\mu_0 H = 1$ mT. The long edges are rough (R), while the short edges are smooth (P). (b) Difference between the images at $\mu_0 H = 1.01$ mT and 1 mT.

A possible explanation for this surprising result might involve an effective reduction of the critical current density at the indentation as a consequence of the reduction of the surface barrier for vortex entrance, as discussed in Ref. [135]. In simple words, the indentation seems to act as a magnetic flux faucet that helps to release the magnetic pressure at the sample border by enhancing the smooth flux penetration in its vicinity. Since it is essential to drive the system out of equilibrium to trigger an avalanche, Therefore, impurities easing the flux penetration are expected to help the system to relax and prevent the formation of a metastable state far enough from equilibrium to trigger an avalanche. This is clearly visible in Fig A.4, for the sample with T10 and S indentation on long rough borders (R), while short borders are smooth (P) (see also Fig. A.3 (c)). Figure A.4 (a) shows a magneto-optical image of the flux penetration at 3.6 K for an applied field $\mu_0 H = 1$ mT. Panel (b) represents the difference between the image at $\mu_0 H = 1.01$ mT and the image in panel (a). This is useful to highlight changes in the magnetic field distribution. In this image, we see a large amount of small spots where flux changes along the rough border, while the smooth short borders show only one larger spot carrying more flux. This is in agreement with the observation that flux avalanches do not appear at the rough borders, due to efficient flux relaxation.

Bibliography

[1] H. K. Onnes, *The superconductivity of mercury*, Comm. Phys. Lab. Univ. Leiden **122**, 124 (1911).

[2] L. N. Cooper, *Bound electron pairs in a degenerate Fermi gas*, Phys. Rev. **104**, 1189 (1956).

[3] J. Bardeen, L. N. Cooper, and J. R. Schrieffer, *Theory of superconductivity*, Phys. Rev. **108**, 1175 (1957).

[4] W. Meissner and R. Ochsenfeld, *Ein neuer Effekt bei Eintritt der Supraleitfähigkeit*, Naturwissenschaften **21**, 787 (1933).

[5] F. London and H. London, *The electromagnetic equations of the supraconductor*, Proc. Roy. Soc. **A149**, 71 (1935).

[6] A. A. Abrikosov, *Magnetic properties of superconductors of the second group*, Sov. Phys. JETP **5** (1957).

[7] P. G. de Gennes, *Superconductivity of metals and alloys* (Addison-Wesley New York, 1989).

[8] D.-X. Chen, J. J. Moreno, A. Hernando, A. Sanchez, and B.-Z. Li, *Nature of the driving force on an Abrikosov vortex*, Phys. Rev. B **57**, 5059 (1998).

[9] A. A. Abrikosov, *An influence of the size on the critical field for type II superconductors*, Dokl. Akad. Nauk SSSR **86**, 489 (1952).

[10] E. B. Sonin, *Magnus force in superfluids and superconductors*, Phys. Rev. B **55**, 485 (1997).

[11] P. Fulde, L. Pietronero, W. R. Schneider, and S. Strässler, *Problem of Brownian motion in a periodic potential*, Phys. Rev. Lett. **35**, 1776 (1975).

[12] J. Bardeen and M. J. Stephen, *Theory of the motion of vortices in superconductors*, Phys. Rev. **140**, 1197 (1965).

[13] M. Tinkham, *Viscous flow of flux in type-II superconductors*, Phys. Rev. Lett. **13**, 804 (1964).

[14] J. R. Clem, *The Bardeen-Stephen theory*, Journal of Superconductivity **4**, 337 (1991).

[15] H. Suhl, *Inertial mass of a moving fluxoid*, Phys. Rev. Lett. **14**, 226 (1965).

[16] C. P. Bean, *Magnetization of high-field superconductors*, Rev. Mod. Phys. **36**, 31 (1964).

[17] C. P. Bean and J. D. Livingston, *Surface barrier in type-II superconductors*, Phys. Rev. Lett. **12**, 14 (1964).

[18] Y. B. Kim, C. F. Hempstead, and A. R. Strnad, *Magnetization and critical supercurrents*, Phys. Rev. **129**, 528 (1963).

[19] W. A. Fietz, M. R. Beasley, J. Silcox, and W. W. Webb, *Magnetization of superconducting Nb-25% Zr wire*, Phys. Rev. **136**, A335 (1964).

[20] J. Pearl, *Current distribution in superconducting films carrying quantized fluxoids*, Appl. Phys. Lett. **5**, 65 (1964).

[21] W. J. Kossler, N. Abraham, C. E. Stronach, and A. J. Greer, *Magnetic fields of vortices in a superconducting thin film*, Phys. Procedia **30**, 241 (2012).

[22] E. H. Brandt, *Thin superconductors in a perpendicular magnetic ac field: General formulation and strip geometry*, Phys. Rev. B **49**, 9024 (1994).

[23] E. H. Brandt, M. V. Indenbom, and A. Forkl, *Type-II superconducting strip in perpendicular magnetic field*, Europhys. Lett. **22**, 735 (1993).

[24] H. J. Jensen, *Self-organized criticality: emergent complex behavior in physical and biological systems* (Cambridge University Press, 1998).

[25] E. Altshuler and T. H. Johansen, *Colloquium: Experiments in vortex avalanches*, Rev. Mod. Phys. **76**, 471 (2004).

[26] R. G. Mints and A. L. Rakhmanov, *Critical state stability in type-II superconductors and superconducting-normal-metal composites*, Rev. Mod. Phys. **53**, 551 (1981).

[27] J. I. Vestgården, D. V. Shantsev, Y. M. Galperin, and T. H. Johansen, *Lightning in superconductors*, Sci. Rep. **2** (2012).

[28] U. Bolz, B. Biehler, D. Schmidt, B.-U. Runge, and P. Leiderer, *Dynamics of the dendritic flux instability in $YB_2Cu_3O_{7-\delta}$ films*, Europhys. Lett. **64**, 517 (2003).

[29] J. I. Vestgården, D. V. Shantsev, Y. M. Galperin, and T. H. Johansen, *Dynamics and morphology of dendritic flux avalanches in superconducting films*, Phys. Rev. B **84**, 054537 (2011).

[30] C. A. Duran, P. L. Gammel, R. E. Miller, and D. J. Bishop, *Observation of magnetic-field penetration via dendritic growth in superconducting niobium films*, Phys. Rev. B **52**, 75 (1995).

[31] D. V. Denisov *et al.*, *Onset of dendritic flux avalanches in superconducting films*, Phys. Rev. Lett. **97**, 077002 (2006).

[32] Y. Takahashi, *Two hundred years of Lichtenberg figures*, J. Electrostat. **6**, 1 (1979).

[33] I. Aranson, A. Gurevich, and V. Vinokur, *Vortex avalanches and magnetic flux fragmentation in superconductors*, Phys. Rev. Lett. **87**, 067003 (2001).

[34] D. V. Denisov, A. L. Rakhmanov, D. V. Shantsev, Y. M. Galperin, and T. H. Johansen, *Dendritic and uniform flux jumps in superconducting films*, Phys. Rev. B **73**, 014512 (2006).

[35] J. I. Vestgården, P. Mikheenko, Y. M. Galperin, and T. H. Johansen, *Inductive braking of thermomagnetic avalanches in superconducting films*, Supercond. Sci. Technol. **27**, 055014 (2014).

[36] I. L. Maksimov, *On the magnetic flux - branching instability in superconductors*, Physica C **235**, 3017 (1994).

[37] E. Baruch-El *et al.*, *Dendritic flux instabilities in $YB_2Cu_3O_{7-x}$ films: Effects of temperature and magnetic field ramp rate*, Phys. Rev. B **94**, 054509 (2016).

[38] Montana Instruments, *Montana Instruments Knowledge Base*, available online at `http://resources.montanainstruments.com/help` (2017).

[39] W. E. Gifford, *The Gifford-McMahon cycle*, Adv. Cryog. Eng. **11**, 152 (1966).

[40] M. Motta, *Flux avalanches in patterned superconducting thin films: ac susceptibility, morphology and related studies*, PhD thesis, Universidade Federal de São Carlos (2013).

[41] M. R. Koblischka and R. J. Wijngaarden, *Magneto-optical investigations of superconductors*, Supercond. Sci. Technol. **8**, 199 (1995).

[42] C. Jooss, J. Albrecht, H. Kuhn, S. Leonhardt, and H. Kronmüller, *Magneto-optical studies of current distributions in high-T_c superconductors*, Rep. Prog. Phys. **65**, 651 (2002).

[43] M. Faraday, *Experimental researches in electricity. Nineteenth series*, Philos. Trans. R. Soc. London **136**, 1 (1846).

[44] B.-U. Runge, U. Bolz, J. Eisenmenger, and P. Leiderer, *Ultrafast magneto-optical study of flux avalanches in high-T_c superconductors*, Physica C **341**, 2029 (2000).

[45] S. J. Bending, *Local magnetic probes of superconductors*, Adv. Phys. **48**, 449 (1999).

[46] P. E. Goa, H. Hauglin, Å. A. F. Olsen, M. Baziljevich, and T. H. Johansen, *Magneto-optical imaging setup for single vortex observation*, Rev. Sci. Instrum. **74**, 141 (2003).

[47] I. S. Veshchunov *et al.*, *Optical manipulation of single flux quanta*, Nat. Commun. **7** (2016).

[48] D. H. Goldstein, *Polarized light* (CRC press, 2016).

[49] R. C. Jones, *A new calculus for the treatment of optical systems: I. Description and discussion of the calculus*, J. Opt. Soc. Am. **31**, 488 (1941).

[50] H. Kirchner, *Improved Faraday technique for observing magnetic structures in superconductors*, Phys. Lett. A **30**, 437 (1969).

[51] P. B. Alers, *Structure of the intermediate state in superconducting lead*, Phys. Rev. **105**, 104 (1957).

[52] T. Schuster, M. R. Koblischka, B. Ludescher, N. Moser, and H. Kronmüller, *EuSe as magneto-optical active coating for use with the high resolution Faraday effect*, Cryogenics **31**, 811 (1991).

[53] W. DeSorbo, *Study of the intermediate state in superconductors using cerium phosphate glass*, Phys. Rev. Lett. **4**, 406 (1960).

[54] B. Dutoit and L. Rinderer, *Use of europium selenide films for magneto-optical studies at low temperatures*, Jpn. J. Appl. Phys. **26**, 1661 (1987).

[55] H.-U. Habermeier, *Paving the way for the success of magneto-optics, in "Magneto-Optical Imaging"* (Springer Netherlands, Dordrecht, 2004), pp. 1–10.

[56] M. V. Indenbom, V. I. Nikitenko, A. A. Polyanskii, and V. K. Vlasko-Vlasov, *New method for direct study of magnetic flux distribution in superconductors*, Cryogenics **30**, 747 (1990).

[57] P. Hansen, K. Witter, and W. Tolksdorf, *Magnetic and magneto-optic properties of lead-and bismuth-substituted yttrium iron garnet films*, Phys. Rev. B **27**, 6608 (1983).

[58] L. A. Dorosinskii *et al.*, *Studies of HTSC crystal magnetization features using indicator magnetooptic films with in-plane anisotropy*, Physica C **203**, 149 (1992).

[59] D. L. Wood and K. Nassau, *Optical properties of gadolinium gallium garnet*, Appl. Opt. **29**, 3704 (1990).

[60] F. Hansteen *et al.*, *Optical and magnetooptical properties of bismuth and gallium substituted iron garnet films*, Thin Solid Films **455**, 429 (2004).

[61] P. Hansen, C.-P. Klages, J. Schuldt, and K. Witter, *Magnetic and magneto-optical properties of bismuth-substituted lutetium iron garnet films*, Phys. Rev. B **31**, 5858 (1985).

[62] F. Laviano *et al.*, *An improved method for quantitative magneto-optical analysis of superconductors*, Supercond. Sci. Technol. **16**, 71 (2002).

[63] A. Hubert and R. Schäfer, *Magnetic domains: the analysis of magnetic microstructures* (Springer Science & Business Media, 2008).

[64] L. E. Helseth, R. W. Hansen, E. I. Il'yashenko, M. Baziljevich, and T. H. Johansen, *Faraday rotation spectra of bismuth-substituted ferrite garnet films with in-plane magnetization*, Phys. Rev. B **64**, 174406 (2001).

[65] M. Tokunaga, T. Tamegai, and T. H. Johansen, *Improvement of vortex imaging in magneto-optical technique and bitter decoration*, Physica C **437**, 331 (2006).

[66] National Institute of Health, *ImageJ software*, available online at `http://imagej.nih.gov/ij` (2017).

[67] R. J. Wijngaarden *et al.*, *Fast imaging polarimeter for magneto-optical investigations*, Rev. Sci. Instrum. **72**, 2661 (2001).

[68] P. Mandal, D. Chowdhury, S. S. Banerjee, and T. Tamegai, *High sensitivity differential magneto-optical imaging with a compact Faraday-modulator*, Rev. Sci. Instrum. **83**, 123906 (2012).

[69] A. Soibel *et al.*, *Imaging the vortex-lattice melting process in the presence of disorder*, Nature **406**, 282 (2000).

[70] M. Terao, Y. Tokunaga, M. Tokunaga, and T. Tamegai, *Observation of single vortices by magneto-optical imaging*, Physica C **426**, 94 (2005).

[71] H. U. Habermeier, W. Klein, R. Aoki, and H. Kronmüller, *Magneto-optical investigation of flux penetration in plastically deformed niobium monocrystals*, Phys. Status Solidi A **53**, 225 (1979).

[72] T. H. Johansen *et al.*, *Direct observation of the current distribution in thin superconducting strips using magneto-optic imaging*, Phys. Rev. B **54**, 16264 (1996).

[73] M. Roussel, *Magneto-optical imaging in superconductors*, PhD thesis, University of Wollongong (2007).

[74] P. Thévenaz, *StackReg, an ImageJ plugin for the recursive alignment of a stack of images*, available online at `http://bigwww.epfl.ch/thevenaz/stackreg` (2017).

[75] J. I. Vestgården *et al.*, *Interaction between superconducting vortices and a Bloch wall in ferrite garnet films*, Phys. Rev. Lett. **98**, 117002 (2007).

[76] J. Brisbois *et al.*, *Magnetic flux penetration in Nb superconducting films with lithographically defined microindentations*, Phys. Rev. B **93**, 054521 (2016).

[77] R. Engel-Herbert and T. Hesjedal, *Calculation of the magnetic stray field of a uniaxial magnetic domain*, J. Appl. Phys. **97**, 074504 (2005).

[78] E. Seynaeve *et al.*, *Transition from a single-domain to a multidomain state in mesoscopic ferromagnetic Co structures*, J. Appl. Phys. **89**, 531 (2001).

[79] B. D. Cullity and C. D. Graham, *Introduction to magnetic materials* (John Wiley & Sons, 2011).

[80] V. L. Pokrovsky, K. Romanov, and H. Wei, *Magnetic configurations of hybrid ferromagnetic dot-superconductor systems*, J. Magn. Magn. Mater. **307**, 107 (2006).

[81] A. A. Fraerman, I. R. Karetnikova, I. M. Nefedov, I. A. Shereshevskii, and M. A. Silaev, *Magnetization reversal of a nanoscale ferromagnetic disk placed above a superconductor*, Phys. Rev. B **71**, 094416 (2005).

[82] J. Brisbois *et al.*, *Imprinting superconducting vortex footsteps in a magnetic layer*, Sci. Rep. **6** (2016).

[83] P. W. Anderson, *Theory of flux creep in hard superconductors*, Phys. Rev. Lett. **9**, 309 (1962).

[84] P. W. Anderson and Y. B. Kim, *Hard superconductivity: theory of the motion of Abrikosov flux lines*, Rev. Mod. Phys. **36**, 39 (1964).

[85] Y. B. Kim, M. J. Stephen, and R. D. Parks, *Superconductivity, vol. 2* (Marcel Dekker, New York, 1969).

[86] R. B. Harrison, J. P. Pendrys, and L. S. Wright, *Damping effects and flux kinetics in a type II superconducting disk*, J. Low Temp. Phys. **18**, 113 (1975).

[87] M. Baziljevich *et al.*, *Origin of dendritic flux patterns in MgB_2 films*, Physica C **369**, 93 (2002).

[88] E.-M. Choi *et al.*, *Dendritic magnetic avalanches in carbon-free MgB_2 thin films with and without a deposited Au layer*, Appl. Phys. Lett. **87**, 152501 (2005).

[89] E.-M. Choi *et al.*, *Suppression of dendritic flux jumps in MgB_2 films coated with a gold rim*, Supercond. Sci. Technol. **22**, 015011 (2008).

[90] J. Albrecht *et al.*, *Bending of magnetic avalanches in MgB_2 thin films*, Appl. Phys. Lett. **87**, 182501 (2005).

[91] F. Colauto *et al.*, *Suppression of flux avalanches in superconducting films by electromagnetic braking*, Appl. Phys. Lett. **96**, 092512 (2010).

[92] M. Danckwerts, A. R. Goni, C. Thomsen, K. Eberl, and A. G. Rojo, *Enhanced vortex damping by eddy currents in superconductor-semiconductor hybrids*, Phys. Rev. Lett. **84**, 3702 (2000).

[93] J. Baker and A. G. Rojo, *Vortex viscosity due to eddy currents in superconductor-semiconductor hybrids*, Phys. Rev. B **64**, 014513 (2001).

[94] J. I. Vestgården, Y. M. Galperin, and T. H. Johansen, *The thermomagnetic instability in superconducting films with adjacent metal layer*, J. Low Temp. Phys. **173**, 303 (2013).

[95] M. R. Wertheimer and J. l. G. Gilchrist, *Flux jumps in type II superconductors*, J. Phys. Chem. Solids **28**, 2509IN12515 (1967).

[96] G. Carneiro and E. H. Brandt, *Vortex lines in films: Fields and interactions*, Phys. Rev. B **61**, 6370 (2000).

[97] A. I. Larkin and Y. U. N. Ovchinnikov, *Nonlinear conductivity of superconductors in the mixed state*, Sov. Phys. JETP **41**, 960 (1975).

[98] M. N. Kunchur, *Unstable flux flow due to heated electrons in superconducting films*, Phys. Rev. Lett. **89**, 137005 (2002).

[99] A. Gurevich and G. Ciovati, *Dynamics of vortex penetration, jumpwise instabilities, and nonlinear surface resistance of type-II superconductors in strong rf fields*, Phys. Rev. B **77**, 104501 (2008).

[100] M. Menghini, R. J. Wijngaarden, A. V. Silhanek, S. Raedts, and V. V. Moshchalkov, *Dendritic flux penetration in Pb films with a periodic array of antidots*, Phys. Rev. B **71**, 104506 (2005).

[101] M. Motta *et al.*, *Controllable morphology of flux avalanches in microstructured superconductors*, Phys. Rev. B **89**, 134508 (2014).

[102] J. Albrecht, P. Audehm, and M. Djupmyr, *Chaotic vortex dynamics and low current phases in the remanent state of MgB_2 thin films*, Supercond. Sci. Technol. **21**, 045016 (2008).

[103] J. C. Maxwell, *On the induction of electric currents in an infinite plane sheet of uniform conductivity*, Proc. R. Soc. Lond. **XX**, 160 (1872).

[104] J. R. Reitz, *Forces on moving magnets due to eddy currents*, J. Appl. Phys. **41**, 2067 (1970).

[105] W. M. Saslow, *Maxwell's theory of eddy currents in thin conducting sheets, and applications to electromagnetic shielding and MAGLEV*, Am. J. Phys. **60**, 693 (1992).

[106] W. M. Saslow, *How a superconductor supports a magnet, how magnetically "soft" iron attracts a magnet, and eddy currents for the uninitiated*, Am. J. Phys. **59**, 16 (1991).

[107] T. D. Rossing and J. R. Hull, *Magnetic levitation*, Phys. Teach. **29**, 552 (1991).

[108] Y. Liu and J. W. Belcher, *Magnetic flux diffusion and expulsion with thin conducting sheets*, arXiv:0712.0182 (2007).

[109] S. W. Lee and R. Menendez, *Forces at low- and high- speed limits in magnetic levitation systems*, J. Appl. Phys. **46**, 422 (1975).

[110] E. V. Votyakov and A. Thess, *Interaction of a magnetic dipole with a slowly moving electrically conducting plate*, J. Eng. Math. **77**, 147 (2012).

[111] H. A. Barnes, *Thixotropy - a review*, J. Non-Newton. Fluid. **70**, 1 (1997).

[112] G. Grimaldi, A. Leo, A. Nigro, S. Pace, and R. P. Huebener, *Dynamic ordering and instability of the vortex lattice in Nb films exhibiting moderately strong pinning*, Phys. Rev. B **80**, 144521 (2009).

[113] O.-A. Adami *et al.*, *Onset, evolution, and magnetic braking of vortex lattice instabilities in nanostructured superconducting films*, Phys. Rev. B **92**, 134506 (2015).

[114] D. Y. Vodolazov and F. M. Peeters, *Rearrangement of the vortex lattice due to instabilities of vortex flow*, Phys. Rev. B **76**, 014521 (2007).

[115] A. V. Silhanek *et al.*, *Formation of stripelike flux patterns obtained by freezing kinematic vortices in a superconducting Pb film*, Phys. Rev. Lett. **104**, 017001 (2010).

[116] J. Van de Vondel *et al.*, *Vortex core deformation and stepper-motor ratchet behavior in a superconducting aluminum film containing an array of holes*, Phys. Rev. Lett. **106**, 137003 (2011).

[117] L. C. Davis and J. R. Reitz, *Eddy currents in finite conducting sheets*, J. Appl. Phys. **42**, 4119 (1971).

[118] R. H. Borcherts and L. C. Davis, *Force on a coil moving over a conducting surface including edge and channel effects*, J. Appl. Phys. **43**, 2418 (1972).

[119] J. R. Reitz and L. C. Davis, *Force on a rectangular coil moving above a conducting slab*, J. Appl. Phys. **43**, 1547 (1972).

[120] P. Mikheenko, T. H. Johansen, S. Chaudhuri, I. J. Maasilta, and Y. M. Galperin, *Ray optics behavior of flux avalanche propagation in superconducting films*, Phys. Rev. B **91**, 060507 (2015).

[121] J. Brisbois *et al.*, *Classical analogy for the deflection of flux avalanches by a metallic layer*, New J. Phys. **16**, 103003 (2014).

[122] P. Mikheenko *et al.*, *Metal frame as local protection of superconducting films from thermomagnetic avalanches*, AIP Advances **6**, 035304 (2016).

[123] A. Andronov, I. Gordion, V. Kurin, I. Nefedov, and I. Shereshevsky, *Kinematic vortices and phase slip lines in the dynamics of the resistive state of narrow superconductive thin film channels*, Physica C **213**, 193 (1993).

[124] A. G. Sivakov *et al.*, *Josephson behavior of phase-slip lines in wide superconducting strips*, Phys. Rev. Lett. **91**, 267001 (2003).

[125] I. Giaever, *Magnetic coupling between two adjacent type-II superconductors*, Phys. Rev. Lett. **15**, 825 (1965).

[126] P. E. Goa, H. Hauglin, Å. A. F. Olsen, D. Shantsev, and T. H. Johansen, *Manipulation of vortices by magnetic domain walls*, Appl. Phys. Lett. **82**, 79 (2003).

[127] T. Schuster *et al.*, *Flux penetration into $YBa_2Cu_3O_x$ thin films covering substrate step edges*, Appl. Phys. Lett. **62**, 768 (1993).

[128] B. L. T. Plourde *et al.*, *Vortex distributions near surface steps observed by scanning SQUID microscopy*, Phys. Rev. B **66**, 054529 (2002).

[129] F. Pardo *et al.*, *Real space images of the vortex lattice structure in a type II superconductor during creep over a barrier*, Phys. Rev. Lett. **79**, 1369 (1997).

[130] J. Barba-Ortega, J. D. Gonzalez, and E. Sardella, *Superconducting state of a disk with a pentagonal/hexagonal trench/barrier*, J. Low Temp. Phys. **174**, 96 (2014).

[131] R. A. Matula, *Electrical resistivity of copper, gold, palladium, and silver*, J. Phys. Chem. Ref. Data **8**, 1147 (1979).

[132] J. I. Vestgården, D. V. Shantsev, Y. M. Galperin, and T. H. Johansen, *The diversity of flux avalanche patterns in superconducting films*, Supercond. Sci. Technol. **26**, 055012 (2013).

[133] J. R. Clem and K. K. Berggren, *Geometry-dependent critical currents in superconducting nanocircuits*, Phys. Rev. B **84**, 174510 (2011).

[134] O.-A. Adami *et al.*, *Current crowding effects in superconducting corner-shaped Al microstrips*, Appl. Phys. Lett. **102**, 052603 (2013).

[135] D. Cerbu *et al.*, *Vortex ratchet induced by controlled edge roughness*, New J. Phys. **15**, 063022 (2013).

[136] G. Via, C. Navau, and A. Sanchez, *Magnetic and transport currents in thin film superconductors of arbitrary shape within the london approximation*, J. Appl. Phys. **113**, 093905 (2013).

[137] J. I. Vestgården, D. V. Shantsev, Y. M. Galperin, and T. H. Johansen, *Flux penetration in a superconducting strip with an edge indentation*, Phys. Rev. B **76**, 174509 (2007).

[138] A. Gurevich and M. Friesen, *Nonlinear transport current flow in superconductors with planar obstacles*, Phys. Rev. B **62**, 4004 (2000).

[139] M. Tinkham, *Introduction to Superconductivity* (Dover Publications, 2004).

[140] A. I. Gubin, K. S. Il'in, S. A. Vitusevich, M. Siegel, and N. Klein, *Dependence of magnetic penetration depth on the thickness of superconducting Nb thin films*, Phys. Rev. B **72**, 064503 (2005).

[141] A. M. Chang *et al.*, *Scanning Hall probe microscopy*, Appl. Phys. Lett. **61**, 1974 (1992).

[142] F. Hengstberger, M. Eisterer, and H. W. Weber, *Thickness dependence of the critical current density in superconducting films: A geometrical approach*, Appl. Phys. Lett. **96**, 022508 (2010).

[143] E. Baruch-El, M. Baziljevich, T. H. Johansen, and Y. Yeshurun, *Substrate influence on dendritic flux instability in YBCO thin films*, J. Supercond. Nov. Magn. **28**, 379 (2015).

[144] J. I. Vestgarden, Y. M. Galperin, and T. H. Johansen, *Dendritic flux avalanches in superconducting films of different thickness*, arXiv:1309.6463 (2013).

[145] F. Colauto, E. J. Patiño, M. Aprilli, and W. A. Ortiz, *The role of demagnetizing factors in the occurrence of vortex avalanches in Nb thin films*, J. Phys. Conf. Ser. **150**, 052038 (2009).

[146] G. R. Berdiyorov *et al.*, *Pillars as antipinning centers in superconducting films*, Phys. Rev. B **77**, 024526 (2008).

[147] G. R. Berdiyorov, M. V. Milošević, B. J. Baelus, and F. M. Peeters, *Superconducting vortex state in a mesoscopic disk containing a blind hole*, Phys. Rev. B **70**, 024508 (2004).

[148] M. V. Milošević, G. R. Berdiyorov, and F. M. Peeters, *Fluxonic cellular automata*, Appl. Phys. Lett. **91**, 212501 (2007).

[149] J. Barba-Ortega, E. Sardella, and J. A. Aguiar, *Superconducting properties of a parallelepiped mesoscopic superconductor: A comparative study between the 2D and 3D Ginzburg-Landau models*, Phys. Lett. A **379**, 732 (2015).

[150] S. J. Chapman, Q. Du, and M. D. Gunzburger, *A model for variable thickness superconducting thin films*, Zeitschrift für angewandte Mathematik und Physik ZAMP **47**, 410 (1996).

[151] V. N. Gladilin *et al.*, *Vortices in a wedge made of a type-I superconductor*, New J. Phys. **17**, 063032 (2015).

[152] R. Kato, Y. Enomoto, and S. Maekawa, *Computer simulations of dynamics of flux lines in type-II superconductors*, Phys. Rev. B **44**, 6916 (1991).

[153] A. V. Silhanek *et al.*, *Local probing of the vortex–antivortex dynamics in superconductor/ferromagnet hybrid structures*, Supercond. Sci. Technol. **24**, 024007 (2011).

[154] V. N. Gladilin, J. Tempere, J. T. Devreese, and V. V. Moshchalkov, *Negative-μ regime in the ac magnetic response of superconductor nanoshells*, Solid State Commun. **152**, 1781 (2012).

[155] V. N. Gladilin, J. Tempere, J. T. Devreese, W. Gillijns, and V. V. Moshchalkov, *Vortex-antivortex pair generation by an in-plane magnetic dipole on a superconducting film*, Phys. Rev. B **80**, 054503 (2009).

[156] D. C. Larbalestier *et al.*, *Isotropic round-wire multifilament cuprate superconductor for generation of magnetic fields above 30 T*, Nat. Mater. **13**, 375 (2014).

[157] M. Berciu, T. G. Rappoport, and B. Jankó, *Manipulating spin and charge in magnetic semiconductors using superconducting vortices*, Nature **435**, 71 (2005).

[158] A. Y. Aladyshkin, A. V. Silhanek, W. Gillijns, and V. V. Moshchalkov, *Nucleation of superconductivity and vortex matter in superconductor–ferromagnet hybrids*, Supercond. Sci. Technol. **22**, 053001 (2009).

[159] A. I. Buzdin, *Proximity effects in superconductor-ferromagnet heterostructures*, Rev. Mod. Phys. **77**, 935 (2005).

[160] I. F. Lyuksyutov and V. L. Pokrovsky, *Ferromagnet–superconductor hybrids*, Adv. Phys. **54**, 67 (2005).

[161] M. Vélez *et al.*, *Superconducting vortex pinning with artificial magnetic nanostructures*, J. Magn. Magn. Mater. **320**, 2547 (2008).

[162] C. C. de Souza Silva *et al.*, *Dipole-induced vortex ratchets in superconducting films with arrays of micromagnets*, Phys. Rev. Lett. **98**, 117005 (2007).

[163] A. V. Silhanek *et al.*, *Manipulation of the vortex motion in nanostructured ferromagnetic/superconductor hybrids*, Appl. Phys. Lett. **90**, 182501 (2007).

[164] R. B. G. Kramer, A. V. Silhanek, W. Gillijns, and V. V. Moshchalkov, *Imaging the statics and dynamics of superconducting vortices and antivortices induced by magnetic microdisks*, Phys. Rev. X **1**, 021004 (2011).

[165] T. Tamegai, Y. Nakao, S. Mohan, and Y. Nakajima, *Experimental demonstration of shrinkage of magnetic domains in a superconductor/ferromagnet bilayer*, Supercond. Sci. Technol. **24**, 024015 (2011).

[166] V. Vlasko-Vlasov *et al.*, *Coupled domain structures in superconductor/ferromagnet Nb-Fe/garnet bilayers*, Phys. Rev. B **82**, 100502 (2010).

[167] V. Vlasko-Vlasov *et al.*, *Domain structure and magnetic pinning in ferromagnetic/superconducting hybrids*, Phys. Rev. B **85**, 064505 (2012).

[168] S. Erdin, I. F. Lyuksyutov, V. L. Pokrovsky, and V. M. Vinokur, *Topological textures in a ferromagnet-superconductor bilayer*, Phys. Rev. Lett. **88**, 017001 (2001).

[169] M. Iavarone *et al.*, *Imaging the spontaneous formation of vortex-antivortex pairs in planar superconductor/ferromagnet hybrid structures*, Phys. Rev. B **84**, 024506 (2011).

[170] A. Palau *et al.*, *Hysteretic vortex pinning in superconductor-ferromagnet nanocomposites*, Phys. Rev. Lett. **98**, 117003 (2007).

[171] V. Vlasko-Vlasov *et al.*, *Guiding superconducting vortices with magnetic domain walls*, Phys. Rev. B **77**, 134518 (2008).

[172] C. Stahl *et al.*, *Using magnetic coupling in bilayers of superconducting YBCO and soft-magnetic CoFeB to map supercurrent flow*, Europhys. Lett. **106**, 27002 (2014).

[173] N. Saito, H. Fujiwara, and Y. Sugita, *A new type of magnetic domain structure in negative magnetostriction Ni-Fe films*, J. Phys. Soc. Jpn **19**, 1116 (1964).

[174] Y. Murayama, *Micromagnetics on stripe domain films. I. Critical cases*, J. Phys. Soc. Jpn **21**, 2253 (1966).

[175] Y. Murayama, *Micromagnetics on stripe domain films. ii*, J. Phys. Soc. Jpn **23**, 510 (1967).

[176] Y. Sugita, H. Fujiwara, and T. Sato, *Critical thickness and perpendicular anisotropy of evaporated permalloy films with stripe domains*, Appl. Phys. Lett. **10**, 229 (1967).

[177] R. Szymczak, *A modification of the Kittel open structure*, J. Appl. Phys. **39**, 875 (1968).

[178] A. Holz and H. Kronmüller, *The nucleation of stripe domains in thin ferromagnetic films*, Phys. Status Solidi B **31**, 787 (1969).

[179] T. Dastagir *et al.*, *Tuning the permeability of permalloy films for on-chip inductor applications*, Appl. Phys. Lett. **97**, 162506 (2010).

[180] N. Amos *et al.*, *Magnetic force microscopy study of magnetic stripe domains in sputter deposited permalloy thin films*, J. Appl. Phys. **103**, 07E732 (2008).

[181] D. Mancusi *et al.*, *Magnetic pinning in a superconducting film by a ferromagnetic layer with stripe domains*, Supercond. Sci. Technol. **27**, 125002 (2014).

[182] J. B. Youssef, N. Vukadinovic, D. Billet, and M. Labrune, *Thickness-dependent magnetic excitations in permalloy films with nonuniform magnetization*, Phys. Rev. B **69**, 174402 (2004).

[183] L. S. Uspenskaya, O. A. Tikhomirov, S. I. Bozhko, S. V. Egorov, and A. A. Chugunov, *Domain structure and magnetization of the permalloy/niobium bilayers*, J. Appl. Phys. **113**, 163907 (2013).

[184] M. V. Milošević and F. M. Peeters, *Vortex pinning in a superconducting film due to in-plane magnetized ferromagnets of different shapes: The London approximation*, Phys. Rev. B **69**, 104522 (2004).

[185] D. Y. Vodolazov *et al.*, *Considerable enhancement of the critical current in a superconducting film by a magnetized magnetic strip*, Phys. Rev. B **72**, 064509 (2005).

[186] A. Belkin *et al.*, *Tunable transport in magnetically coupled MoGe/permalloy hybrids*, Appl. Phys. Lett. **93**, 072510 (2008).

[187] A. Belkin, V. Novosad, M. Iavarone, J. Pearson, and G. Karapetrov, *Superconductor/ferromagnet bilayers: Influence of magnetic domain structure on vortex dynamics*, Phys. Rev. B **77**, 180506 (2008).

[188] R. F. Lopes *et al.*, *Spin texture on top of flux avalanches in $Nb/Al_2O_3/Co$ thin film heterostructures*, J. Appl. Phys. **121**, 013905 (2017).

[189] F. Dumas-Bouchiat *et al.*, *Thermomagnetically patterned micromagnets*, Appl. Phys. Lett. **96**, 102511 (2010).

[190] G. Shaw, R. B. G. Kramer, N. M. Dempsey, and K. Hasselbach, *A scanning Hall probe microscope for high resolution, large area, variable height magnetic field imaging*, Rev. Sci. Instrum. **87**, 113702 (2016).

[191] M. S. Welling, R. J. Westerwaal, W. Lohstroh, and R. J. Wijngaarden, *Huge compact flux avalanches in superconducting Nb thin films*, Physica C **411**, 11 (2004).

[192] A. A. Bespalov, A. S. Mel'Nikov, and A. I. Buzdin, *Magnon radiation by moving Abrikosov vortices in ferromagnetic superconductors and superconductor-ferromagnet multilayers*, Phys. Rev. B **89**, 054516 (2014).

[193] Y. Nakatani, A. Thiaville, and J. Miltat, *Faster magnetic walls in rough wires*, Nat. Mater. **2**, 521 (2003).

[194] T. Schuster, M. V. Indenbom, M. R. Koblischka, H. Kuhn, and H. Kronmüller, *Observation of current-discontinuity lines in type-II superconductors*, Phys. Rev. B **49**, 3443 (1994).

[195] T. Schuster, H. Kuhn, and E. H. Brandt, *Flux penetration into flat superconductors of arbitrary shape: Patterns of magnetic and electric fields and current*, Phys. Rev. B **54**, 3514 (1996).

List of publications

1. **Determination of the magnetic penetration depth in a superconducting Pb film**
   J. Brisbois, B. Raes, J. Van de Vondel, V. V. Moshchalkov, and A. V. Silhanek.
   Journal of Applied Physics **115**, 103906 (2014).

2. **Classical analogy for the deflection of flux avalanches by a metallic layer**
   J. Brisbois, B. Vanderheyden, F. Colauto, M. Motta, W. A. Ortiz, J. Fritzsche, N. D. Nguyen, B. Hackens, O.-A. Adami, and A. V. Silhanek
   New Journal of Physics **16**, 103003 (2014).

3. **Magnetic flux penetration in Nb superconducting films with lithographically defined micro-indentations**
   J. Brisbois, O.-A. Adami, J. I. Avila, M. Motta, W. A. Ortiz, N. D. Nguyen, P. Vanderbemden, B. Vanderheyden, R. B. G. Kramer, and A. V. Silhanek.
   Physical Review B **93**, 54521 (2016).

4. **Impurity scattering effects on the superconducting properties and the tetragonal-to-orthorhombic phase transition in FeSe**
   M. Abdel-Hafiez, Y. J. Pu, **J. Brisbois**, R. Peng, D. L. Feng, D. A. Chareev, A. V. Silhanek, C. Krellner, and A. N. Vasiliev.
   Physical Review B **93**, 224508 (2016).

5. **Imprinting superconducting vortex footsteps in a magnetic layer**
   J. Brisbois, M. Motta, J. I. Avila, G. Shaw, T. Devillers, N. M. Dempsey, S. K. P. Veerapandian, P. Colson, B. Vanderheyden, P. Vanderbemden, W. A. Ortiz, N. D. Nguyen, R. B. G. Kramer, and A. V. Silhanek
   Scientific Reports **6**, 27159 (2016).

6. **Probing the low-frequency vortex dynamics in a nanostructured superconducting strip**
   C. C. de Souza Silva, B. Raes, **J. Brisbois**, L. R. E. Cabral, A. V. Silhanek, J.

Van de Vondel, and V. V. Moshchalkov.
Physical Review B **94**, 24516 (2016).

7. **Flux penetration in a superconducting film partially capped with a conducting layer**
J. Brisbois, V. N. Gladilin, J. Tempere, J. T. Devreese, V. V. Moshchalkov, F. Colauto, M. Motta, T. H. Johansen, J. Fritzsche, O.-A. Adami, N. D. Nguyen, W. A. Ortiz, R. B. G. Kramer, and A. V. Silhanek.
Physical Review B **95**, 94506 (2017).

8. **Statistics of localized phase slips in tunable width planar point contacts**
X. D. A. Baumans, V. S. Zharinov, E. Raymenants, S. Blanco Alvarez, J. E. Scheerder, **J. Brisbois**, D Massarotti, R. Caruso, F. Tafuri, E. Janssens, V. V. Moshchalkov, J. Van de Vondel, and A. V. Silhanek.
Scientific Reports **7**, 44569 (2017).

9. **Healing effect of controlled anti-electromigration on conventional and high-T_c superconducting nanowires**
X. D. A. Baumans, J. Lombardo, **J. Brisbois**, G. Shaw, V. S. Zharinov, G. He, H. Yu, J. Yuan, B. Zhu, K. Jin, R. B. G. Kramer, J. Van de Vondel, and A. V. Silhanek.
Small, 1700384 (2017).

10. **Quantitative magneto-optical investigation of superconductor-ferromagnet hybrid structures**
G. Shaw*, **J. Brisbois***, L. B. G. L. Pinheiro, J. Müller, S. Blanco Alvarez, T. Devillers, N. M. Dempsey, J. E. Scheerder, J. Van de Vondel, S. Melinte, P. Vanderbemden, M. Motta, W. A. Ortiz, K. Hasselbach, R. B. G. Kramer, and A. V. Silhanek.
* These authors contributed equally to this work.
In preparation (2017).

11. **Distinction between critical current effects and intrinsic anomalies in the point-contact Andreev reflection spectrum of unconventional superconductors**
G. He*, Z. Wei*, **J. Brisbois***, Y. Jia, Y. Huang, A. V. Silhanek, J. Yuan, X. Dong, B. Zhu, and K. Jin.
* These authors contributed equally to this work.
In preparation (2017).

Electronic version at the institutional repository (ORBi):

Experimental Physics of Nanostructured Materials website: